

Title	直接インプリント法によるIn ₂ O ₃ 系酸化物薄膜の形成と薄膜トランジスタへの応用に関する研究
Author(s)	Jain, Puneet
Citation	
Issue Date	2019-09
Type	Thesis or Dissertation
Text version	ETD
URL	http://hdl.handle.net/10119/16192
Rights	
Description	Supervisor:徳光 永輔, 先端科学技術研究科, 博士

**Investigation of In₂O₃-based Oxide Films by
Direct Imprinting for
TFT Application**

Puneet Jain

Japan Advanced Institute of Science and Technology

Doctoral Dissertation

**Investigation of In₂O₃-based Oxide Films by
Direct Imprinting for
TFT Application**

Puneet Jain

Supervisor: Professor Eisuke Tokumitsu

**Graduate School of Advanced Science and Technology
Japan Advanced Institute of Science and Technology
Materials Science
September 2019**

Abstract

In this work, bottom gate thin film transistor (TFT) using a novel imprinting technique, nano-rheology printing (n-RP), has been fabricated using solution process derived indium oxide (In_2O_3) as a channel and source/drain; while solution process derived hafnium oxide (HfO_2) as a gate insulator. Platinum (Pt) has been used as gate electrode.

To fabricate TFT, at first the electrical properties of indium oxide (In_2O_3) and indium tin oxide (ITO) were studied, which were fabricated by solution process. The source solution of In_2O_3 and ITO were synthesized by indium acetylacetonate ($\text{In}(\text{acac})_3$) precursor. It has also been found that using $\text{In}(\text{acac})_3$ precursor, high mobility of around $42.7 \text{ cm}^2/\text{Vs}$ can be obtained for In_2O_3 films. The obtained resistivity for 1 wt.% ITO was $2.6 \times 10^{-3} \Omega\text{cm}$. $\text{In}(\text{acac})_3$ precursor has selected as this precursor has rheological properties, so, the gel films of In_2O_3 and ITO can be directly imprinted.

The channel and source/drain of the TFT were fabricated by n-RP process. The electrical and patterning properties of direct imprinted (or, nano-rheological printed, n-RP) indium oxide (In_2O_3) and indium tin oxide (ITO) were also studied in this work. It has been found that the patterns of In_2O_3 were better than those of ITO. This is because higher $\tan \delta$ (which indicates softness of the gel measured by rheometer) of In_2O_3 as compared to ITO. The patterning properties were checked by using a checker quartz mold, SNP-02. The electrical properties of imprinted In_2O_3 and ITO films were also studied and compared with that of non-imprinted films. It has found that the Hall mobility of In_2O_3 is reduced after imprinting, whereas it remains almost the same for ITO, as compared to their non-imprinted ones. It was found by SIMS measurements that the residual carbon of imprinted In_2O_3 is much higher than that of non-imprinted region, whereas only slight difference was observed in carbon concentration in ITO

films. Carrier concentration of imprinted films was increased in In_2O_3 after imprinting but did not change much in ITO as compared to their non-imprinted films.

In the fabricated TFT, 45-nm-thick HfO_2 film fabricated by the solution process was used as a high- k gate dielectric insulator. HfO_2 is monoclinic in phase and is paraelectric in nature. The leakage current density, breakdown field strength, and relative dielectric constant of HfO_2 , annealed at 700 °C for 15 min in O_2 were $1.0 \times 10^{-6} \text{ A/cm}^2$, 5.8 MV/cm, and 17, respectively.

The n-RP fabricated TFT using In_2O_3 as source/drain and channel and HfO_2 as gate dielectric, confirmed the n-channel transistor operation with an on/off ratio in the order of $\sim 10^5$ and a field effect mobility of $0.13 \text{ cm}^2/\text{Vs}$.

Keywords: solution process, nano-rheological printing, In_2O_3 , ITO, high- k , thin film transistors (TFTs)

Acknowledgement

At first, I would like to thank Professor Eisuke Tokumitsu very much, for accepting me in his lab even after spending one year in Professor Susumu Horita laboratory. I am also thankful to Professor Eisuke Tokumitsu for providing me such a novel and interesting research topic, i.e. n-RP, and his abiding guidance and encouragement during my doctor course.

I am also grateful to Professor Susumu Horita for accepting me in his laboratory and giving me the basic knowledge necessary for research.

I am also grateful to Professor Niroyashi Matsumi for his fruitful discussions with a kind direction to conduct my minor thesis in his laboratory.

My special thanks to internal committee members, Professor Mikio Koyano, Professor Hiroshi Mizuta, and Professor Keisuke Ohdaira from School of Materials Science-JAIST. I sincerely thank to Professor Mutsumi Kimura from Ryukoku University, the external committee member. I thank all of them for their time and consideration in serving on my thesis.

I am very much thankful to Assistant Professor Ken-ichi Haga for his support in scientific discussions.

Also, I should not forget to thank Assistant Professor Tue for fruitful consideration and suggestions about n-RP process.

The author would also like to thank Professor Yamaguchi for providing his support in rheological studies.

The author would like to express appreciation to Mr. Akio Miyazato for mass spectra measurements. The author would like to thank Assistant Professor Heisuke Sakai from Professor Murata laboratory for supporting in optical measurements of In_2O_3 and ITO films.

Finally, I would like to express my gratitude to my family and friends for their continuous love and support. Especially, I wish to express undying love to my mother, who supported me during the difficulties in the Ph.D journey. Finally, the author express his humble gratitude to the almighty for all the good things.

Puneet Jain

Graduate School of Advanced Science and Technology

Japan Advanced Institute of Science and Technology

September 2019

List of Figures

Fig. 1-1: Periodic table with associated elements as cations in transparent conductive oxides compounds, marked with red box [9].....	2
Fig. 1-2: Thin film deposition techniques.....	4
Fig. 1-3: Schematic of typical solution processing routes [18].....	5
Fig. 1-4: Illustration of commonly used coating techniques [19].....	5
Fig. 1-5: Spin-coating schematic.....	6
Fig. 1-6: Patterning properties of ITO, IGZO, and SnO, studied by Shimoda et al. [26].....	8
Fig. 1-7: Patterning properties of Ru-La-O, studied by Shimoda et al. by n-RP [27].....	9
Fig. 1-8: Transfer characteristics of TFT fabricatd using (a) ITO and (b) In ₂ O ₃ , as channel with BLT as ferroelectric gate insulator, by Haga et al. [28].....	9
Fig. 1-9: Comparison of TFT fabrication by photolithography and n-RP.....	10
Fig. 2-1: Schematic of crystalline In ₂ O ₃ bixbyite.....	17
Fig. 2-2: Process flow for formation of In ₂ O ₃ film on SiO ₂ substrate.....	20
Fig. 2-3: Process flow for formation of ITO films by SnCl ₂ and by Sn(acac) ₂ precursors film on SiO ₂ substrate.....	20
Fig. 2-4: TG-DTA analysis of In ₂ O ₃ and ITO.....	21
Fig. 2-5: Hall mobility and carrier concentration of In ₂ O ₃ films with respect to annealing temperature.....	23
Fig. 2-6: XRD of In ₂ O ₃ films with annealing temperature variation.....	24
Fig. 2-7: Hall mobility and carrier concentration of In ₂ O ₃ films.....	25

Fig. 2-8: SEM images of In ₂ O ₃ films annealed for 15, 60, and 90 min.....	26
Fig. 2-9: XRD of In ₂ O ₃ films by varying annealing time.....	26
Fig. 2-10: Surface roughness of In ₂ O ₃ films by varying annealing time.....	27
Fig. 2-11: AFM images of In ₂ O ₃ films annealed for 15, 60, and 90 min in O ₂ at 600 °C.....	27
Fig. 2-12: Thickness of In ₂ O ₃ films by varying annealing time.....	28
Fig. 2-13: Hall mobility, carrier concentration, and resistivity of ITO films.....	29
Fig. 2-14: XRD of ITO films for varying Sn wt.%.....	32
Fig. 2-15: Surface roughness dependence on Sn wt.% of ITO films.....	33
Fig. 2-16: Thickness dependence on Sn wt.% for ITO films.....	33
Fig. 2-17: Electrical properties of In ₂ O ₃ and ITO films by varying annealing temperature.....	34
Fig. 2-18: XRD of In ₂ O ₃ and ITO films by varying annealing temperature.....	36
Fig. 2-19: Thickness of In ₂ O ₃ and ITO films by varying annealing temperature.....	36
Fig. 2-20: Work function measurements of In ₂ O ₃ and ITO films.....	38
Fig. 3-1: Schematic of n-RP process.....	44
Fig. 3-2: SAM layer formation mechanism on mold.....	46
Fig. 3-3: Schematic of SNP-02 mold.....	47
Fig. 3-4: n-RP machine with various parts explained.....	48
Fig. 3-5: n-RP machine during imprinting.....	48
Fig. 3-6: Actual temperature v/s indicated temperature.....	49

Fig. 3-7: Imprinting of In ₂ O ₃ gel film using SNP-02 quartz mold by varying imprinting temperature.....	51
Fig. 3-8: Thickness of imprinted In ₂ O ₃ film using SNP-02 mold by varying imprinting pressure.....	52
Fig. 3-9: Optical microscope images of n-RPed (a) In ₂ O ₃ , (b) ITO via Sn(acac) ₂ , and (c) ITO via SnCl ₂	52
Fig. 3-10: Thickness of In ₂ O ₃ , ITO via Sn(acac) ₂ , and ITO via SnCl ₂ before and after annealing, with imprinting temperature, pressure, time, of 175 °C, 15 MPa, and 5 min.....	53
Fig. 3-11: Thermogravimetric (TG) analysis of In ₂ O ₃ and ITO source solutions.....	54
Fig. 3-12: Differential thermal analysis (DTA) of In ₂ O ₃ and ITO source solutions.....	55
Fig. 3-13: Description of imprinted and non-imprinted films.....	56
Fig. 3-14: Hall mobility of imprinted and non-imprinted films after annealing at 600 °C.....	57
Fig. 3-15: FT-IR of In ₂ O ₃ and ITO gel films.....	58
Fig. 3-16: CSI-FT-ICR-MS analysis of (a) In ₂ O ₃ , (b) ITO via Sn(acac) ₂ , and (c) ITO via SnCl ₂	59
Fig. 3-17: Viscoelastic properties of (a) In ₂ O ₃ , (b) ITO via Sn(acac) ₂ , and (c) ITO via SnCl ₂	61
Fig. 3-18: SIMS profile of imprinted and non-imprinted In ₂ O ₃ and ITO films, after annealing.....	62
Fig. 3-19: XPS spectra of In ₂ O ₃ and ITO for oxygen 1s peak.....	64
Fig. 3-20: XRD of (a) imprinted and (b) non-imprinted, In ₂ O ₃ and ITO films.....	66
Fig. 4-1: Phase diagram of HfO ₂ from Massalski [27].....	73

Fig. 4-2: Formation of HfO ₂ solid thin film from source solution.....	75
Fig. 4-3: Patterning of ITO, and etching of HfO ₂ film, to make MIM capacitor.....	77
Fig. 4-4: Thermal behaviour of HfO ₂ source solution.....	79
Fig. 4-5: P-E and C-V of HfO ₂ films annealed at 500, 600, and 700 °C in O ₂ for 15 min.....	81
Fig. 4-6: J-E of HfO ₂ films annealed at 500, 600, and 700 °C in O ₂ for 15 min.....	82
Fig. 4-7: XRD of HfO ₂ films annealed at 500, 600, and 700 °C in O ₂ for 15 min.....	83
Fig. 4-8: AFM images of HfO ₂ films annealed at 500, 600, and 700 °C in O ₂ for 15 min.....	83
Fig. 4-9: Peel-off of Pt film from Pt/Ti/SiO ₂ /Si substrate at 800 °C annealing.....	84
Fig. 5-1: Process flow for TFT fabrication.....	92
Fig. 5-2: Top and side view of fabricated TFT by n-RP process.....	93
Fig. 5-3: Transfer characteristics of fabricated TFT by n-RP.....	95
Fig. 5-4: Output characteristics of fabricated TFT by n-RP.....	95
Fig. 5-5: Threshold voltage estimation of fabricated TFT by n-RP.....	96

Table of Contents

Abstract.....	i
Acknowledgement.....	iii
List of figures.....	v
1. Introduction.....	1
1.1 Introduction.....	1
1.2 High channel mobility and oxide semiconductors.....	1
1.3 Fabrication process of oxide semiconductors thin films.....	3
1.4 Smaller device size.....	6
1.5 Previous work.....	8
1.6 Device structure comparison by photolithography and n-RP.....	9
1.7 Objective of the thesis.....	10
2. Electrical Characterization of In₂O₃-based Thin Films by Solution Process.....	15
2.1 Introduction.....	15
2.2 Experimental procedure.....	18
2.3 Results and discussion.....	20
2.3.1 Thermal analysis.....	20
2.3.2 Electrical properties.....	22
2.3.3 Annealing temperature dependence.....	33
2.3.4 Work function measurements.....	37
Summary.....	39
3. Characterization of In₂O₃ and Indium-Tin-Oxide (ITO) Thin Films by Nano-Rheology Printing (n-RP).....	42
3.1 Introduction.....	42
3.2 Nano-rheological (n-RP) printing process.....	42
3.3 Experimental procedure.....	45

3.4 Results and discussion.....	49
3.4.1 Actual v/s indicated temperature.....	49
3.4.2 Pattern formation.....	49
3.4.3 Patterns of In ₂ O ₃ and ITO.....	52
3.4.4 Electrical properties.....	55
3.5 Discussion.....	57
Summary.....	67
4. Solution Derived High k-dielectric Materials.....	71
4.1 Introduction.....	71
4.2 Experimental procedure.....	74
4.3 Results and discussion.....	78
Summary.....	85
5. In₂O₃ Channel Thin Film Transistor (TFT) by Solution Process and n-RP.....	88
5.1 Introduction.....	88
5.2 Fabrication process.....	90
5.3 Results and discussion.....	93
Summary.....	97
6. Conclusion.....	99
6.1 Summary and conclusions of in this research.....	99
6.2 Future prospects of this study.....	101

1. Introduction

1.1 Introduction

Thin film transistors (TFTs) are used in almost every electronic equipments in today's era, or, it can also be said that TFTs are used in flat-panel displays, smart phones, video games, camera recorders, etc. The requirements of the electronic industry are to have low-power consumption, high throughput with low-cost, and high resolution for display applications. These requirements can be fulfilled by having high mobility of the channel and having smaller device size. In addition, a new low-cost, low-energy TFT fabrication process is required.

1.2 High channel mobility and oxide semiconductors

In conventional flat-panel displays, amorphous silicon (a-Si) is used as a channel in TFT. The advantages of using a-Si as a channel is that it is cheap, but the drawback is that it provides low mobility of around $1 \text{ cm}^2/\text{Vs}$. The alternate to a-Si is oxide semiconductors. The advantages of using oxide semiconductors is that they are cheap and they provide high mobility of around $10 \text{ cm}^2/\text{Vs}$.

There are various kinds of oxide semiconductors, which are metal oxides such as In_2O_3 , ZnO , In-Ga-Zn-O (IGZO) and etc. Since some of such metal oxides have large band gap, they are transparent for visible light and can be categorized into different materials named as transparent semiconducting oxides (TSO) and transparent conducting oxides (TCO). TCOs and TSOs are wide band-gap semiconductors (bandgap $> 3 \text{ eV}$) and the TCOs have a relatively high concentration of free electrons in its conduction band. This high carrier concentration arises either from defects in the materials or from extrinsic dopant which generate, the impurity levels located near the conduction band edge [1]. The high-electron-carrier concentration (the

materials will be assumed to be n-type unless otherwise specified) causes absorption of electromagnetic radiation in both the visible and infrared portions of the spectrum [2, 3]. These materials have large metal cation with an electronic configuration of $(n-1)d^{10}ns^0$ ($n \geq 4$). The valance band maximum (VBM) is composed of O $2p$ states and the conduction band minimum (CBM) composed of metal s orbital leading to ionic bonding. Also, these materials have small oxygen anion. Zinc oxide (ZnO), indium oxide (In_2O_3), tin oxide (SnO_2), gallium oxide (Ga_2O_3), etc. are examples of TSOs, while indium-tin-oxide (ITO), gallium-indium-zinc-oxide (GIZO), indium-zinc-oxide (IZO), etc. are examples of TCOs. In_2O_3 , ZnO, SnO_2 , etc. are binary compounds in the category of transparent electronics, while ITO, IZO, etc. are ternary compounds, and GIZO is quaternary compounds. Amongst these, In_2O_3 and ITO are very mature material, which are used as a transparent electrode in TFT-LCDs and touchscreens [4, 5], solar cells [6], electrochromic devices [7], or in organic light emitting diodes [8]. In_2O_3 doped with tin (Sn), is known as ITO, or $\text{In}_2\text{O}_3:\text{Sn}$. As shown in Fig. 1-1, most of the post-transition metals are included in the category of TSO and TCO.

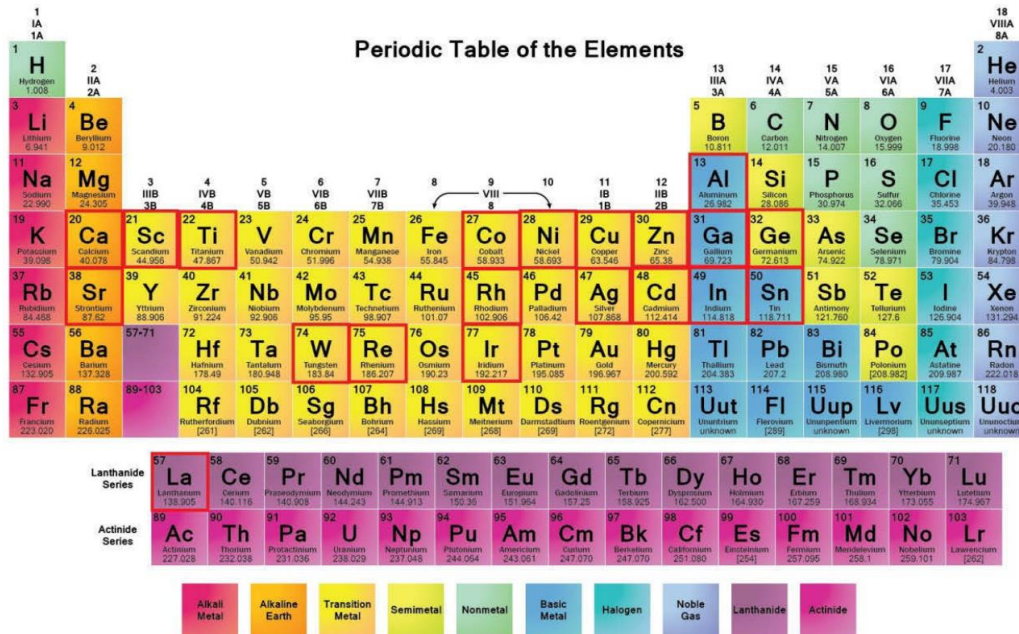


Fig. 1-1: Periodic table with associated elements as cations in transparent conductive oxides compounds, marked with red box [9].

The importance of TCO and TSO depends largely on the reproducibility, performance, and cost of transparent transistors. Thin film transistors (TFTs) are the key components in almost all of the modern flat-panel display. High-performance silicon transistors, which are used in amplifier or microprocessors; and are known by metal-oxide-semiconductor transistors (MOSFETs), require processing temperatures above 1000 °C. On the contrary, there are other types of transistors for large area electronics, which require lower process temperature and cost. The most commonly used are the “thin-film transistors (TFTs)”, which are immediately associated with liquid crystal displays (LCDs), where they allow one to switch each pixel of an image *on* or *off* independently.

1.3 Fabrication process of oxide semiconductors thin films

Conventional ways to deposit oxide thin films are categorized into two process:

- Physical process
- Chemical process

The principle of physical method relies on the evaporation or gasification of the material from a source, i.e. evaporation or sputtering, whereas in chemical process the substrate is exposed to one or more volatile precursors, which react and/or decompose on the substrate surface to produce the desired thin film. These techniques are shown in more details in Fig. 1-2.

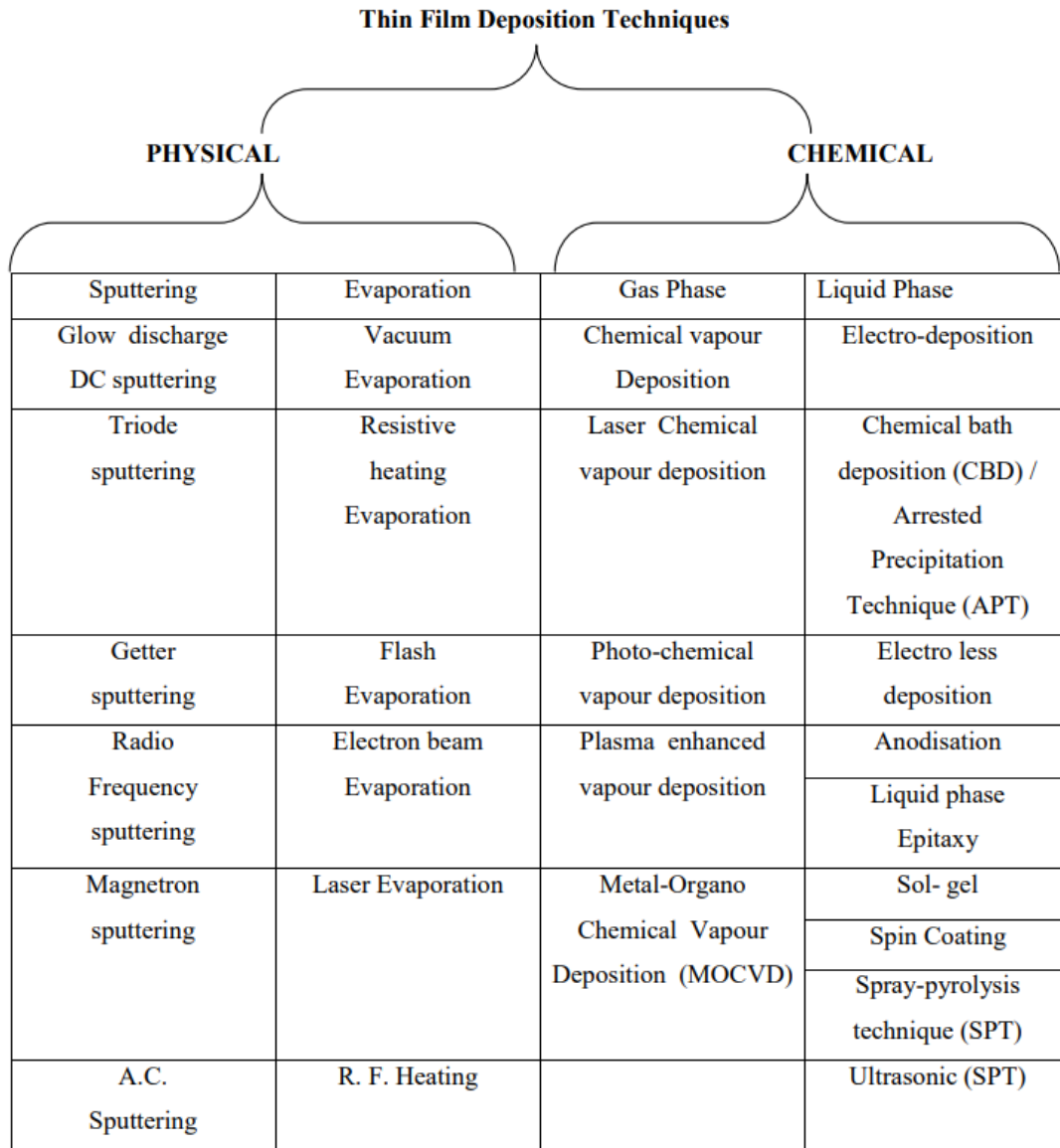


Fig. 1-2: Thin film deposition techniques.

Among them, the commercial and commonly used are RF and DC sputtering, pulsed laser deposition (PLD), chemical vapor deposition (CVD), vacuum evaporation, etc. [10-15]. These techniques provide good quality thin films, but the drawbacks with these technologies is that they need vacuum system, which means costly equipments and time consuming processes. On the other hand, wet chemical methods to fabricate thin films have potentially many applications compared to these physical methods, like they are less expensive, relatively simple, and the precise control over composition, etc. Another advantage of the wet techniques (which we have used in this work) is that these techniques are compatible with printing technology [16, 17].

Most common wet techniques (or solution process techniques) include, spin-coating, dip-coating, and spray-coating. They all have common processing route, which is shown in Fig. 1-3, while spin-coating, dip-coating, and spray-coating are shown schematically in Fig. 1-4.

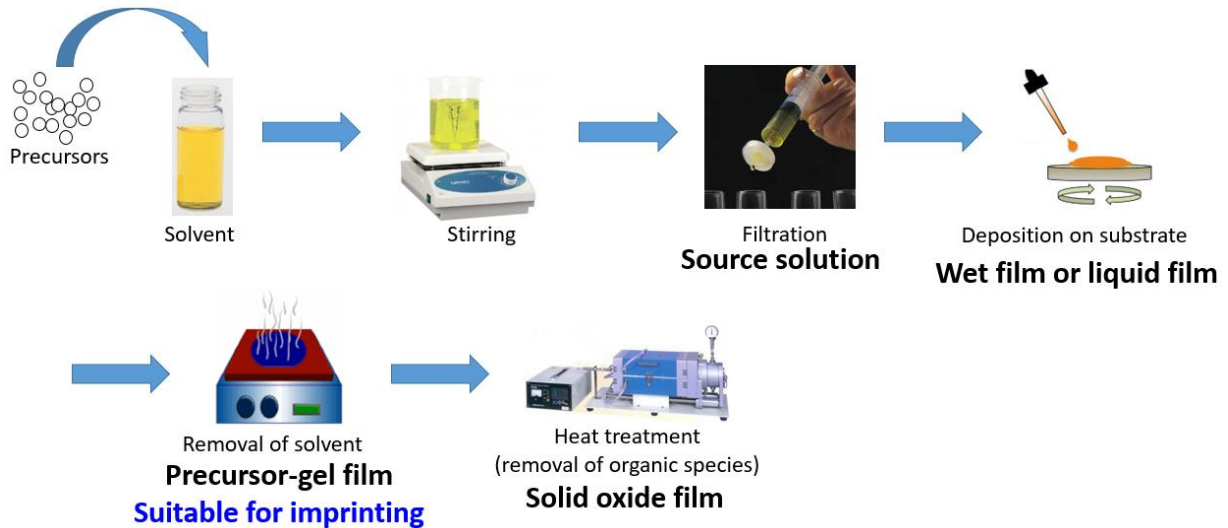


Fig. 1-3: Schematic of typical solution processing routes [18].

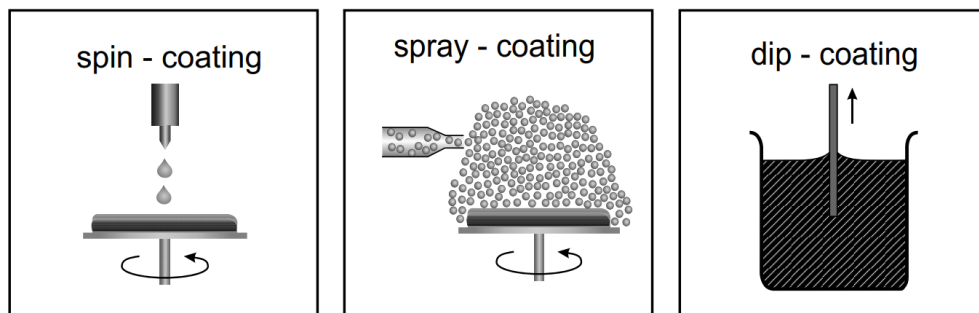


Fig. 1-4: Illustration of commonly used coating techniques [19].

Amongst these, we have used spin-coating throughout our work due to its ease of availability and simplicity. Spin-coating process schematic Fig. 1-5. The process goes like:

Step 1: The substrate is first put on chuck of the spin-coater and hold by vacuum, so that during spinning, the substrate cannot be thrown away.

Step 2: Then sample solution is dispensed on the substrate.

Step 3: The substrate is first rotated at low rpm, so that, the solution can be spread uniformly on the substrate.

Step 4: Then the spin rpm is increased as per our requirement of the thickness. By varying the spin rpm of this step, we can change the thickness of the film.

Step 5: Finally, after spin-coating, we get the film on the substrate. This film is known as liquid or wet film.

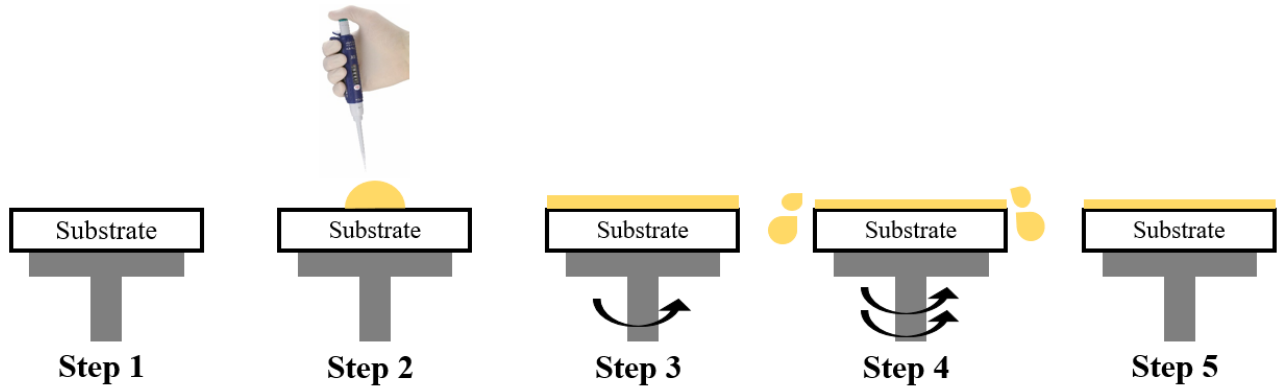


Fig. 1-5: Spin-coating schematic.

1.4 Smaller device size

As stated earlier, that oxide materials are used in many applications and TFT is one of them. For TFT application, the desired channel length should be in sub-micron range for future applications. The ways to get this range of channel lengths include a mechanically molded well [20], electron beam lithography [21], cold welding metal transfer [22], ultraviolet-nanoimprint lithography [23], and film profile engineering [24], and so on. These technologies are successful to fabricate sub-micron channel length TFTs, but they need vacuum technology, which means more time-consuming and costly. On the other hand, printing techniques offers several advantages in manufacturing electronics (known as printed electronics) such as the reduction of material waste, a short processing time, low-equipment cost, possibility of producing circuits on flexible substrates and reproducibility with high-resolution. Printed electronics means a group of techniques which are used to create electronic devices and circuits on low-cost substrates like glass, wood, paper, textile, and polymer. Commonly used printed

electronics techniques are screen printing, ink-jet printing, flexography, gravure printing, nanoimprint lithography, etc.

Among these categories of printed electronics, inkjet printing has gained much attention due to its ability to make flexible/stretchable electronics via direct writing with advantages of low material consumption and high efficiency. But it suffers from the problems are low conductivity of printed circuits, instable printing due to nozzle clog and misdirection jetting, weak adhesion between the printed materials and the substrates, low resolution, limited choices of substrate materials, and relatively high cost due to the use of Ag or Au nanoparticle based conductive inks. Also sometimes, when the solvent evaporates, then the patterns loses its fidelity e.g., a parrelloiped becomes spherical from the edges. If anyhow, we can improve the resolution of printing techniques, then we can reduce the cost and material consumption, by increasing the throughput.

A novel imprinting method, named as nano-rheology printing (n-RP) technology is a direct thermal-imprinting process for printing of metal-oxide [25, 26]. Using n-RP, patterns with a few tens of nanometres resolution are possible without the need of any sacrificing resist material. The process relies on viscoelastic transformation (softening) and metal-oxide condensation during printing, which makes n-RP different from other direct nano-imprinting methods. The printed features experience little shrinkage or deformation in post-annealing, thus it is possible to fabricate oxide patterns with a high shape fidelity to the mold, resulting in a well-defined shape with high precision and the possibility of scaling down the pattern size to a few tens of nanometres.

Using n-RP, we can make patterns, we can also make electrodes (by dry-etching) the residual film or we can also make TFTs using n-RP (we have used this application of n-RP in this work).

1.5 Previous work

n-RP was developed by Prof. Shimoda and his group in JAIST [27]. They studied the patterning properties of indium tin oxide (ITO), indium gallium zinc oxide (IGZO), and tin oxide (SnO). The result of patterning properties of ITO, IGZO, and SnO, imprinted via n-RP is shown in Fig. 1-6 [26]. For this work, they used PH-350 mold from NTT-AT. Apart from this Shimoda *et al.* also studied the patterning properties of Ru-La-O oxides, which is shown in Fig. 1-7 [27], where they used a Si mold (NIM-80L Reso, NTT-AT). Apart from these patterning properties, Shimoda *et al.* used n-RP process to fabricate TFTs, where gate electrode, source/drain, and channel, all were fabricated by n-RP.

Our lab has also fabricated TFT by n-RP process, using In_2O_3 and ITO as channel layer but used ferroelectric gate insulator i.e. $(\text{Bi},\text{La})_4\text{Ti}_3\text{O}_{12}$ (BLT) [28]. The transfer characteristics of the TFT fabricated previously in our lab is shown in Fig. 1-8.

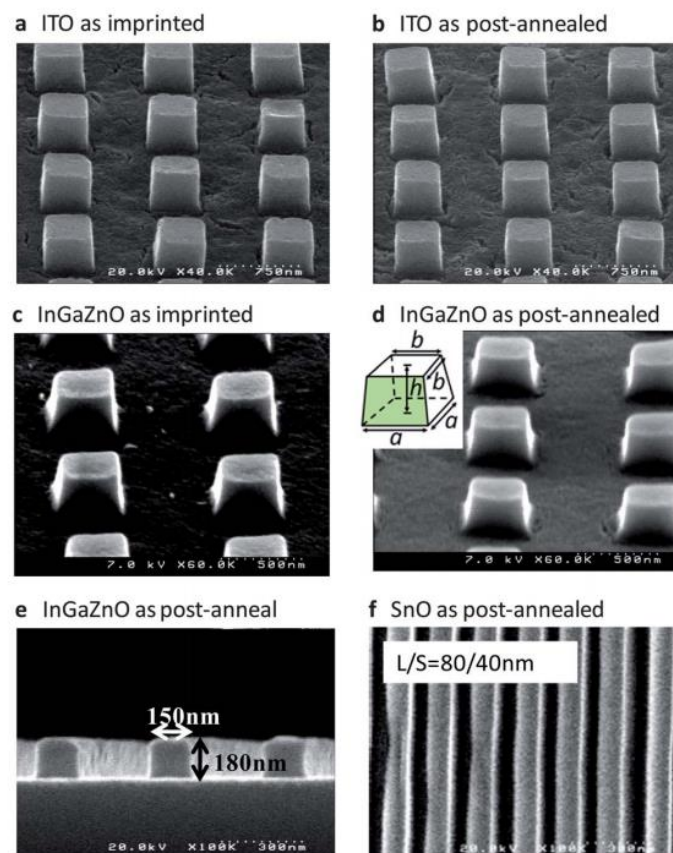


Fig. 1-6: Patterning properties of ITO, IGZO, and SnO, studied by Shimoda et al. [26].

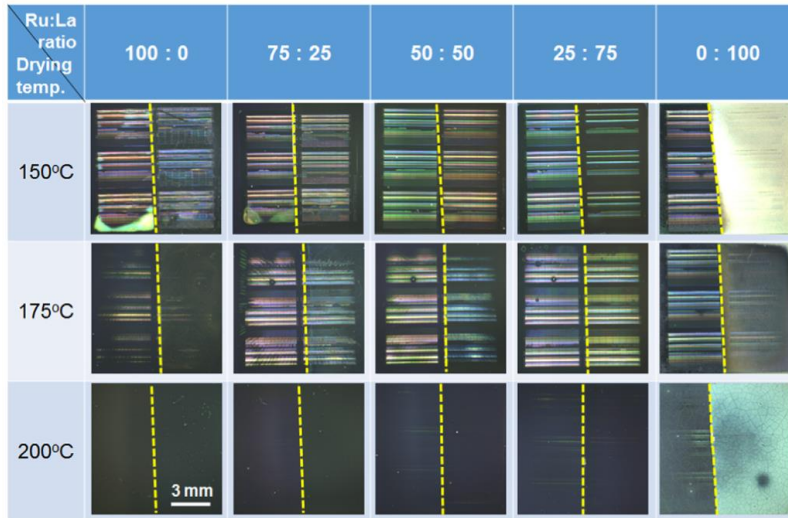


Fig. 1-7: Patterning properties of Ru-La-O, studied by Shimoda et al. by n-RP [27].

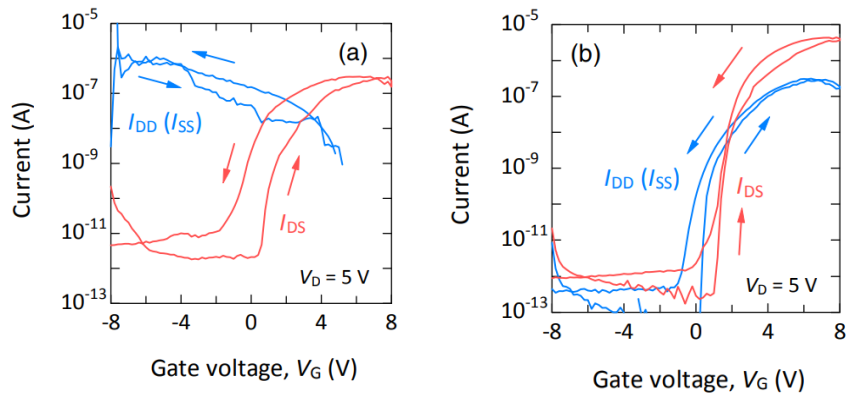


Fig. 1-8: Transfer characteristics of TFT fabricated using (a) ITO and (b) In_2O_3 , as channel with BLT as ferroelectric gate insulator, by Haga et al. [28].

1.6 Device structure comparison by photolithography and n-RP

Figure 1-9 shows the TFT fabricated by photolithography and by n-RP; and it is seen from Fig. 1-9, that when TFT is fabricated by conventional photolithography, then source/drain can be any metal, or heavily doped Si or ITO. The channel can be a-Si or oxide semiconductor, while the gate dielectric can be SiO_2 or Si_3N_4 or ferroelectric gate insulator. On the contrary, when we fabricate TFT by n-RP process, the source/drain and channel, all are fabricated simultaneously and that too by the same material. The thick regions act as source/drain while the thin region acts as channel. Since the channel is conductive oxide, so the gate insulator has

to be ferroelectric gate material or high- k gate insulator (provided that the charge density of the gate insulator is greater than the charge density of the channel).

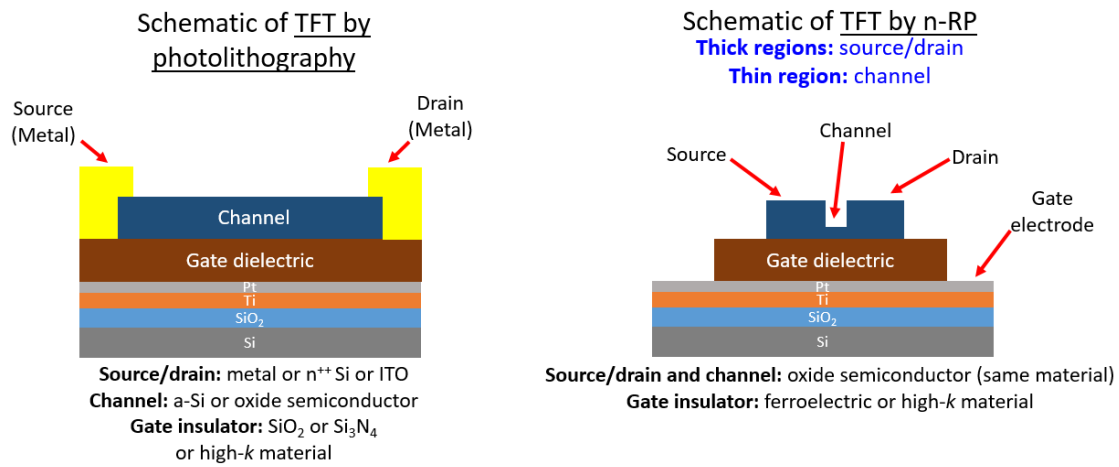


Fig. 1-9: Comparison of TFT fabrication by photolithography and n-RP.

1.7 Objective of the thesis

The aim of this thesis is to fabricate thin film transistor (TFT) by novel imprinting technique, known as “nano-rheology printing (n-RP)” using solution process derived indium oxide (In₂O₃) as channel layer and source/drain; and solution process derived hafnium oxide (HfO₂) as gate dielectric material. Using n-RP, source/drain and channel are formed simultaneously. Therefore, in the fabricated TFT, source/drain and channel are made up of In₂O₃. Platinum (Pt) is used as gate electrode.

To do this, first we fabricated solution processed indium oxide (In₂O₃) and indium tin oxide (ITO) thin film using indium acetylacetonate (In(acac)₃) precursor in propionic acid (PrA) for In₂O₃. For ITO, we used two different tin precursors. One was tin chloride (SnCl₂) and another was tin acetylacetonate (Sn(acac)₂). Therefore, the source solutions of ITO were prepared by SnCl₂ and In(acac)₃ in PrA; and Sn(acac)₂ and In(acac)₃ in PrA. After the film deposition of thin films of In₂O₃ and ITO, they were optimized by changing annealing time and annealing

temperature to get good electrical properties (i.e. high mobility and carrier concentration). Mobility and carrier concentration were measured using Hall measurement set-up.

After getting the best condition of high mobility and carrier concentration, we again characterized In_2O_3 and ITO by n-RP technique. This characterization was done in terms of patterning and electrical properties. Patterning properties were studied using SNP-02 checker mold, the condition at which best patterns are obtained, is found. Using this condition, we again imprinted In_2O_3 and ITO thin films using flat mold by n-RP technique to study the electrical properties. After imprinting, annealing was done using the conditions obtained above (discussed in the above paragraph). A comparison of electrical properties of imprinted and non-imprinted films was done. The complete mechanism for the change in electrical properties after imprinting was also studied. Until now there are numerous research done on the patterning properties of In_2O_3 -based oxide semiconductors. However, few research are available for the study of electrical properties (i.e. Hall mobility and carrier concentration) via imprinting technique.

In_2O_3 and ITO have high carrier concentration, so they need to be depleted, in order to get low off-current, when they are used as channel of TFT. This depletion is done by using ferroelectric gate insulator due to their large remnant polarization. Instead of ferroelectric gate insulator, a paraelectric gate insulator can also be used if the induced charge density is sufficient, in this case we can use TFT for display applications, while with ferroelectric gate, we can use TFTs for memory applications due to the presence of memory window. In this work, we used high- k hafnium oxide (HfO_2) as gate insulator. HfO_2 was fabricated by solution process using hafnium acetylacetonate ($\text{Hf}(\text{acac})_4$) in PrA. HfO_2 thin films were also optimized by changing annealing conditions, to get its good electrical properties, which means low leakage current density and high breakdown field strength.

Using all the above optimized condition, TFT was fabricated using Pt as bottom gate electrode, In_2O_3 as source/drain and channel, and HfO_2 as a gate dielectric. In_2O_3 and HfO_2 , both were fabricated via solution process. Bottom gate is used as the crystallization temperature of HfO_2 is higher than that of In_2O_3 .

Previous work on n-RP by Shimoda *et al.* was done on the patterning properties of ITO and Ru-La-O oxides, but they did not study the mechanism of patterning properties with addition of Sn in In_2O_3 . Also, previous work was done only on the patterning properties, no work was done on the electrical properties. Previous work of Haga *et al.* from our laboratory, also did not study the electrical properties and they fabricated FeTFT using BLT as gate insulator, which is different from the gate insulator (HfO_2) in this work.

References

1. N. R. Kim, J. H. Lee, Y. Y. Lee, D. H. Nam, H. W. Yeon, S. Y. Lee, T. Y. Yang, Y. J. Lee, A. Chu, K. T. Nam, and Y. C. Joo, *J. Mater. Chem. C.*, **1** (2013) 5953.
2. M. Gross, N. Linse, I. Maksimenko, and P. J. Wellmann, *Adv. Eng. Mater.*, **11** (2009) 295.
3. N. A. Dahoudi and M. A. Aegerter, *Thin Solid Films*, **502** (2006) 193.
4. M. Katayama, *Thin Solid Films*, **341** (1999) 140.
5. M. Gaillet, L. Yan, and E. Teboul, *Thin Solid Films*, **516** (2007) 170.
6. K. G. Gopchandran, B. Joseph, J. T. Abraham, P. Koshy, and C. G. Granqvist, *Vacuum*, **86** (1997) 547.
7. C. G. Granqvist, *Nat. Mater.*, **5** (2006) 89.
8. W. Kowalsky, P. Gorn, J. Meyer, M. Korger, H. H. Johannes, T. Riedl, *Proc. SPIE*, (2007) 68860F.
9. D. S. Ginley, H. Hosono, and D. C. Paine, *Handbook of Transparent Conductors* (Springer, New York Heidelberg Dordrecht London, 2010).
10. D. S. Ginley and C. Bright, *MRS. Bull.*, **25** (2000) 15.
11. K. L. Chopra, S. Major, and D. K. Pandya, *Thin Solid Films*, **102** (1983) 1.
12. C. G. Granqvist and A. Hultaker, *Thin Solid Films*, **411** (2002) 1.
13. V. Muler, M. Rasp, J. Rathously, B. Schutz, M. Niederberger, and D. Fattakhova, *Small.*, **6** (2010) 633.
14. R. B. H. Tahar, T. Ban, Y. Ohya, and Y. Takahashi, *J. Appl. Phys.*, **83** (1998) 2631.
15. E. N. Dattoli and W. Lu, *MRS Bull.*, **36** (2011) 782.
16. D. S. Hecht and R. B. Kaner, *MRS. Bull.*, **36** (2011) 749.
17. K. Nishio, T. Sei, T. Tsuchiya, *J. Mater. Sci.*, **31** (1996) 1761.
18. R. M. Pasquarelli, D. S. Ginley, and R. O'Hayre, *Chem. Soc. Rev.*, **40** (2011) 5406.

19. R. W. Schwartz, T. Schneller, and R. Waser, *C. R. Chimie.*, **7** (2004) 433.
20. F. Ganier, R. Hajlaouri, and M.E. Kassmi, *Appl. Phys. Lett.*, **73** (1998) 1721.
21. Song, S. Kim, H. Yin, C. J. Kim, J. Park, S. Kim, H. S. Choi, E. Lee, and Y. Park, *IEEE Electron Device Lett.*, **29** (2008) 549.
22. C. Kim, M. Shtein, and S. R. Forrestb, *Appl. Phys. Lett.*, **80** (2002) 4051.
23. M. D. Austina and S. Y. Chou, *Appl. Phys. Lett.*, **81** (2002) 4431.
24. C. H. Lin, R. J. Lyu, and T. Y. Huang, *IEEE Electron Devices Lett.*, **80** (2013) 1160.
25. T. T. Phan, J. Li, and T. Shimoda, *Nano Futures.*, **2** (2018) 035006.
26. T. Kaneda, D. Hirose, T. Miyasako, P. T. Tue, Y. Murakami, S. Kohara, J. Li, T. Mitani, E. Tokumitsu, and T. Shimoda, *J. Mater. Chem.*, **2** (2014) 40.
27. K. Nagahara, D. Hirose, J. Li, J. Mihara, and T. Shimoda, *Ceramics International*, **42** (2016) 7730.
28. K. Haga, Y. Kamiya, and E. Tokumitsu, *Jpn. J. Appl. Phys.* **57** (2018) 02CB14.

2. Electrical Characterization of In₂O₃-based Thin Films by Solution Process

2.1 Introduction

Indium oxide (In₂O₃) has been a material of interest for researchers over past many years. When it is doped with tin, the material is then known as indium tin oxide (ITO). In₂O₃ is commonly known as transparent oxide semiconductor oxide (TSO), while ITO is known as transparent conducting oxide (TCO).

In₂O₃ shows n-type conduction. This n-type conduction is due to oxygen vacancy in In₂O₃ (or, In₂O_{3-x}), pronounced as non-stoichiometry intrinsic defect. Such kinds of defects get enhanced when we anneal TSO/TCO in reducing environment. On the other hand, ITO has low resistivity (or high conductivity), usually less than 10⁻⁴ Ωcm [1]. ITO is also known as degenerate wide band-gap material. This is because Sn donates its one e⁻ to In₂O₃ crystal structure, by replacing In³⁺ and forms Sn⁴⁺. So, in ITO, high conductivity is due to two reasons:-

- a. oxygen vacancies that provide electrons by acting as doubly charged donors [$V_o^{\cdot\cdot}$].
- b. donation of electron by tin substitution thereby acting as a singly charged donor on an indium site [Sn_{In}].

Another advantage of In₂O₃ and ITO is that they have high visibility (> 80 %) in visible light.

Due to the advantages of high conductivity and high optical transparency in visible light, ITO has many applications. Some of them are transparent conductive electrodes [2, 3], heat reflecting filters for energy saving purposes [4, 5], flat panel displays [6], ITO coatings are used in optoelectronic coatings like in solar cells, electrochromic windows [7], liquid-crystal displays [8], information displays [9], etc.

As stated above, Sn doped In_2O_3 is ITO. Sn substitute In in In_2O_3 crystal structure. So, it is necessary to study In_2O_3 crystal structure. In_2O_3 has three different crystal polymorphs referred as In_2O_3 -c, In_2O_3 -rh, and In_2O_3 -o. In_2O_3 -c, In_2O_3 -rh, and In_2O_3 -o stand for cubic, rhombohedral, and orthorhombic, respectively. Among these three crystal polymorphs, In_2O_3 -o and In_2O_3 -rh are rarely studied, hence, few papers are available on its crystal structure [10, 11] as they are high pressure phase. In_2O_3 -c phase is the most studied phase. The difference in these polymorphs is the linkage of InO_6 octahedra. This is discussed in next paragraph, starting with cubic bixbyite structure.

In_2O_3 -c (from now on, only In_2O_3) crystallizes into cubic bixbyite structure. Cubic bixbyite is a “2 x 2 x 2” fluorite derived lattice, with one-quarter of the anions missing (known as “structural vacancies”). Each bixbyite structure has 16 formula units of In_2O_3 per unit cells, i.e. 80 atoms ($2 \text{ In} + 3 \text{ O} = 5$ and $5 \times 16 = 80$ atoms), out of these 80 atoms, 32 are indium atoms and 48 are oxygen atoms. A cubic bixbyite also has 16 oxygen vacancies, along with 80 atoms of indium and oxygen. The 32 indium atoms are categorized as In-b (8 atoms/unit cell, also called as $8b$, b stands for body-diagonal) and In-d (24 atoms/unit cell, also called as $24d$, d stands for diagonal). In the crystalline structure, the oxygen atoms are octahedrally coordinated around indium, which means that all indium cations are surrounded by six oxygen atoms and two structural vacancies. The structural vacancy positions can be along the body diagonal (b-site) or along a face diagonal (d-site). The b-site and d-site represent 25% and 75% of the octahedra arrangement, respectively. In the b-site arrangement, all the oxygens are equidistant from the indium, while in the d-site arrangement, they are not. Due to the presence of structural vacancies, there are two configurations by which InO_6 octahedra link together in crystalline In_2O_3 . The first one is the one in which both i.e. an oxygen and a structural vacancy, are shared between adjacent polyhedra leading to the fact that the polyhedral are only joined at a corner, hence “corner sharing”. The second one is the one in which two oxygens are shared between

the adjacent polyhedra with the end result that the polyhedra are joined along the entire edge, “edge sharing” [12]. A schematic of crystalline In_2O_3 bixbyite is shown in Fig 2-1.

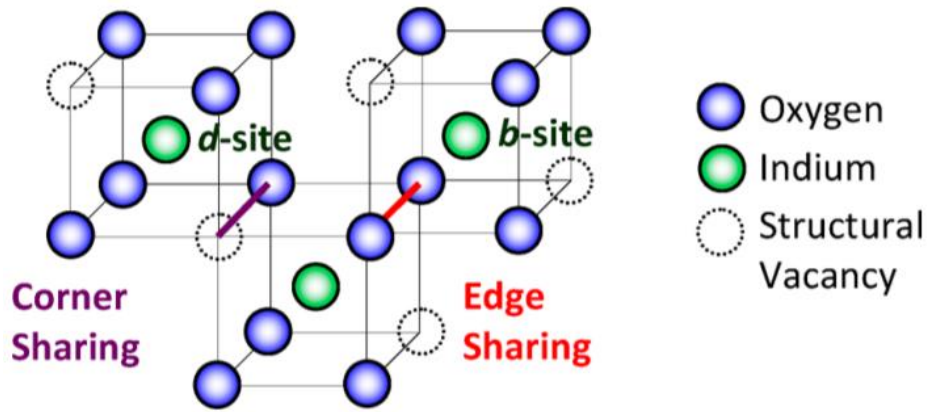


Fig. 2-1: Schematic of crystalline In_2O_3 bixbyite.

In cubic structure, two InO_6 are connected either, by corners sharing or edge sharing, while in other polymorphs, they are also connected along the faces.

The electrical properties (resistivity, carrier concentration, and Hall mobility) of In_2O_3 and ITO depend on the fabrication process and annealing environment. There are many ways to deposit In_2O_3 -derived films, like r.f. sputtering, d.c. sputtering, magnetron sputtering, pulsed laser deposition (PLD), electron beam deposition, spray pyrolysis, sol-gel techniques, etc. [13-15]. Most widely adopted industrial process is sputtering, which produces high quality films. Sputtering or other techniques like PLD, need vacuum equipments; and hence the method becomes time consuming and costly. On the other hand, the solution processed films are relatively simple to deposit and less expensive. Other advantages of solution process are less time consuming, and precise control over doping. However, the film quality in terms of electrical properties of solution processed films is generally not as good as films by sputtering because solution processed films are sometimes porous due to the evaporation of solvent and gaseous decomposition products [16] and porosity results in low mobility.

Annealing environment also plays an important role in determining the electrical properties of ITO. Oxidizing environment (e.g. O₂) reduces the oxygen vacancies ($V_O^{\cdot\cdot}$) by providing oxygen into the vacant oxygen sites and hence carrier concentration reduces. Reducing environment (e.g. forming gas) enhances $V_O^{\cdot\cdot}$ and hence carrier concentration increases, which leads to more scattering and hence less mobility.

In this present work, we studied the electrical properties of In₂O₃ and ITO thin films prepared by the solution process using indium acetylacetonate (In(acac)₃) in propionic acid (PrA) for In₂O₃ thin films; and In(acac)₃ with tin chloride (SnCl₂) or with tin acetylacetonate (Sn(acac)₂) in PrA for ITO thin films. In(acac)₃ precursor is chosen because it has rheological properties, so the gel film of In₂O₃ or ITO prepared using In(acac)₃ precursor can be used for direct imprinting (this is discussed in next chapter). To the best of our knowledge, no research group has used these precursors earlier. A few researchers have used SnCl₂ as a precursor to make ITO but they used indium chloride (InCl₃) as indium precursor [17-19]. In this work, SnCl₂ and Sn(acac)₂ were selected. In Sn(acac)₂, the “acac” is an organic species which gets removed from the film during annealing, leaving behind Sn. While when SnCl₂ is used, Sn and Cl are expected to remain in the film, even after annealing. A comparison of the electrical properties is done with two different tin precursors.

2.2 Experimental procedure

The source solution of In₂O₃ was prepared by mixing In(acac)₃ in PrA while the source solutions of ITO were prepared by mixing Sn(acac)₂ or SnCl₂ and In(acac)₃ in PrA. The source solutions were prepared by mixing the precursors for 1 h at 120 °C at 1000 rpm. After 1 h stirring at 120 °C, the solution was allowed to cool down and then filtered using 0.2 μm pore sized filter paper. It was then spin-coated on SiO₂(200nm)/Si substrate at 1500 rpm for 20 s. This gave us liquid film. Then the sample was then dried on a hot plate at 100 °C in air for 3

min, to make the liquid film into a gel film (or, precursor film) by evaporating solvent. Finally, the gel film was annealed in rapid thermal annealing (RTA), by varying annealing conditions.

For In_2O_3 films, RTA annealing was done at 600 °C for 15 min to 90 min in steps of 15 min, while ITO films were annealed in RTA at 600 °C for 1 h. To study the temperature dependence, the films were annealed in RTA in O_2 environment for 1 h by varying the annealing temperature from 500 to 700 °C with steps of 100 °C. Complete process is shown in Figs. 2-2 and 2-3, where Fig. 2-2 is for In_2O_3 and Fig. 2-3 is for ITO films. Sn content in ITO films was varied from 1 wt.% to 10 wt.%. After annealing the films in RTA, the films were photolithographed and etched to remove the edge-effect, then the electrical characteristics were measured using Hall set-up at room temperature using van-der Pauw method.

Hall measurement system used was RESITEST 8400 by Toyo corp. The film thickness was measured using step profilometer (Alphastep-D500 by KLA tencor). Films crystallinity was checked using GI-XRD (X'Pert PRO MRD Epi from PANalytical) with accelerating voltage and current used were 45 V and 40 mA, respectively, while $\text{Cu-}\alpha$ X-rays were used. Atomic force microscope (AFM; AFM5000II SPA-400 by Hitachi), was used in dynamic force microscope (DFM) mode to measure the films morphology. Scanning electron microscopy (SEM; S-4500 by Hitachi), was also used to study the surface morphology of the films. The oxidation temperature (temperature at which the gel films become oxide films), were measured via thermal analysis (from Toshiba Nanoanalysis, Japan). The work functions of the films were measured by photoelectron spectrometer (AC-2 by Riken Keiki).

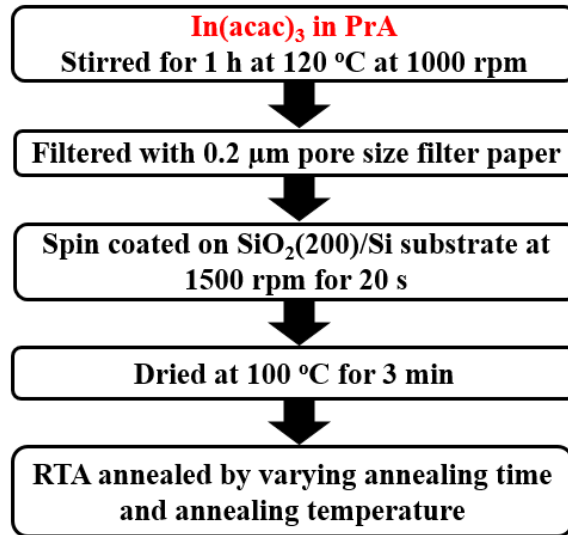


Fig. 2-2: Process flow for formation of In₂O₃ film on SiO₂ substrate.

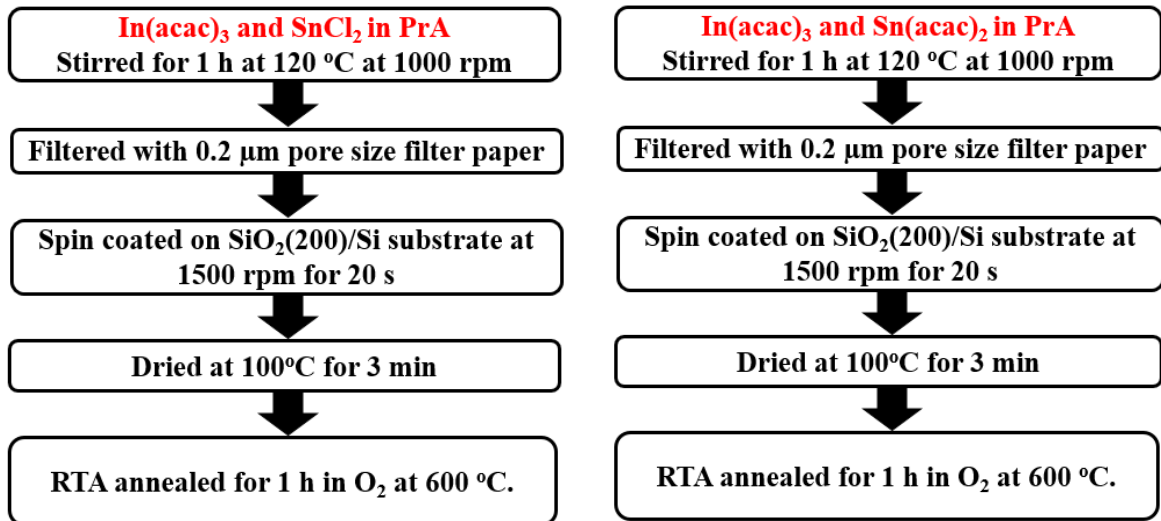


Fig. 2-3: Process flow for formation of ITO films by SnCl₂ and by Sn(acac)₂ precursors film on SiO₂ substrate.

2.3 Results and discussion

2.3.1 Thermal analysis

In₂O₃ and ITO films were synthesized by solution process in our work. Solution processed films become solid oxide films at a particular temperature, which is studied by thermogravimetric analysis (TG) and differential thermal analysis (DTA). TG-DTA are together known as thermal analysis.

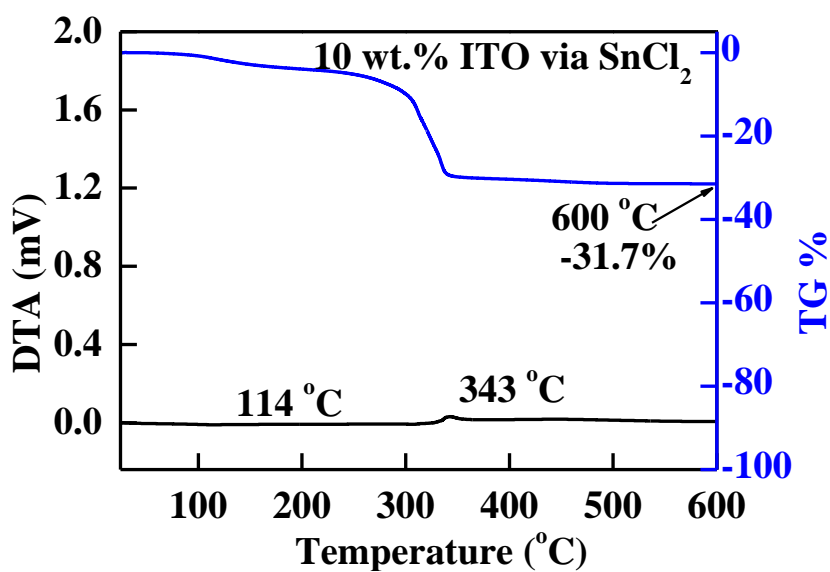
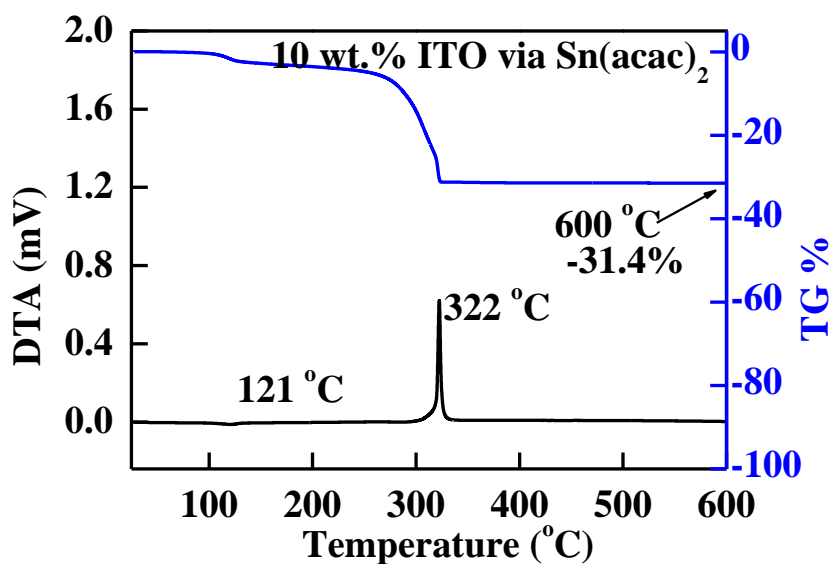
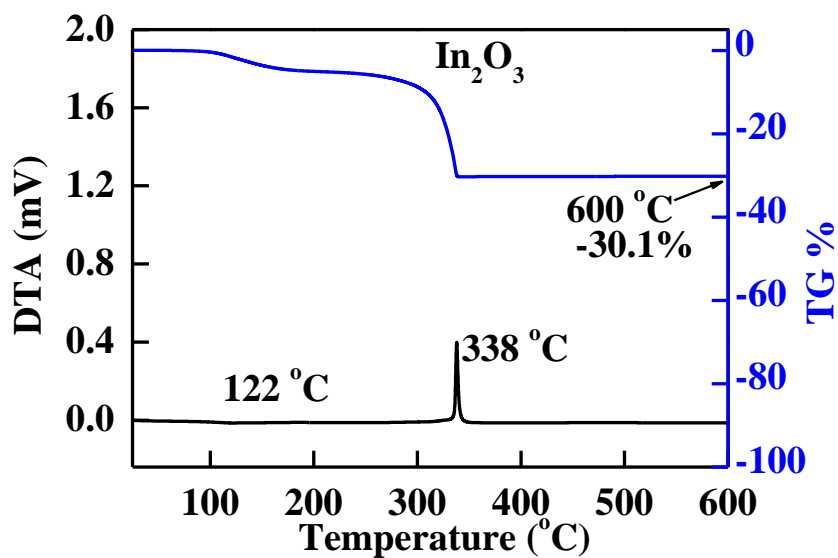


Fig. 2-4: TG-DTA analysis of In₂O₃ and ITO.

Thermal analysis behaviour of the In_2O_3 , 10 wt.% ITO via SnCl_2 , and 10 wt.% ITO via $\text{Sn}(\text{acac})_2$ is shown in Fig. 2-4. TG-DTA was measured in ambient air from room temperature ($25\text{ }^\circ\text{C}$) to $600\text{ }^\circ\text{C}$ at a heating rate of $10\text{ }^\circ\text{C min}^{-1}$. Air flow rate was 200 ml/min. Thermal behaviour indicates that In_2O_3 and ITO (herein after ITO via $\text{Sn}(\text{acac})_2$ and ITO via SnCl_2 are known together known as ITO, unless otherwise stated) solutions decomposed in two steps, because two weight loss regions were clearly observed in TG behaviour: one starts at around room temperature and ends at around $120\text{ }^\circ\text{C}$. This also corresponds to an endothermic peak at around $120\text{ }^\circ\text{C}$ in DTA. This peak indicates that the evaporation of solvent is completed at this temperature. The second weight loss region in TG starts at around $250\text{ }^\circ\text{C}$ and ends at approximately $350\text{ }^\circ\text{C}$. The positive peak in DTA at around $350\text{ }^\circ\text{C}$ corresponds to the crystallization of In_2O_3 and ITO by the decomposition and oxidation of organic species. Source solutions remain in gel state between 120 to $250\text{ }^\circ\text{C}$. N-RP imprinting is done in this gel-state of the films (discussed in next chapter).

2.3.2 Electrical properties

2.3.2.1 In_2O_3 films

As In_2O_3 and ITO gels become oxide at around $350\text{ }^\circ\text{C}$ (confirmed by thermal analysis), but it does not mean all the organics from the films have evaporated at this temperature. Organics still keep eliminating from the films with an increase of annealing temperature. At first In_2O_3 films were annealed in O_2 for 1 h by varying the annealing temperature from 500 to $700\text{ }^\circ\text{C}$. The Hall mobility and carrier concentration dependence on annealing temperature of In_2O_3 films is shown in Fig. 2-5. It is seen from Fig. 2-5 that as the annealing temperature increases, Hall mobility increases. This is due to the reason that with the increase of annealing temperature, more organic species are removed from the films and crystal structure of the films improve. This is shown in Fig. 2-6, which shows the crystal structure of the films. Figure 2-6 shows with

increasing annealing temperature, FWHM decreases, which means crystal structure improves or grain size increases.

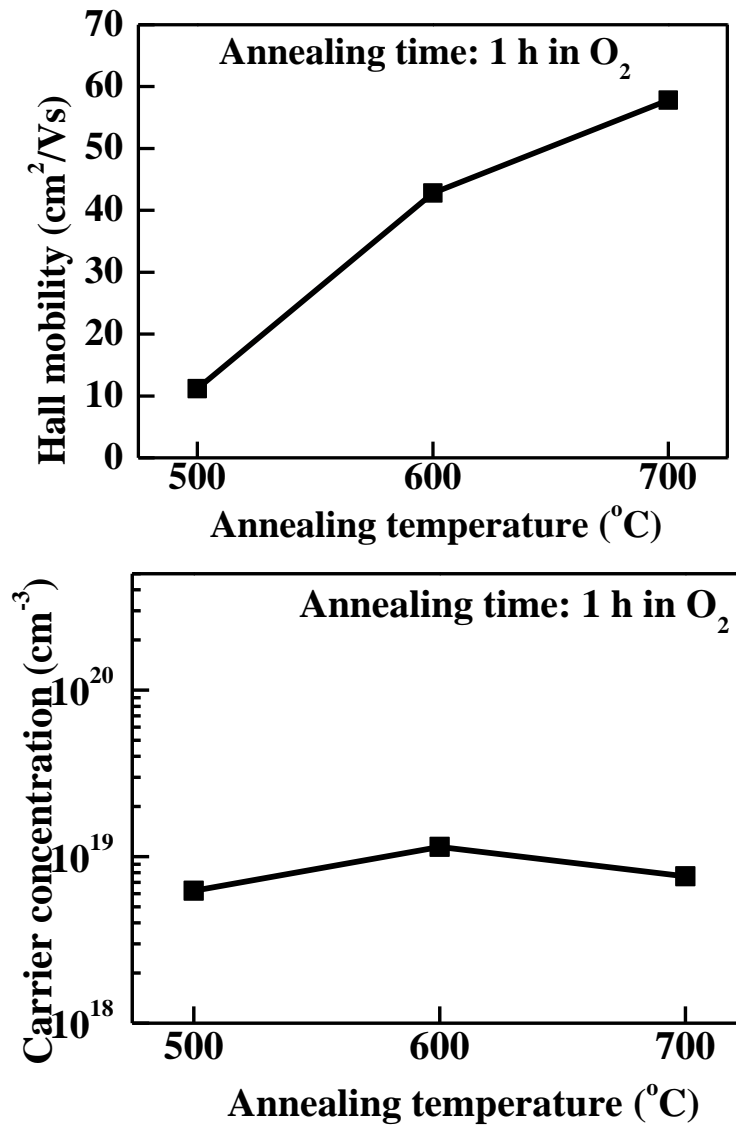


Fig. 2-5: Hall mobility and carrier concentration of In₂O₃ films with respect to annealing temperature.

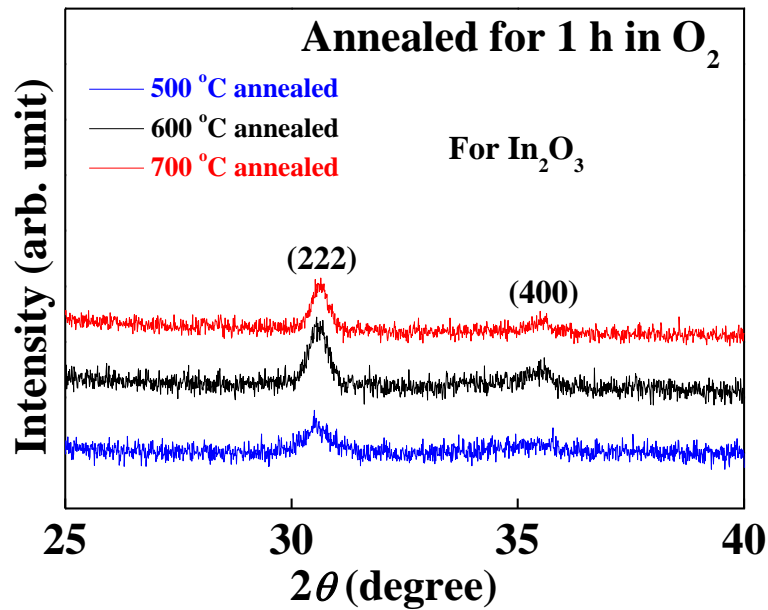


Fig. 2-6: XRD of In₂O₃ films with annealing temperature variation.

As In₂O₃ and ITO films are used in flat panel displays with glass substrate and with glass substrate, the maximum annealing temperature we can use is around 600 °C. So, further annealing is done in O₂ for 1 h at 600 °C. In₂O₃ films were annealed in O₂ at 600 °C, by varying annealing time. The results of Hall mobility and carrier concentration is shown in Fig. 2-7. It is seen from Fig. 2-7, that as annealing time increases from 15 to 60 min, Hall mobility first increases and then after 60 min, it starts to decrease. However, carrier concentration is constant with respect to annealing time. Initial increase and then decrease of Hall mobility can be understood by looking the SEM images of 15, 60, and 90 min annealed films.

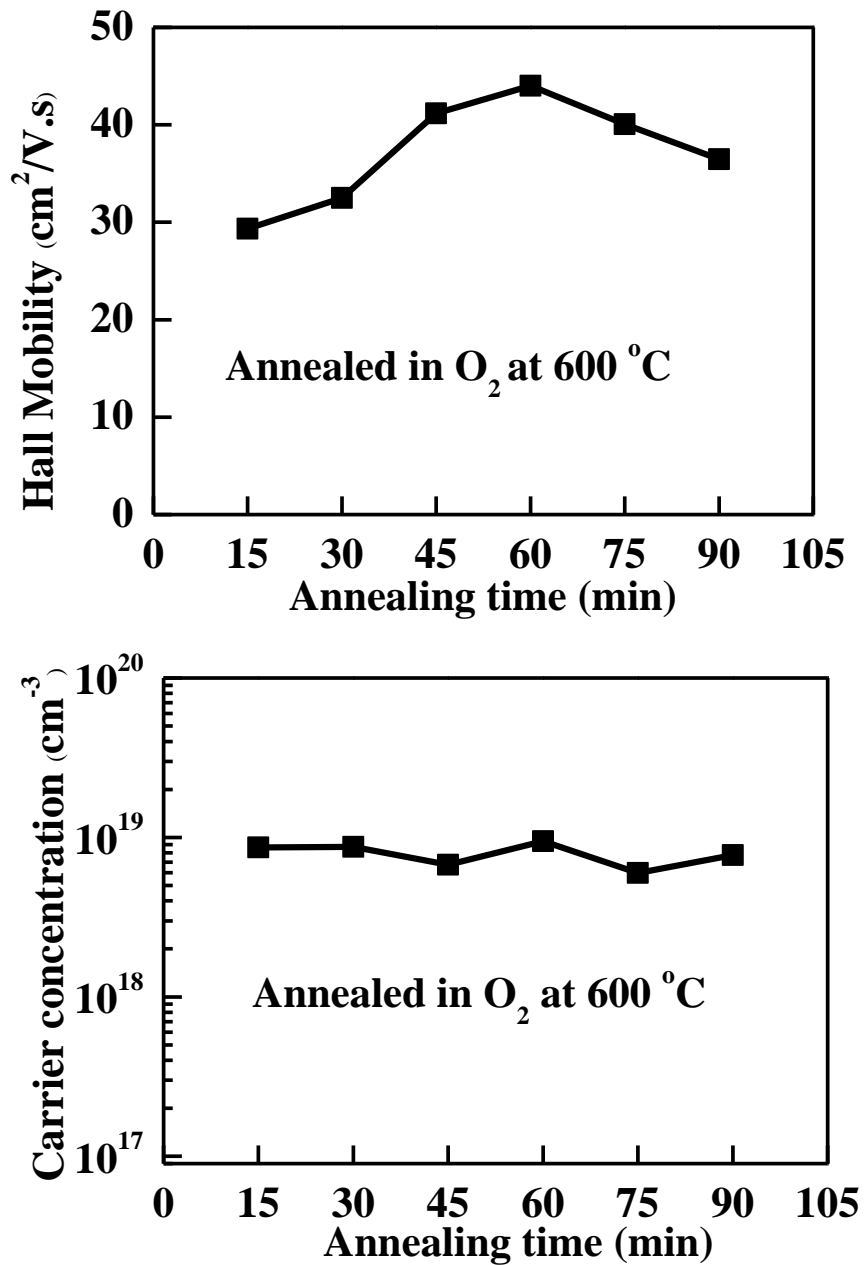


Fig. 2-7: Hall mobility and carrier concentration of In₂O₃ films.

SEM images of 15, 60, and 90 min annealed In₂O₃ films are shown in Fig. 2-8. From SEM images, it is seen that at longer annealing time (90 min), there is clustering in the films. This may be one of the reason for decrease in mobility at longer annealing times. The XRD result (Fig. 2-9) also shows that as annealing time increases, FWHM first decreases and then increase of FWHM at longer annealing time.

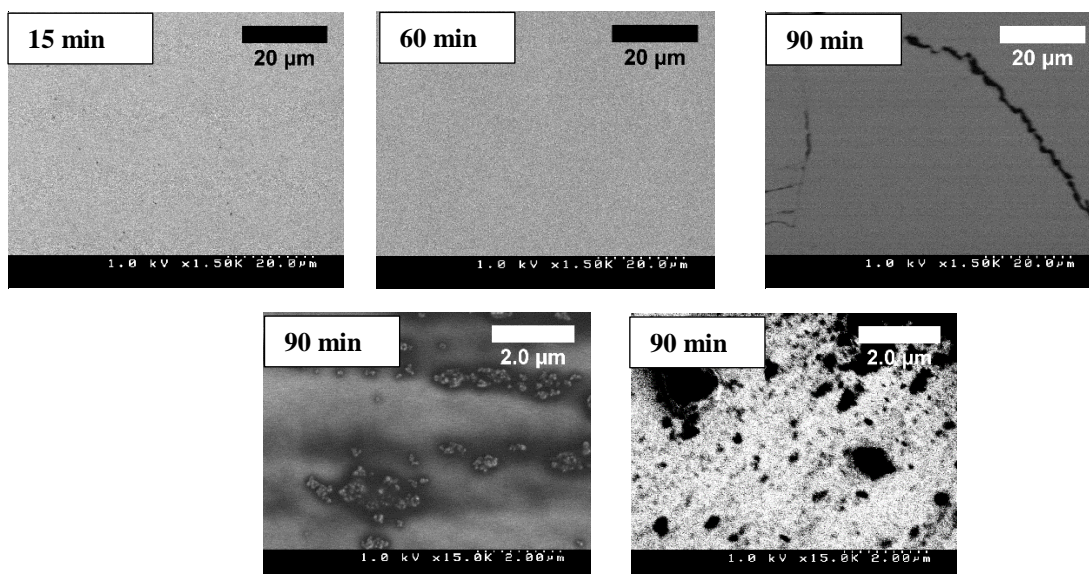


Fig. 2-8: SEM images of In_2O_3 films annealed for 15, 60, and 90 min.

Figure 2-9 shows the XRD of In_2O_3 films with time variation. It is also seen from the XRD results that as the annealing time increases from 15 min to 60 min, crystallinity increases (i.e. FWHM decreases), further increase of annealing time, FWHM increases. This is the reason for the increase of mobility, first and then decreases.

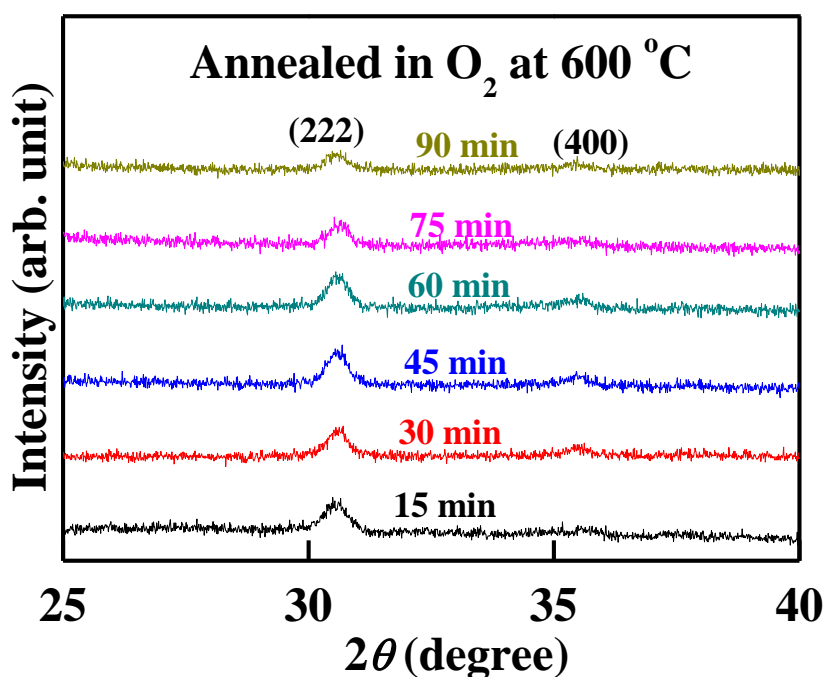


Fig. 2-9: XRD of In_2O_3 films by varying annealing time.

It is also interesting to note that as the annealing time increases, the average surface roughness increases. This is shown in Fig. 2-10, which shows the average surface roughness (R_a) dependence on annealing time for In_2O_3 . R_a was measured for an area of $2 \times 2 \mu\text{m}^2$. The surface roughness increases with increasing annealing time because of the reason that with increasing annealing time, crystallinity increases, so grains grow. Figure 2-11 shows the grains for 15, 60, and 90 min annealed In_2O_3 film, while Fig. 2-12 shows the thickness dependence of annealing time.

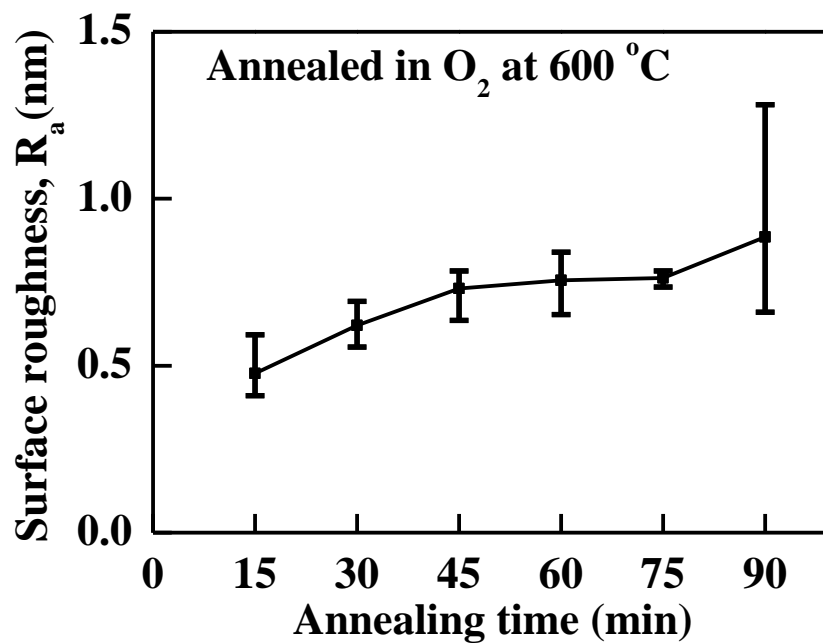


Fig. 2-10: Surface roughness of In_2O_3 films by varying annealing time.

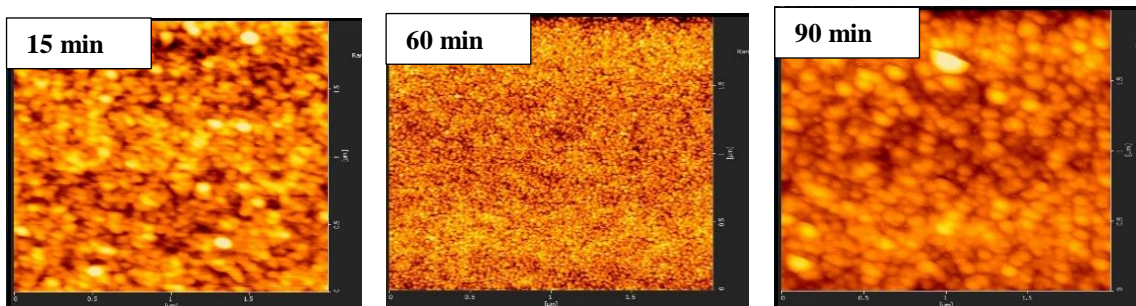


Fig. 2-11: AFM images of In_2O_3 films annealed for 15, 60, and 90 min in O_2 at $600 \text{ }^\circ\text{C}$.

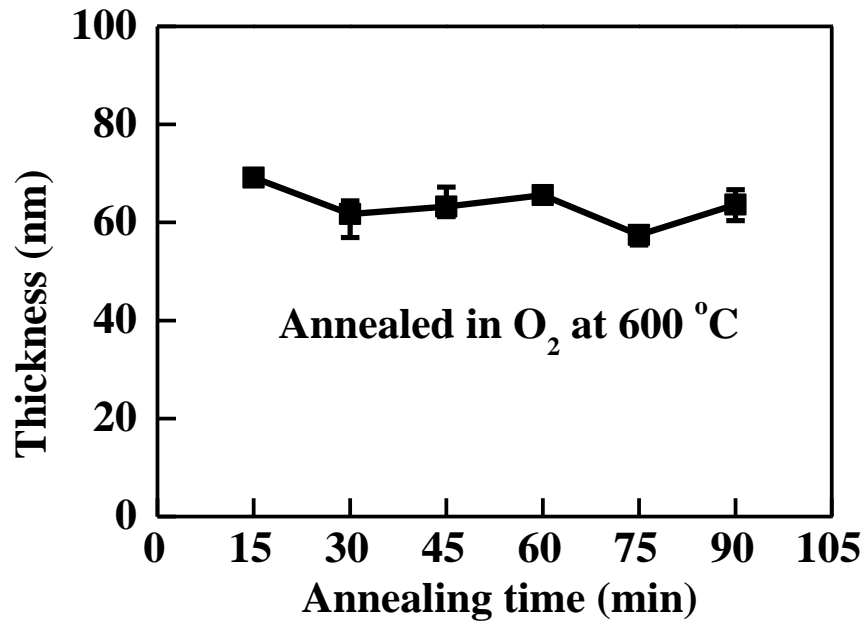


Fig. 2-12: Thickness of In₂O₃ films by varying annealing time.

2.3.2.2 ITO films

As stated above, ITO films were prepared using In(acac)₃ and SnCl₂ in PrA, and also by using In(acac)₃ and Sn(acac)₂ in PrA. From Fig. 2-7, it is found that high mobility is obtained at 600 °C, 1 h annealing in RTA in O₂ environment, for In₂O₃ case. So ITO films were annealed at this condition. ITO films were prepared by varying the SnO₂ wt.% from 1 to 10. Hall mobility decreases as Sn wt.% increases. This is because Sn acts as a donor impurity in In₂O₃ cubic bixbyite crystal structure, so as the tin content increases, more impurity scattering takes place, hence less mobility. As Sn⁴⁺ acts as donor impurity, which donates electron to In₂O₃ by substituting In³⁺, so adding Sn carrier concentration increases. Hall mobility and carrier concentration of ITO films are shown in Fig. 2-13.

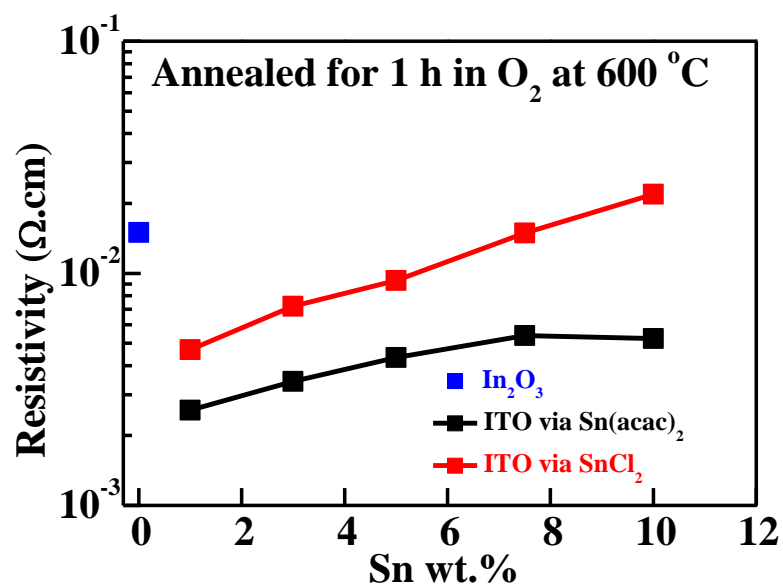
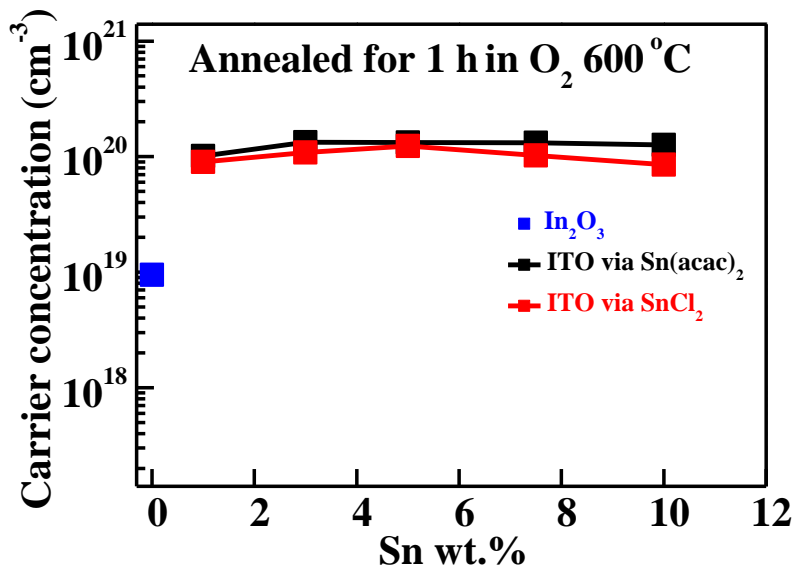
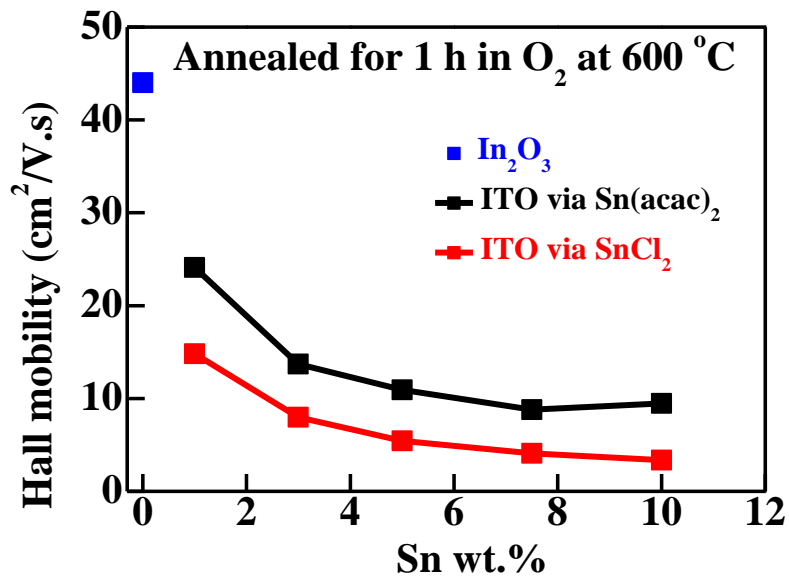


Fig. 2-13: Hall mobility, carrier concentration, and resistivity of ITO films.

From Fig. 2-13, it is seen that the Hall mobility of ITO via SnCl₂ is lower than that of ITO via Sn(acac)₂. This may be due to the reason that ITO via SnCl₂ has Cl incorporated into the films. Therefore, this is one disadvantage of using Cl based precursor. Another disadvantage of using Cl precursors is that chloride compounds can leave toxic by-products behind [20].

The resistivity of the films is calculated by the formula:

$$\rho = \frac{1}{q.n.\mu} \quad (1)$$

where, ρ , q , n , and μ are resistivity, electronic charge (1.6×10^{-19} C), carrier concentration, and mobility, respectively. Since in Eq. (1), q is constant and from Fig. 2-13, carrier concentration is almost same for ITO via SnCl₂ and ITO via Sn(acac)₂. Therefore, it can be concluded that resistivity depends only on Hall mobility.

From Fig. 2-7, it is seen that mobility of In₂O₃ for 1 h annealing at 600 °C in O₂ is as high as 42.6 cm²/Vs, while Fig. 2-13 shows that the resistivity for 1 wt.% ITO annealed in O₂ for 1 h at 600 °C is as low as 2.6×10^{-3} Ωcm. These values are comparable to the values of Hall mobility of In₂O₃ and resistivity of ITO obtained by other research group by vacuum processed (like thermal evaporation, pulsed laser deposition, and sputtering, etc.) In₂O₃ and ITO films. Some of these values are given in Table I and II.

Table I: Comparison of Hall mobility of our solution processed I.O films with other vacuum processed films.

Technique	Hall mobility (cm ² /Vs)	Deposition/ annealing temperature (°C)	Ref.
PLD	35	25	21
PLD	42	25	22
Thermal evaporation	12	100	23
Thermal evaporation	61	150	24
Thermal evaporation	70	350	25
Sputtering	72	400	26
Present work	43	600	--

Table II: Comparison of resistivity of our solution processed ITO films with other vacuum processed films.

Technique	Resistivity (Ωcm)	Deposition/ annealing temperature (°C)	Ref.
PLD	2.8 x 10 ⁻⁴	25	27
Sputtering	1.59 x 10 ⁻⁴	200	28
Sputtering	8.4 x 10 ⁻⁵	300	29
PLD	4.4 x 10 ⁻⁵	300	30
e-beam evaporation	6.0 x 10 ⁻⁵	370	31
Sputtering	1.6 x 10 ⁻⁴	480	32
Present work	2.6 x 10⁻³	600	--

Fig. 2-14 shows the XRD of ITO films, which shows that as Sn content increases, crystallinity decreases. This is also further confirmed by AFM results, which shows that average surface roughness decreases with an increase of Sn content, which means the grain size decreases. Surface roughness as a function of Sn wt.% is shown in Fig. 2-15.

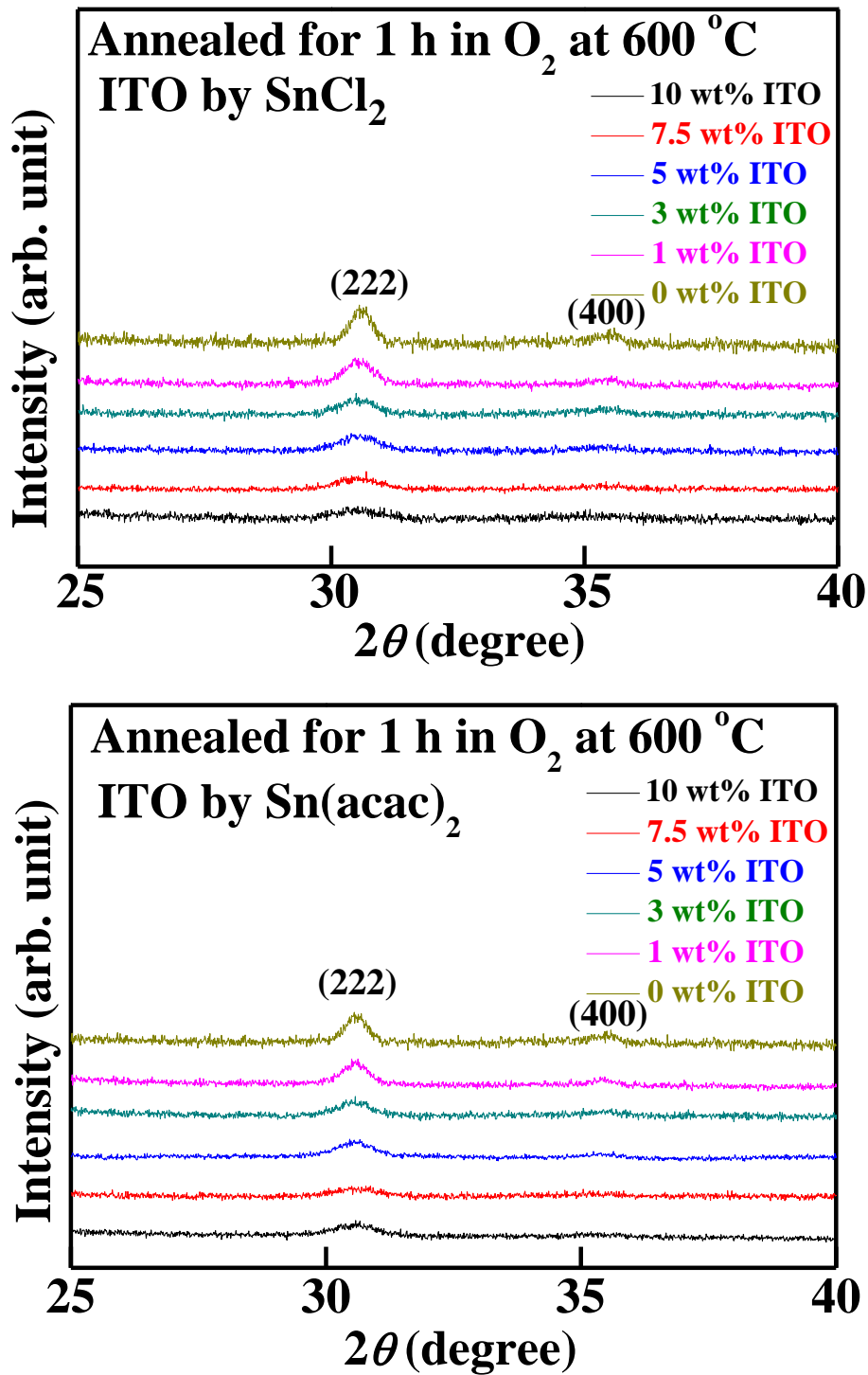


Fig. 2-14: XRD of ITO films for varying Sn wt.%.

The thickness of ITO films as a function of tin weight percent is shown in Fig. 2-16. The film thickness is independent of tin content.

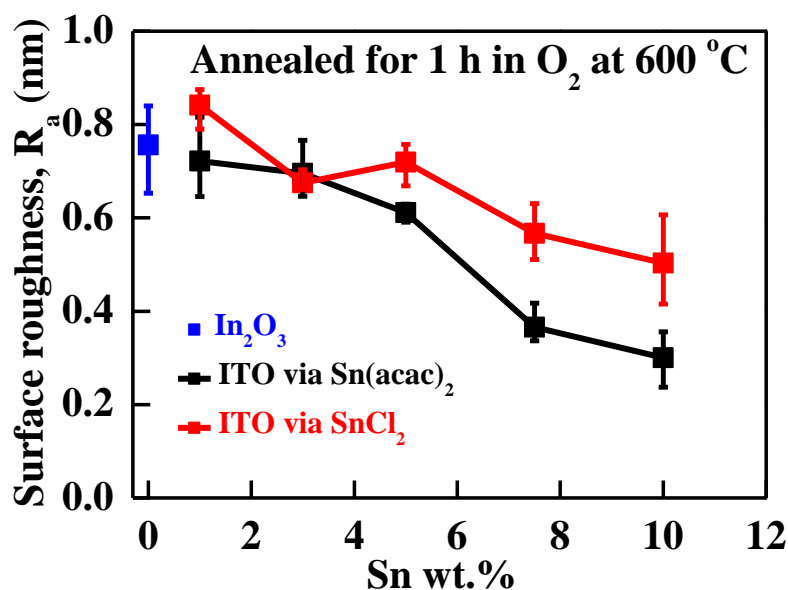


Fig. 2-15: Surface roughness dependence on Sn wt.% of ITO films.

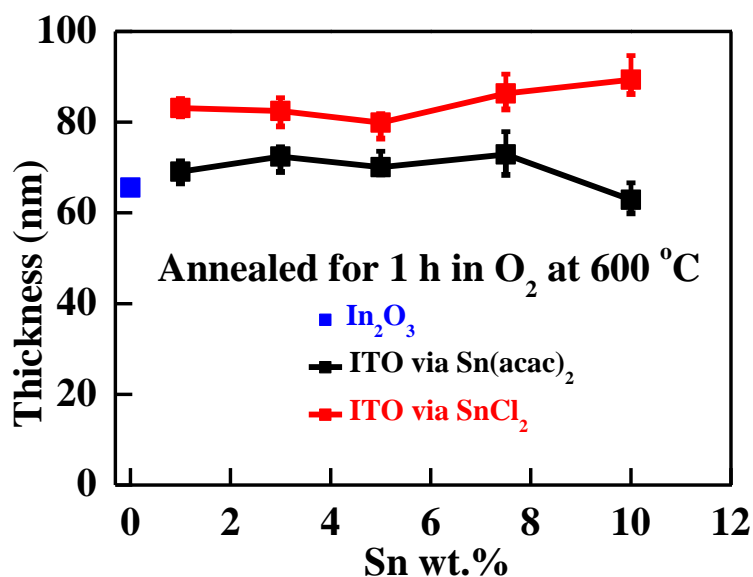


Fig. 2-16: Thickness dependence on Sn wt.% for ITO films.

2.3.3 Annealing temperature dependence

Although the gel films become oxide films at around 350 °C according to TG-DTA analysis, it does not mean that there is complete removal of the organic species from the films at this temperature. As the annealing temperature increases, organic species keep getting removed. The effect of annealing temperature on the electrical properties of In₂O₃ and ITO thin films prepared by solution process is shown in Fig. 2-17.

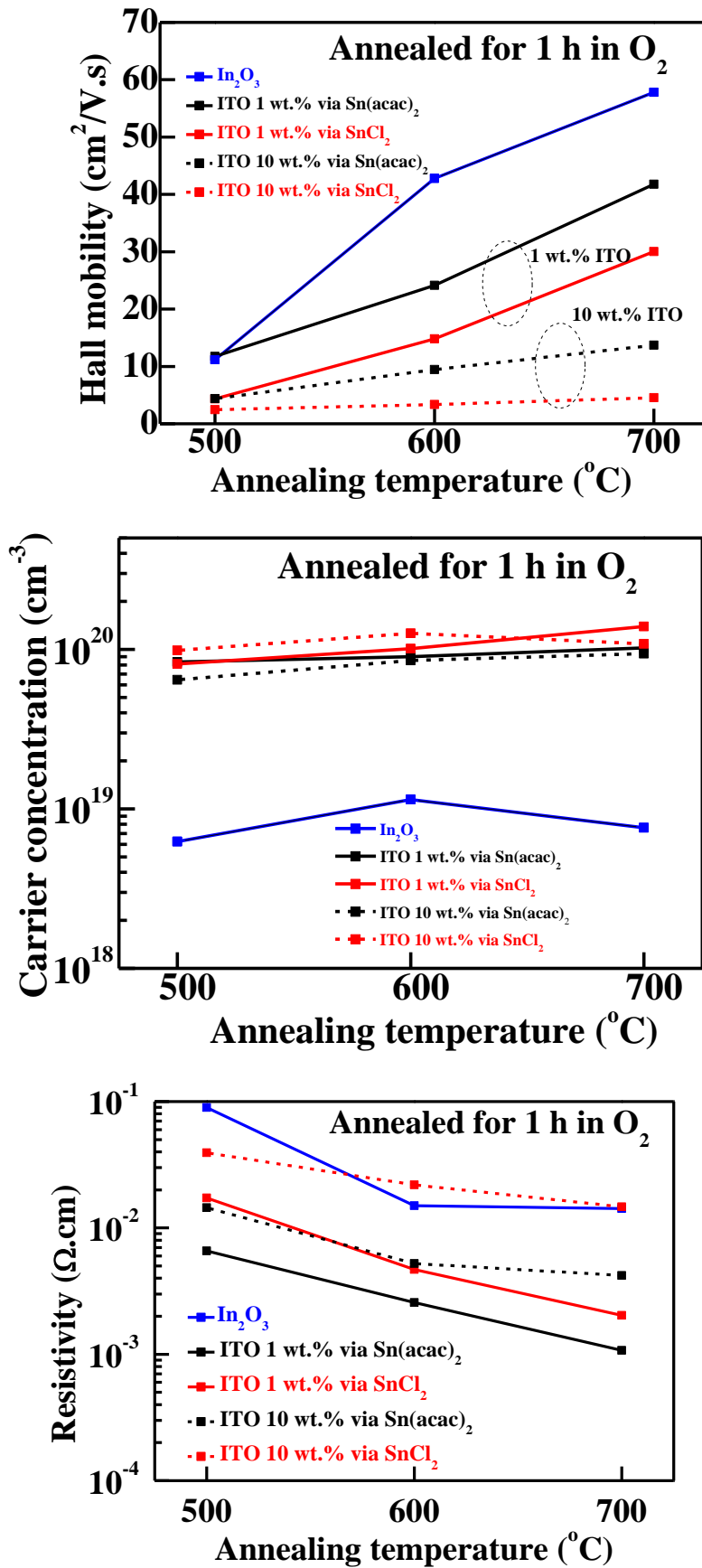
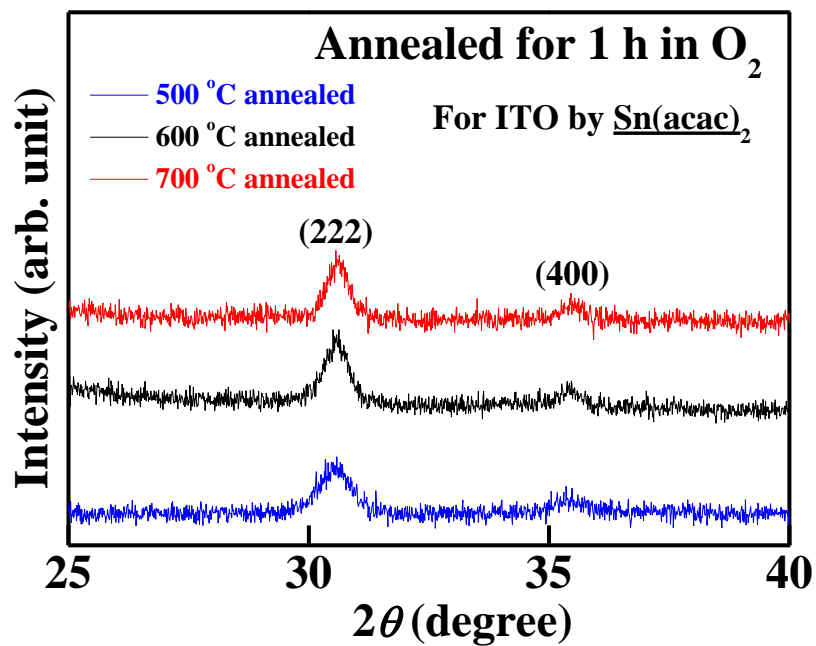
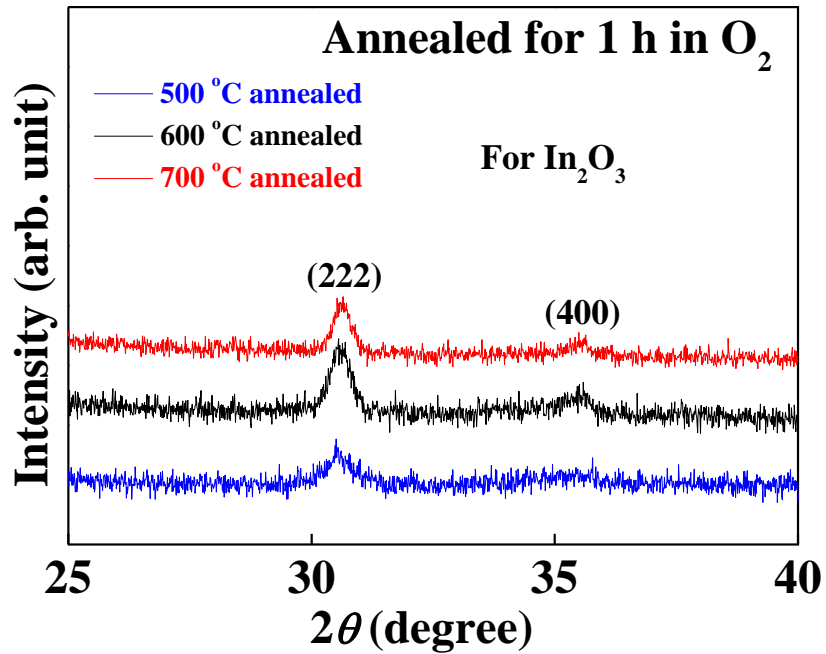


Fig. 2-17: Electrical properties of In₂O₃ and ITO films by varying annealing temperature.

The low resistivity in this case is $1.1 \times 10^{-3} \Omega\text{cm}$ for 1 wt.% ITO via $\text{Sn}(\text{acac})_2$ at 700°C . Again, the resistivity is dependent on mobility because carrier concentration is almost the same for all the samples.

XRD of In_2O_3 and ITO with respect to annealing temperature is shown in Fig. 2-18 which shows that, as annealing temperature increases, crystallinity improves (FWHM reduces).



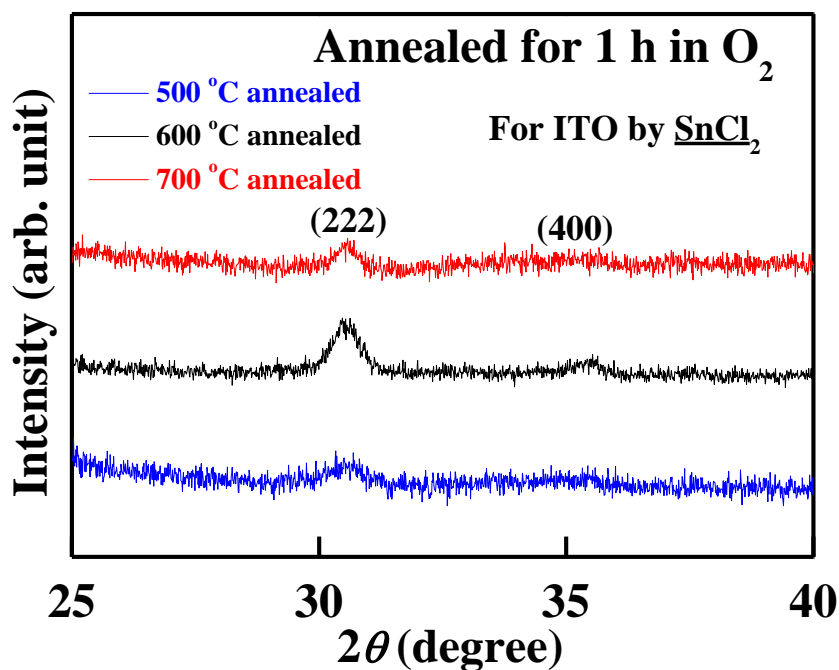


Fig. 2-18: XRD of In₂O₃ and ITO films by varying annealing temperature.

The film thickness dependence on the annealing temperature is shown in Fig. 2-19. As the annealing temperature increases, the thickness either remains constant or decrease. This is because of the reason that with increasing annealing temperature, organic species are removed from the films.

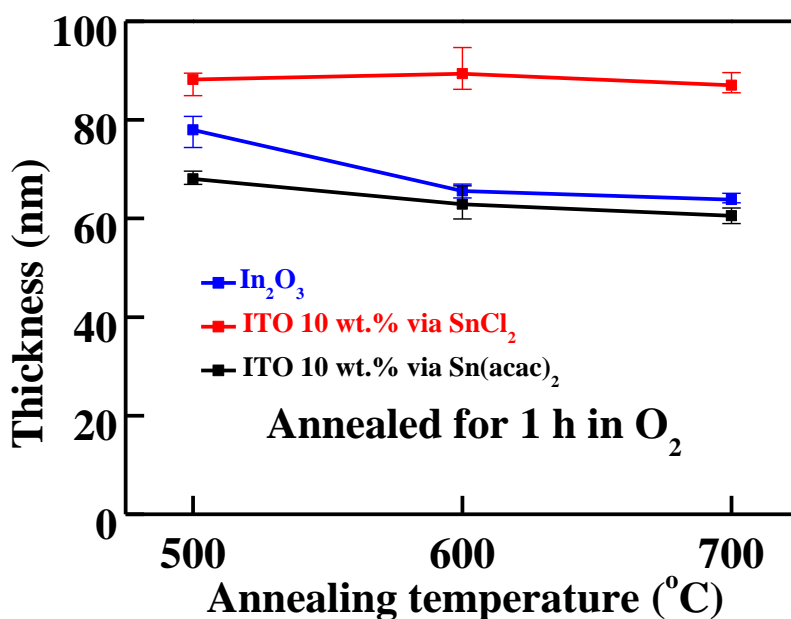
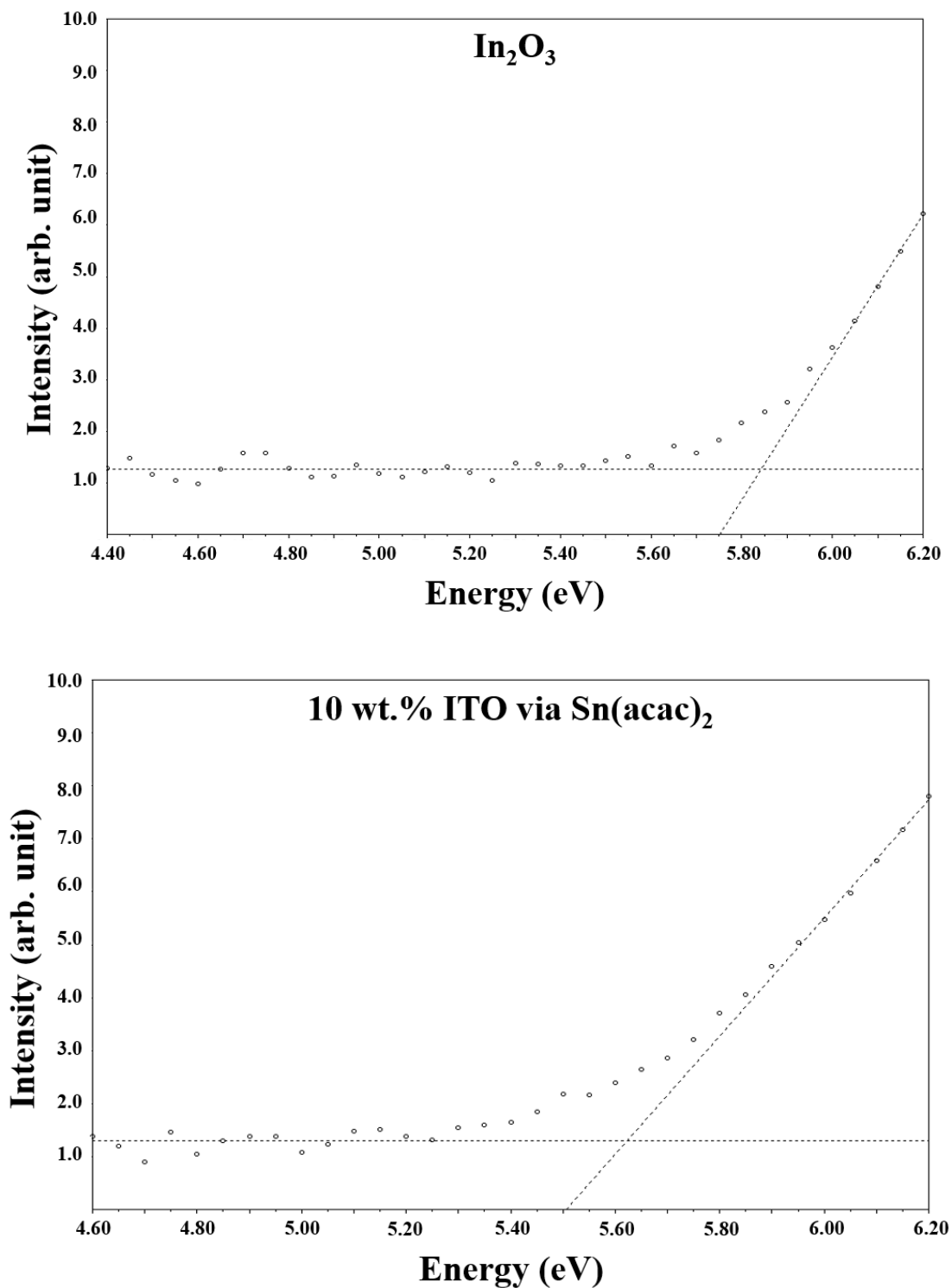


Fig. 2-19: Thickness of In₂O₃ and ITO films by varying annealing temperature.

2.3.4 Work function measurements

The work functions were measured using photoelectron spectrometer for In_2O_3 , 10 wt.% ITO via SnCl_2 , and 10 wt% ITO via $\text{Sn}(\text{acac})_2$. The work functions measurements for In_2O_3 and ITO are shown in Fig. 2-20, while the summary of the work functions are given in Table III.



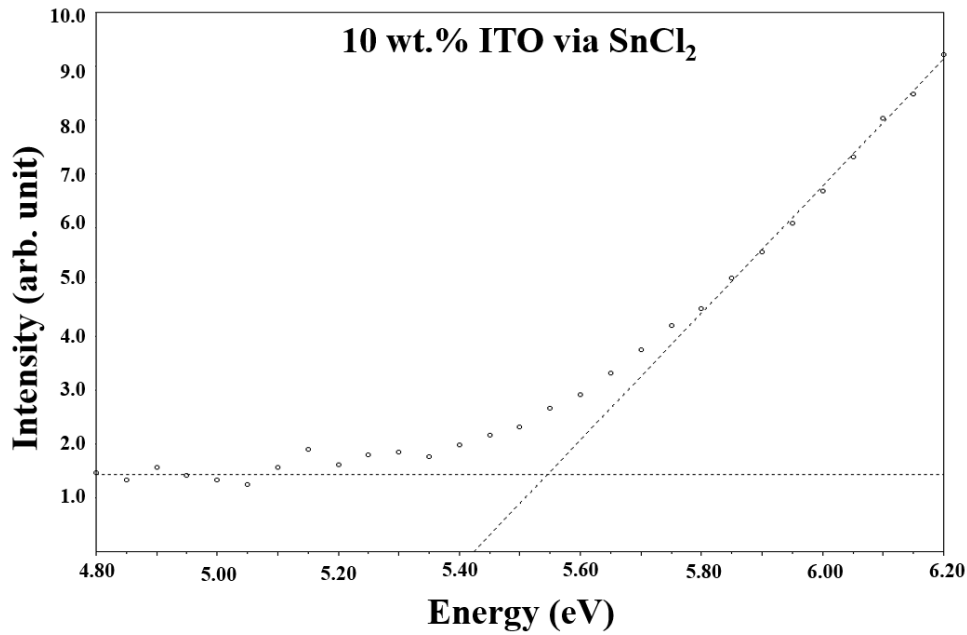


Fig. 2-20: Work function measurements of In_2O_3 and ITO films.

Table III. Work function of In_2O_3 and ITO.

Sample Name	Work function (eV)
In_2O_3	5.8
10 wt.% ITO via $\text{Sn}(\text{acac})_2$	5.6
10 wt.% ITO via SnCl_2	5.6

The work function of In_2O_3 is larger than that of ITO probably because the carrier concentration in In_2O_3 is lower than that of ITO (Fig. 2-13), which means the Fermi level is more towards valance band maximum in In_2O_3 case than in ITO case. As work function is defined as the energy difference between the vacuum level and Fermi level, so work function is more in In_2O_3 than in ITO case.

Summary

In_2O_3 and ITO films were prepared by solution process using $\text{In}(\text{acac})_3$ precursor. High mobility obtained for In_2O_3 case using $\text{In}(\text{acac})_3$ precursor was $42.8 \text{ cm}^2/\text{Vs}$ with a carrier concentration of $9.47 \times 10^{18} \text{ cm}^{-3}$, when In_2O_3 film was annealed for 1 h in O_2 at $600 \text{ }^\circ\text{C}$. Mobility of as high as $57.8 \text{ cm}^2/\text{Vs}$ with a carrier concentration of $7.64 \times 10^{18} \text{ cm}^{-3}$ was obtained for In_2O_3 when annealing temperature was $700 \text{ }^\circ\text{C}$. ITO was prepared using two precursors for tin. One source solution was prepared using $\text{In}(\text{acac})_3$ and SnCl_2 in PrA (named as ITO via SnCl_2), while the another was prepared using $\text{In}(\text{acac})_3$ and $\text{Sn}(\text{acac})_2$ in PrA (named as ITO via $\text{Sn}(\text{acac})_2$). ITO concentration was varied from 1 to 10 wt.%. It was found that as the Sn concentration increases, mobility decreases due to the reason that Sn acts as impurity in In_2O_3 cubic bixbyite structure. Therefore, more the Sn content, more impurity scattering, hence less mobility. The resistivity as low as $2.6 \times 10^{-3} \text{ } \Omega\text{cm}$ for our ITO films was obtained for 1 wt.% ITO via $\text{Sn}(\text{acac})_2$ with a mobility of $24 \text{ cm}^2/\text{Vs}$ and carrier concentration of $1.0 \times 10^{20} \text{ cm}^{-3}$, when ITO film was annealed in O_2 for 1 h at $600 \text{ }^\circ\text{C}$.

References

1. N. Yamada, I. Yasui, Y. Shigesato, H. Li, Y. Ujihira, and K. Nomura, *Jpn. J. Appl. Phys.*, **39** (2000) 4158.
2. D. B. Frazer, *Proc. IEEE*, **61** (1973) 1013.
3. J. B. Du Bow, D. E. Burk, *Appl. Phys. Lett.*, **29** (1976) 494.
4. H. J. J. van Boort, R. Groth, *Philips Techn. Rev.*, **29** (1968) 17.
5. S. Yoshida, *Appl. Opt.*, **17** (1987) 145.
6. Y. Shigesato and David C. Paine, *Appl. Phys Lett.*, **62** (1993) 11.
7. H. Tomonaga and T. Morimoto, *Thin Solid Films*, **392** (2001) 243.
8. H. Hosono, N. Kikuchi, N. Udea, and H. Kawazoe, *J. Non-Cryst. Solids*, **198-200** (1996) 165.
9. Y. Shigesato, S. Tataki, T. Haranou, *Appl. Surf. Sci.*, **48/49** (1991) 269.
10. W. Zachariassen, *Norsk Geologisk Tidsskrift*, **9** (1927) 310.
11. S. Z. Karazhanov, P. Ravindran, P. Vajeeston, A Ulyashin, T. G. Finstad, and H. Fjelivag, *Phys. Rev. B*, **76** (2007) 075129.
12. D. B. Buchholz, Q. Ma, D. Alducin, A. Ponce, M. J. Yacaman, R. Khanal, J. E. Medvedeva, and R. P. H. Chang, *Chem. Mater.*, **26** (2014) 5401.
13. C.H. Yi, I. Yasui, and Y. Shigesato, *Jpn. J. Appl. Phys.*, **34** (1995) 600.
14. Y. Shigesato, S. Tataki, and T. Haranoh, *Jpn. J. Appl. Phys.*, **71** (1992) 3356.
15. R. Latz, K. Michael, and M. Scherer, *Jpn. J. Appl. Phys.*, **30** (1991) L149.
16. R. M. Pasquarelli, D. S. Ginley and R. O'Hayre, *Chem. Soc. Rev.* **40** (2011) 5406.
17. Y. Sawada, C. Kobayashi, S. Seki, and H. Funakubo, *Thin Solid Films*, **409** (2002) 46.
18. Y. Sawada, T. Kondo, T. Aoyama, and R. Ozao, *Trans. Mat. Res. Soc. Japan*, **33** [2] (2009) 225.
19. Y. Sawada, *Mater. Sci. Forum*, **437-438** (2003) 23.

20. Sunho Jeong, Youndmin Jeong, and Jooho Moon, *J. Phys. Chem. C.*, **112** (2008) 11082.
21. F. O. Adurodija, H. Izumi, T. Ishihara, H. Yoshioka, H. Matsui, and M. Motoyama, *Appl. Phys. Lett.*, **74** (1999) 3059.
22. F. O. Adurodija, H. Izumi, T. Ishihara, H. Yoshioka, M. Motoyama, and K. Murai, *J. Vac. Sci. Technol. A*, **18** (2000) 814.
23. S. Cho, *J. Korean Phys. Soc.*, **60** (2012) 2058.
24. Z. Ovadyahu, B. Ovrzyn, and H. W. Kraner, *J. Electrochem. Soc.*, **130** (1983) 917.
25. C. A. Pan and T. P. Ma, *Appl. Phys. Lett.*, **37** (1980) 163.
26. M. Mizuhashi, *Thin Solid Films*, **70** (1980) 91.
27. J. P. Zheng and H. S. Kwok, *Thin Solid Films*, **232** (1993) 99.
28. K. Utsumi, O. Matsunaga, and T. Takahata, *Thin Solid Films*, **334** (1998) 30.
29. F. O. Adurodija, H. Izumi, T. Ishihara, H. Yoshioka, and M. Motoyama, *J. Appl. Phys.*, **88** (2000) 4175.
30. I. A. Rauf, *J. Mater. Sci. Lett.*, **12** (1993) 1902.
31. S. Ray, R. Benerjee, N. Basu, A. K. Batabyal, and A. K. Barua, *J. Appl. Phys.*, **54** (1983) 3497.
32. L. A. Ryabova, V. S. Salun, and I. A. Serbinor, *Thin Solid Films*, **92** 327 (1982).

3. Characterization of In₂O₃ and Indium-Tin-Oxide (ITO) Thin Films by Nano-Rheology Printing (n-RP)

3.1 Introduction

Printed electronics have recently gained attention due to their low environmental impact, less number of steps, large area fabrication, ease of patterning on organic and inorganic substrates; and low cost [1-4]. Some of the present printed techniques include inkjet printing, offset printing, microcontact printing and gravure printing, etc., which are used to fabricate organic thin film transistors (TFTs) [5-6], printed circuits [7] sensors [6-8] and displays [9]. Inkjet printing is a popular method, but not appropriate for the miniaturisation of the advanced electronic devices, as the required resolution is sub-micrometres or below [10], which cannot be realised by the inkjet printing. Furthermore, it is hard to realise precise shape control and lack of scalability via inkjet printing [11].

A novel printing method, named, nano-rheological printing (n-RP) has been introduced by Shimoda et al. in JAIST. N-RP is a direct thermal imprinting technique which performs imprinting at an elevated temperature by utilizing the rheological properties of oxide precursor gels [4, 12-15].

3.2 Nano-rheological printing process

The study of rheological properties of a material in a confined geometry is known as nano-rheology, while rheology itself means to deal with deformation and flow of matter [13]. N-RP is based on direct imprint of precursor gel films, using which we can fabricate patterns as small as 100 nm with good shape control. N-RP is a resist-free, direct printing method, which utilises the rheological properties of a metal-oxide precursor gel to form patterns in the

precursor gel. Other advantages of n-RP are the simple equipment with lower complexity production steps and less material wastage. The complete process is described in Fig. 3-1.

- a) First, the source solution (i.e. source solution of the metal-oxide material in which the patterns are to be created) is spin-coated on the substrate and then dried, so that the source solution on the substrate can be changed from a liquid film into oxide precursor gel film as shown in Fig. 3-1(a).
- b) The sample (i.e. substrate with precursor gel) is then inserted into the n-RP machine, aligned properly with respect to the mold (Fig. 3-1(b)).
- c) The mold is then applied directly (without any resist) on the precursor gel, after which appropriate imprinting temperature and pressure are applied (Fig. 3-1(c)).
- d) The oxide precursor gel softens at imprinting temperature, thereby allowing the transfer of patterns from the mold to the gel film. The mold and gel are allowed to be in contact with each other for some time, after which the sample is cooled gradually. The mold is then detached from the patterned gel film (Fig. 3-1(d)), with some residual film on the gel film, corresponding to the convex regions of the mold.
- e) The residual film is removed by dry etching. During this dry etching, there is also slight etching of the thick patterned regions that correspond to the concave patterns of the mold (Fig. 3-1(e)). This kind of structures can be used for TFT application.
- f) Finally, after annealing, the etched patterned gel film oxidises into the solid oxide material (Fig. 3-1(f)). This kind of structure can be used for electrode application.

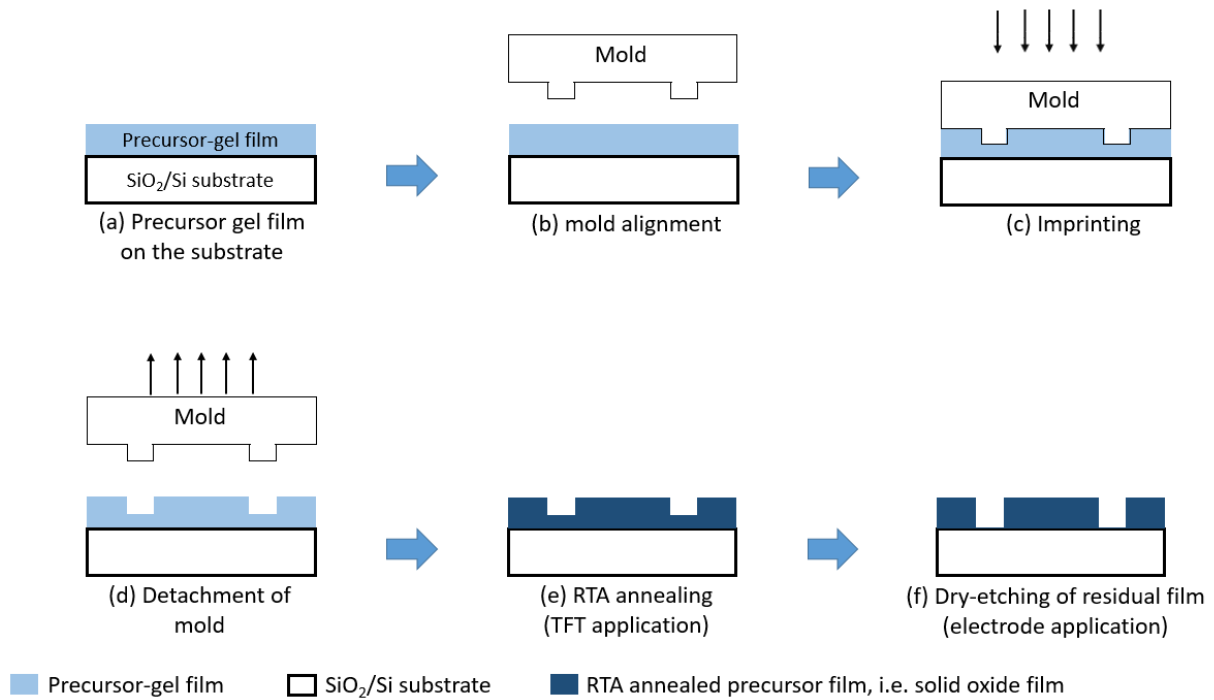


Fig. 3-1: Schematic of n-RP process.

To date, fine pattern formation by n-RP has been reported for In₂O₃ [4], ITO [4], ruthenium lanthanum oxide (Ru-La-O) [16], and ruthenium oxide (RuO) [17]. However, there are few reports on the study of the electrical properties of In₂O₃ and ITO films prepared by n-RP (or sometimes also referred as direct thermal imprinting or direct imprinting in this work). In the present work, we report electrical properties of In₂O₃ and ITO films imprinted by the n-RP process along with the patterning properties. In₂O₃ and ITO are selected because they are very mature materials, which are used as transparent conducting electrode for solar cells, flat panel displays, etc., as well as channel in TFTs [18-20]. The electrical properties of imprinted In₂O₃ and ITO films were also compared with non-imprinted films. In addition, in the previous work on the patterning properties of ITO, the ITO film was prepared using indium acetylacetonate and tin acetylacetonate in propionic acid. In the present work, tin chloride was also used to prepare ITO along with tin acetylacetonate.

3.3 Experimental procedure

To carry out the imprinting, first of all the mold is cleaned with acid to make the surface of mold -OH terminated. This was done using ammonium peroxide mixture (APM), $\text{NH}_4\text{OH}:\text{H}_2\text{O}_2:\text{DI}$ in 1:1:2 ratio. 40 ml of this solution was heated at 80 °C for 20 min, after which the mold was ultra-sonicated in de-ionized (DI) water for 3 min. After making surface of the mold, -OH terminated, the surface of the mold (which goes in direct contact with the precursor-gel film) has to be treated with release and rinse agent (“release + rinse” are known as “coupling agent”). This is to form a self-assembled monolayer (SAM) layer on the surface of the mold. SAM layer is necessary, as this layer is fluorine terminated layer. Fluorine is hydrophobic in nature, so high fluorine content is needed to enhance the release treatment of the gel film from the mold. If the fluorine content is low, then hydrophobicity is reduced and there are more chances that the gel film gets attached with the mold (due to van der Waals interactions) during the detaching of the mold from the film. This may break the patterns. The complete process of SAM layer formation is shown in Fig. 3-2, while the conditions for release and rinse treatment via spin-coating are shown below:

- **Release agent:** spin-coat: 1000rpm/20sec, dry: 120 °C for 20 min.
- **Rinse agent:** ultra-sonicated/3 min, dry: 130 °C for 5 min.

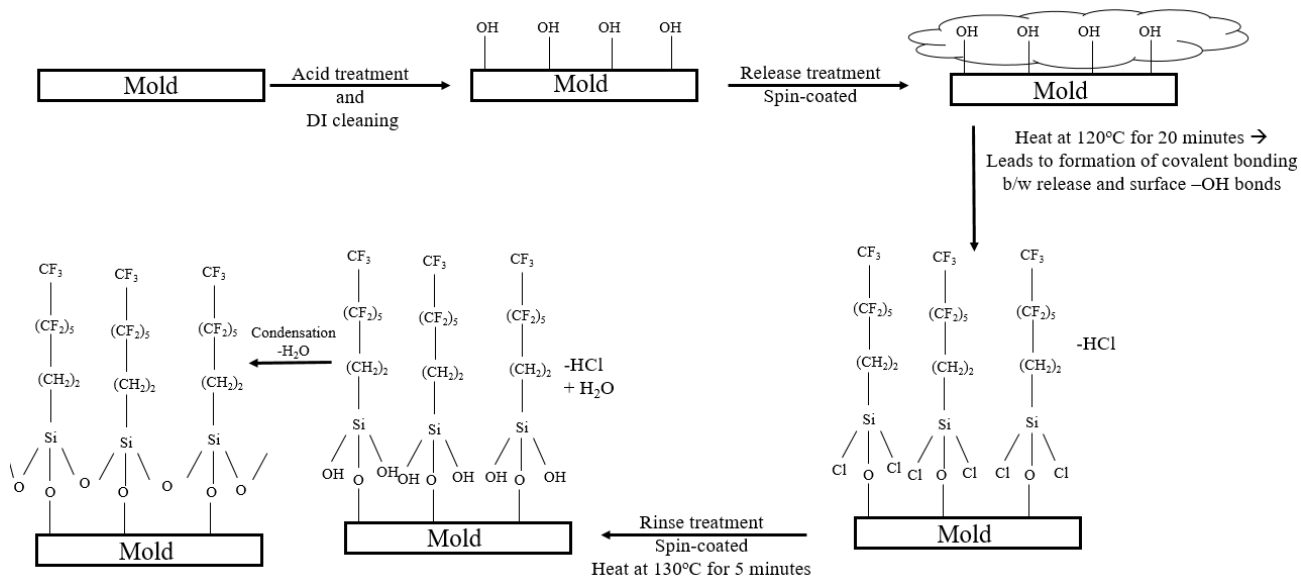


Fig. 3-2: SAM layer formation mechanism on mold.

After preparing the SAM layer on the mold, first, the patterning properties in In_2O_3 by n-RP were investigated to determine good patterns, these conditions were then used as reference conditions to investigate the n-RP properties in ITO films, i.e. to study the effect of the addition of tin (Sn) into In_2O_3 patterning and electrical properties. The In_2O_3 and ITO source solutions and precursor gels were prepared using the conditions as described in Chapter 2. The Sn content of both prepared ITO source solutions was 10 wt.%.

The patterns were checked first by visual inspection and then by using an optical microscope (Olympus BX-51). Further characterisation was performed by secondary ion mass spectroscopy (SIMS; by Material Science and Technology, Promotion Foundation Analysis, Japan), Fourier transform infrared spectroscopy (FT-IR; Perkin Elmer Spectrum 100 FT-IR Spectrometer) in transmittance mode, and X-ray photoelectron spectroscopy (XPS; S-Probe Surface Spectrometer). The crystallinity of the films was measured by an X-ray diffractometer (XRD; X'Pert PRO MRD, PANalytical) using $\text{Cu K}\alpha$ radiation ($\lambda = 1.54 \text{ \AA}$) with 40 kV and 40 mA acceleration voltage and current, respectively. The thermal behaviour (i.e. evaporation of solvent, decomposition of organic species, and oxidation of the precursor gel) of the samples

was studied via thermogravimetry-differential thermal analysis (TG-DTA; by Toshiba Nanoanalysis Corporation). For mass spectroscopy and viscoelastic property studies, Fourier transform ion cyclotron resonance mass spectrometer (FT-ICR-MS; Solarix-JA, Bruker Daltonics) and Rheogel E-4000 (UBM Corporation) were used, respectively. For electrical properties measurement, a Hall effect measurement system (TOYO Corporation Resitest 8400) was utilised at room temperature using the van der Pauw method. The annealing was done using rapid thermal annealing (RTA; Ulvac Sinku-Riko Infrared Furnace) system.

A “quartz SNP-02” mold ($10 \times 10 \times 0.625 \text{ mm}^3$) purchased from NTT-Advanced Technology was used to study the patterning properties. SNP-02 is a checker mold with square concave patterns with an area of $100 \mu\text{m}^2$ (each pattern) and depth of 500 nm. Furthermore, each square is separated from another square by a $10\text{-}\mu\text{m}$ -wide convex line. A schematic of the SNP-02 quartz mold is shown in Fig. 3-3.

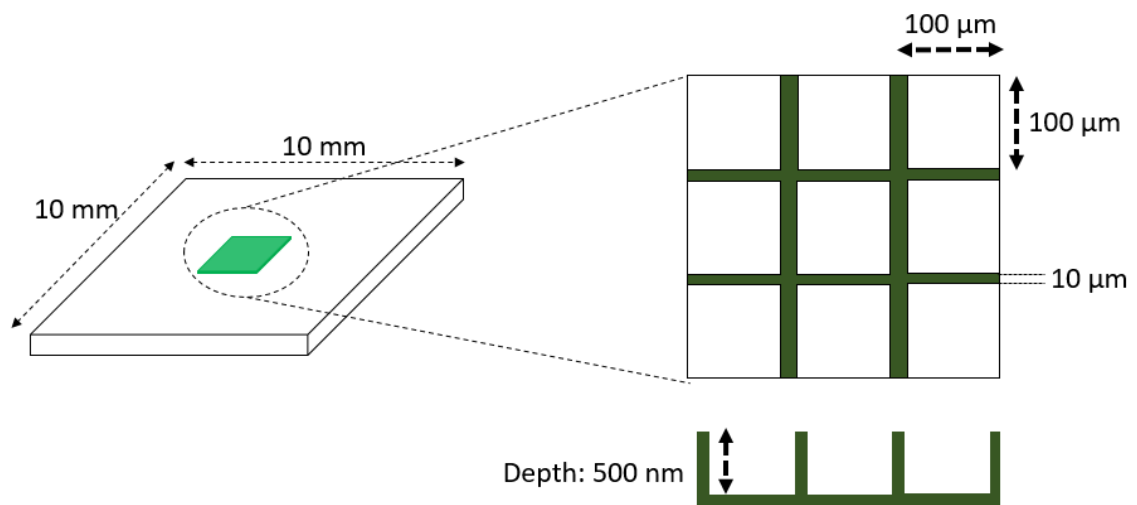


Fig. 3-3: Schematic of SNP-02 mold.

A “flat” mold, which was an eagle XG glass purchased from Corning, with an area of $10 \times 10 \text{ mm}^2$ and 1.1 mm thick, was used to study the electrical properties because a large imprinted area is necessary for Hall measurements.

The n-RP machine used in this work is shown in Fig. 3-4, while Fig. 3-5 shows the n-RP machine during imprinting.

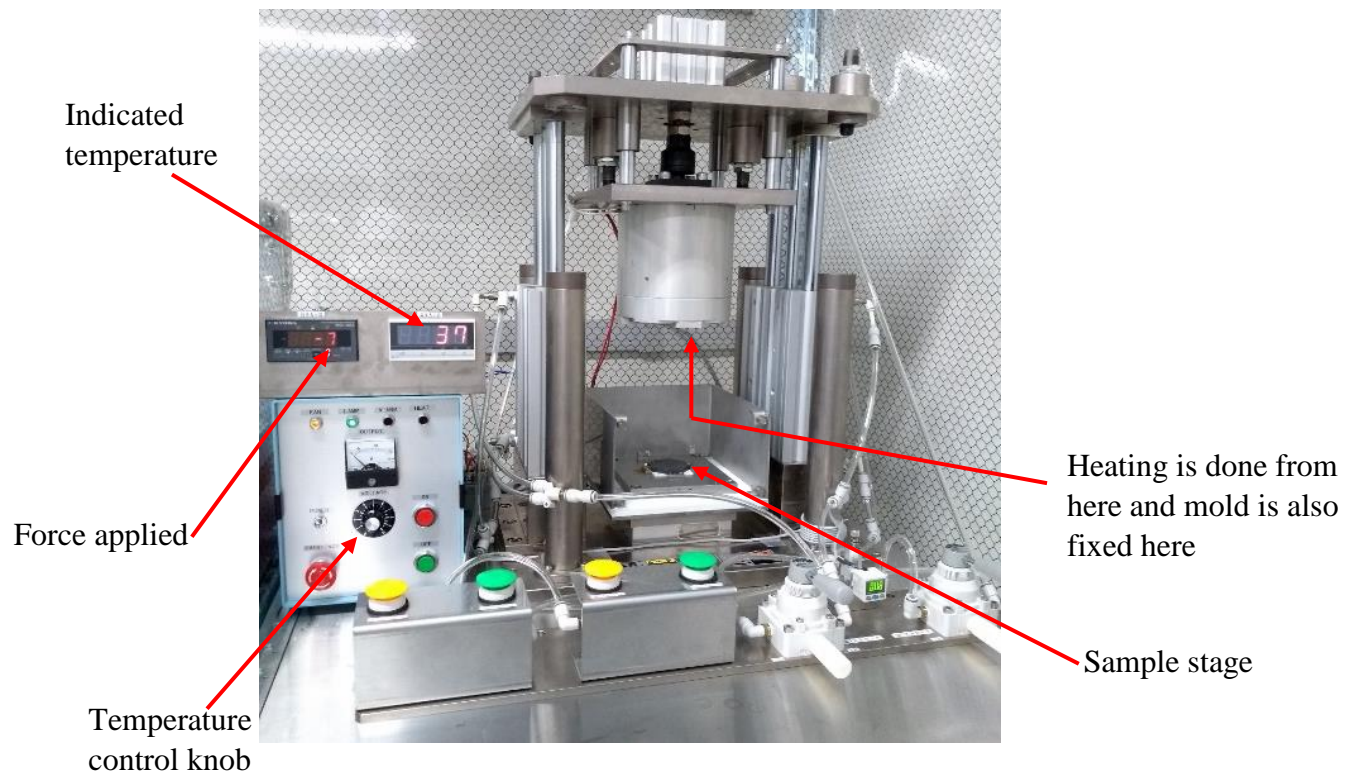


Fig. 3-4: n-RP machine with various parts explained.



Fig. 3-5: n-RP machine during imprinting.

3.4 Results and discussion

3.4.1 Actual v/s indicated temperature

The temperature of the imprinting machine stage where we put our sample for imprinting is known as sample stage (shown in Fig. 3-4). Machine LED shows this temperature, which we call as indicated temperature (also shown in Fig. 3-4). However, when we measured the actual temperature of the sample stage using thermocouple, we found some difference from the indicated one. The temperature of the sample stage measured using thermocouple, we call that as actual temperature. The relation between the actual v/s the indicated temperature is shown in Fig. 3-6, which shows that the actual temperature is higher than the indicated temperature. Throughout this thesis, we have used actual temperature, unless otherwise stated.

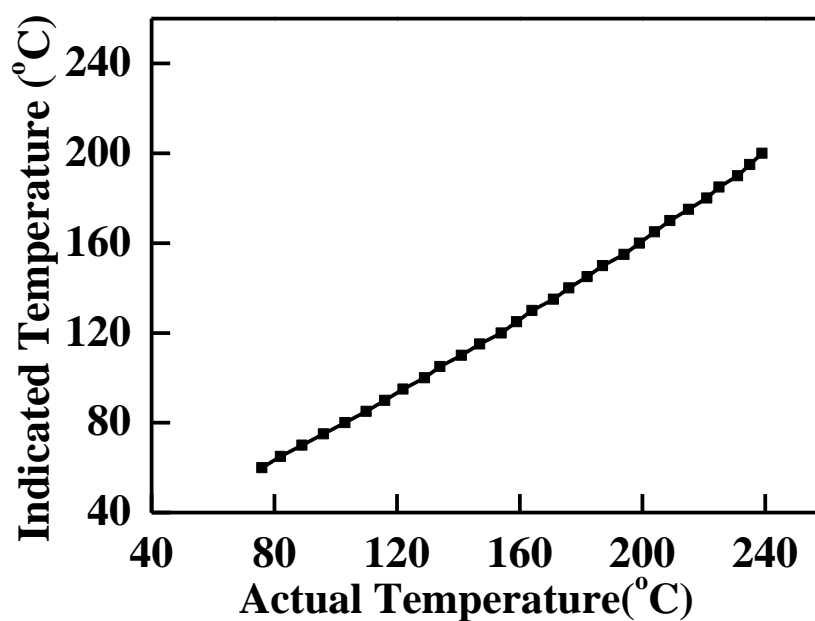


Fig. 3-6: Actual temperature v/s indicated temperature.

3.4.2 Patterns formation

3.4.2.1 With temperature dependence

To optimize the temperature at which we get good patterns in In_2O_3 films, first we put In_2O_3 sample on the imprinting stage and then increased the imprinting temperature. The imprinting

temperature was varied from 155, 165, 175, 185, 200, and 210 °C (actual temperature). These correspond to the indicated temperature of 110, 120, 130, 140, 150, 160, and 170 °C, respectively. The pressure applied was 15 MPa. The mold and gel film remain in contact for 5 min (imprinting time) and then cooling started at the cooling rate of 5.8 °C min⁻¹. The results are shown in Fig. 3-7. The result shows that 175 °C (actual temperature) gives better imprinting patterns. The mold used was SNP-02 checker mold. This mold will be used later for TFT formation, as well. The details of this mold is given in the experimental section. From the above results, 175 °C was selected as the best imprinting temperature for In₂O₃.

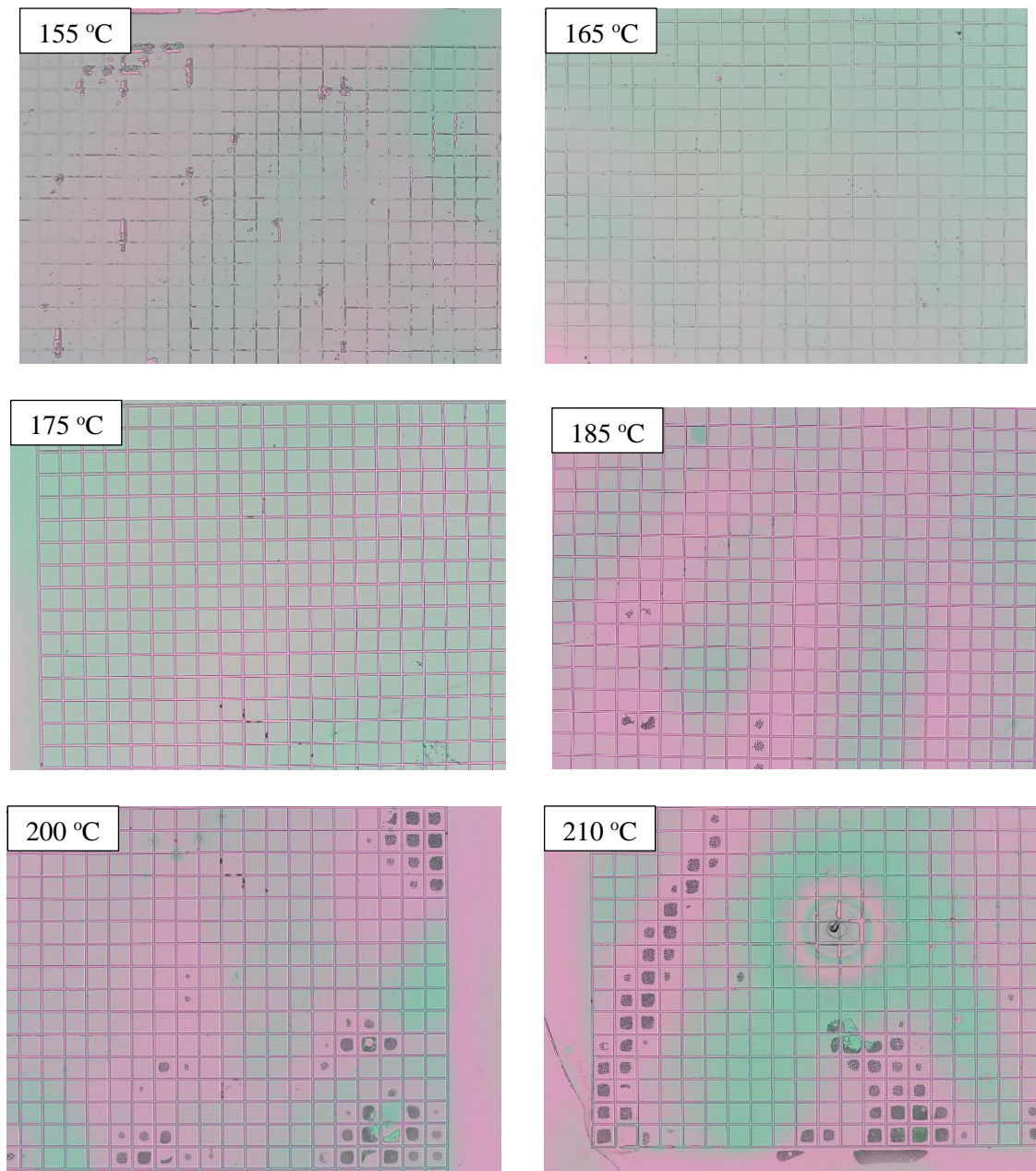


Fig. 3-7: Imprinting of In_2O_3 gel film using SNP-02 quartz mold by varying imprinting temperature.

3.4.2.2 With pressure dependence

The above experiments were performed using 15 MPa of imprinting pressure. We also performed imprinting of In_2O_3 using 175 °C as imprinting temperature but using 5 and 10 MPa of imprinting pressure as well, keeping imprinting time and cooling rate same as stated in Sec. 3.4.2.1 The results are shown in Fig. 3-8 which shows that imprinting is independent of the applied pressure.

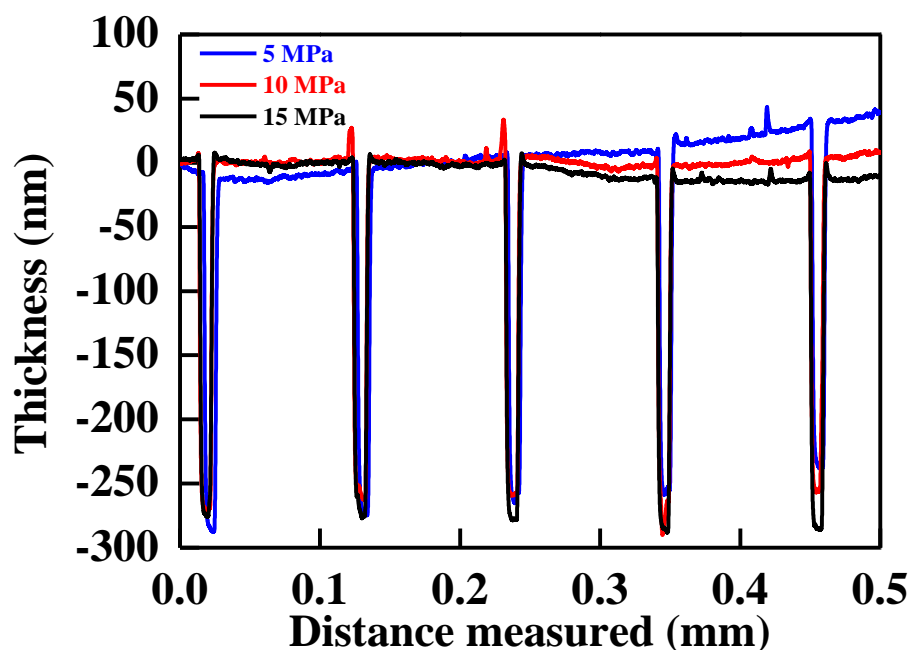


Fig. 3-8: Thickness of imprinted In_2O_3 film using SNP-02 mold by varying imprinting pressure.

3.4.3 Patterns of In_2O_3 and ITO

The patterns of In_2O_3 , 10 wt.% ITO via $\text{Sn}(\text{acac})_2$, and 10 wt.% ITO via SnCl_2 (done at the same conditions as of In_2O_3 , i.e. 175 °C and 15 MPa) using the SNP-02 mold (as described in experimental procedure) are shown in Fig. 3-9. It was evident that the patterns of In_2O_3 were better than that of ITO and that they degraded with the addition of Sn.

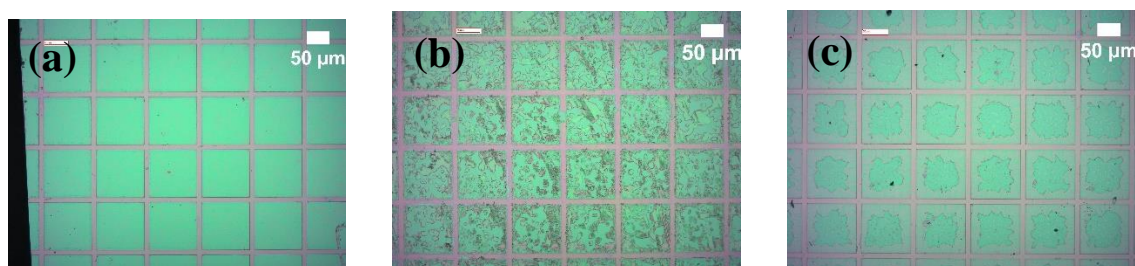
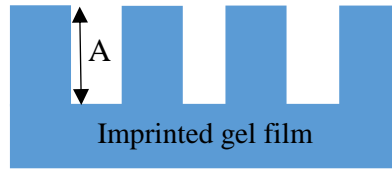
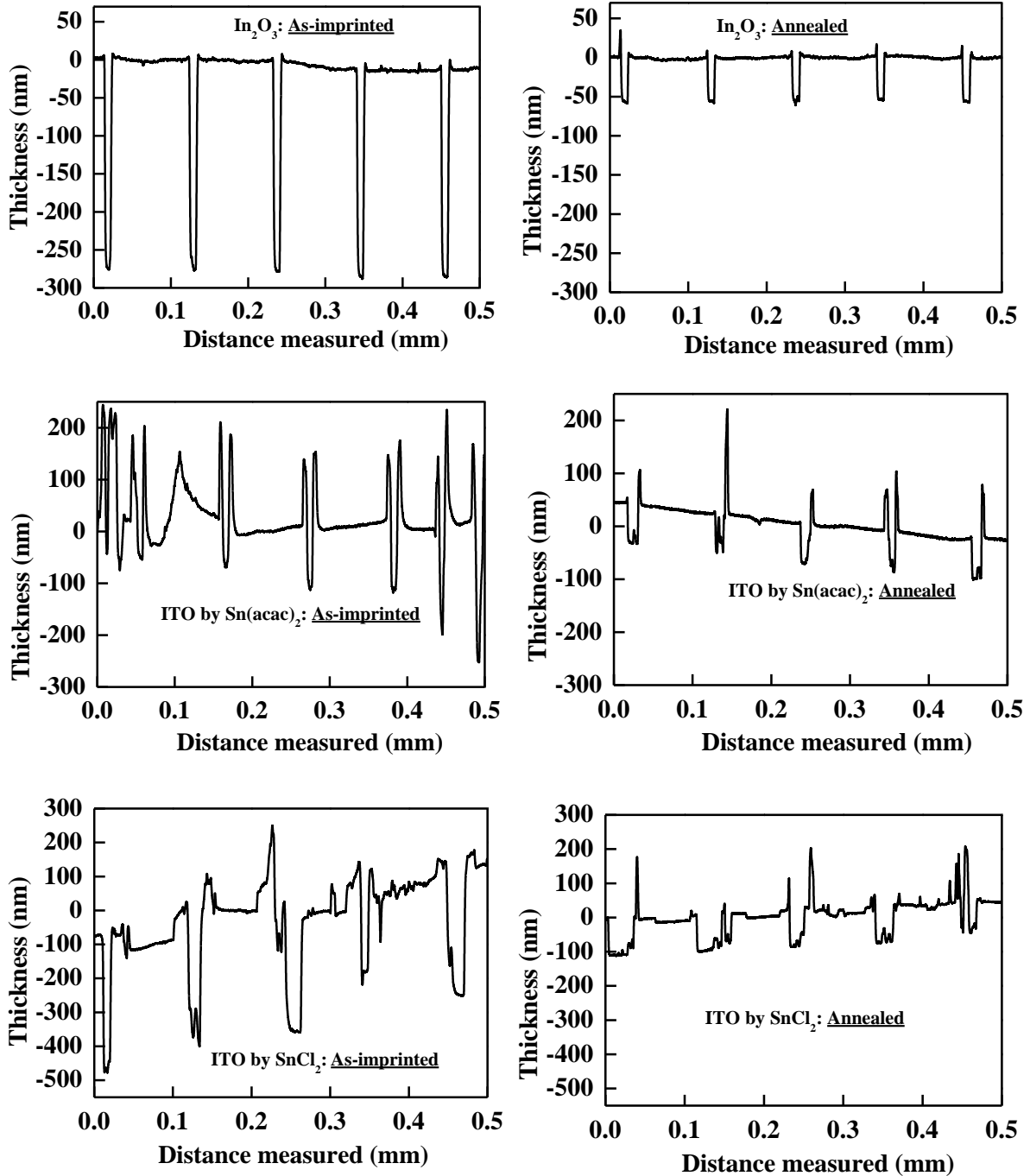


Fig. 3-9: Optical microscope images of n-RPed (a) In_2O_3 , (b) ITO via $\text{Sn}(\text{acac})_2$, and (c) ITO via SnCl_2 .

The thickness of In_2O_3 , ITO via $\text{Sn}(\text{acac})_2$, and ITO via SnCl_2 for Fig. 3-9 is shown in Fig. 3-10. Thickness of region labelled as “A” in Fig. 3-10 (a) is shown in Fig. 3-10 (b).



(a): Region A for which thickness is measured and shown in Fig. 3-10 (b).



(b): Thickness of In_2O_3 and ITO measured by alphastep profilometer.

Fig. 3-10: Thickness of In_2O_3 , ITO via $\text{Sn}(\text{acac})_2$, and ITO via SnCl_2 before and after annealing, with imprinting temperature, pressure, time, of 175 °C, 15 MPa, and 5 min.

Figures 3-11 and 3-12 show the TG and DTA of the source solutions, respectively. TG-DTA measurements were performed in air at a constant heating rate of $10\text{ }^{\circ}\text{C min}^{-1}$. It can be seen from the TG-DTA curves that the evaporation of the solvent in In_2O_3 and ITO is completed at around $120\text{ }^{\circ}\text{C}$. Around this temperature, semi-solid substances (i.e. oxide precursor gels) are generated, whereas an exothermic reaction starts at $250\text{ }^{\circ}\text{C}$, ending around $350\text{ }^{\circ}\text{C}$. The exothermic peak indicates the solidification of each oxide precursor gel due to oxidation. From TG-DTA analysis, it was evident that the gel state of In_2O_3 and ITO is in the temperature range between $120\text{ }^{\circ}\text{C}$ to $290\text{ }^{\circ}\text{C}$, so imprinting is performed in this temperature range, as the specimen is in a semi-solid state in this temperature range.

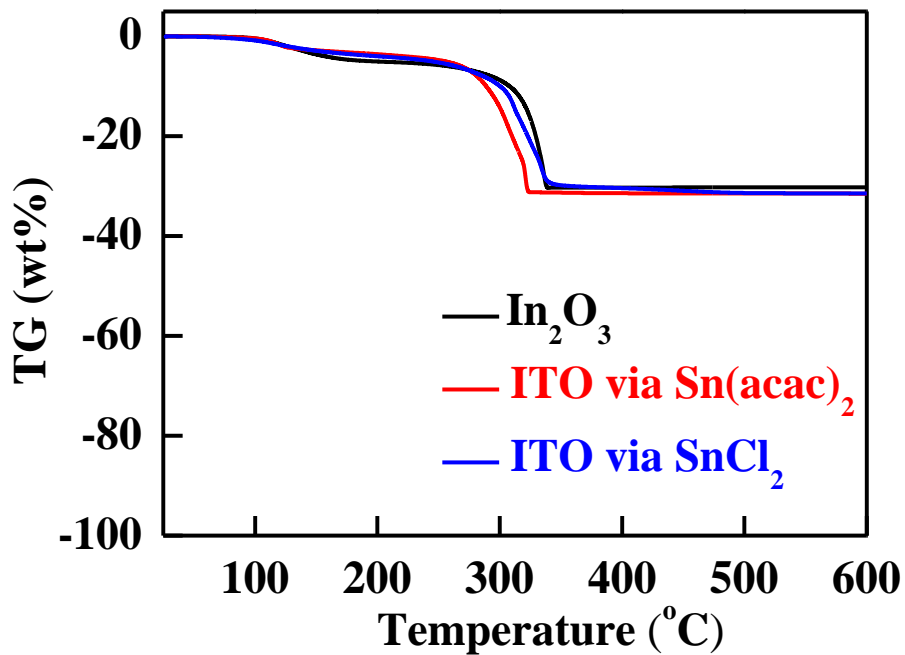


Fig. 3-11: Thermogravimetric (TG) analysis of In_2O_3 and ITO source solutions.

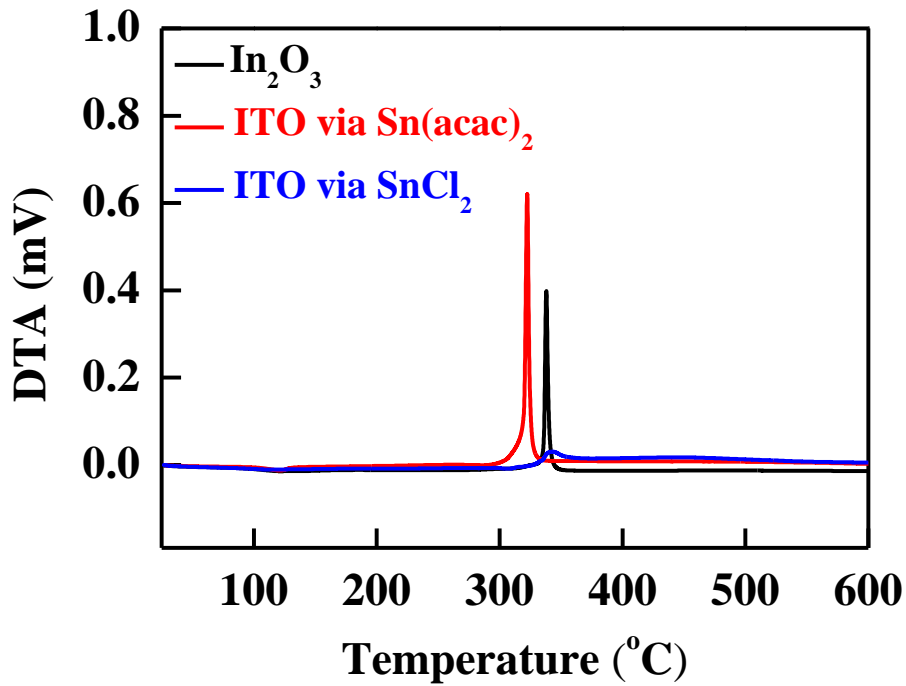


Fig. 3-12: Differential thermal analysis (DTA) of In_2O_3 and ITO source solutions.

3.4.4 Electrical properties

Before going further, it is necessary to explain two terms, imprinted and non-imprinted film. After the gel film was prepared on SiO_2/Si substrate, the sample (i.e. substrate having precursor-gel film) was inserted into the imprinting machine and imprinting was performed on a small region of the sample (i.e. pressure was applied on a small region of the gel, while the complete sample experienced the same imprinting temperature). After imprinting, the sample was taken out from the machine and cut into two parts. The pressure applied part is called the “imprinted film”, while the non-pressure applied part is known as the “non-imprinted film”. Figure 3-13 shows the imprinted and non-imprinted films, schematically. For the electrical properties, the Hall mobility and carrier concentration of “imprinted In_2O_3 and ITO films” were compared with “non-imprinted In_2O_3 and ITO films”. Figure 3-14 shows the Hall mobility and carrier concentration of imprinted and non-imprinted In_2O_3 and ITO annealed at 600 °C in O_2 environment for 1 hour. The Hall mobilities of the 600 °C annealed films reduced by the direct imprinting process which was performed at 175 °C. For In_2O_3 , the mobility reduction by the

imprinting process is more serious than ITO. The carrier concentration of non-imprinted and imprinted In_2O_3 films were $4.2 \times 10^{18} \text{ cm}^{-3}$ and $2.8 \times 10^{19} \text{ cm}^{-3}$, respectively, suggesting that the imprinted In_2O_3 film contains more oxygen vacancies, whereas the carrier concentration of the ITO films were almost the same, regardless of the Sn precursor.

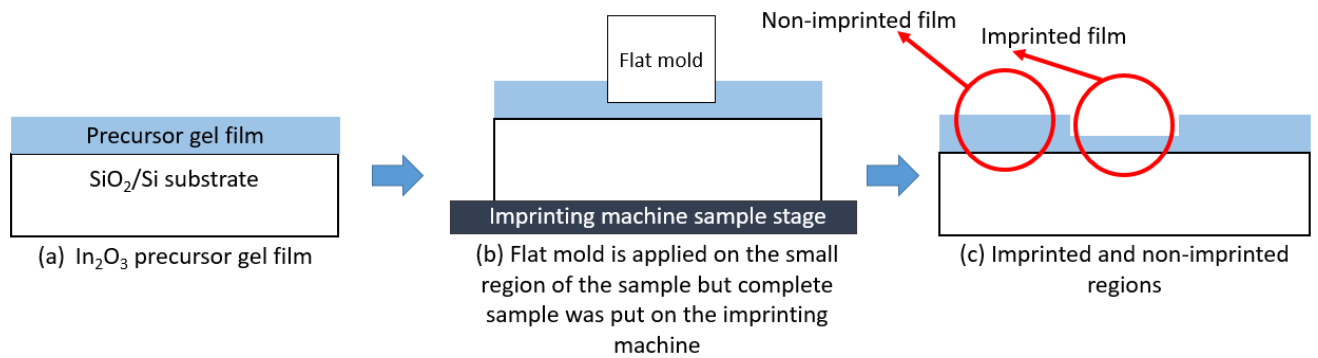


Fig. 3-13: Description of imprinted and non-imprinted films.

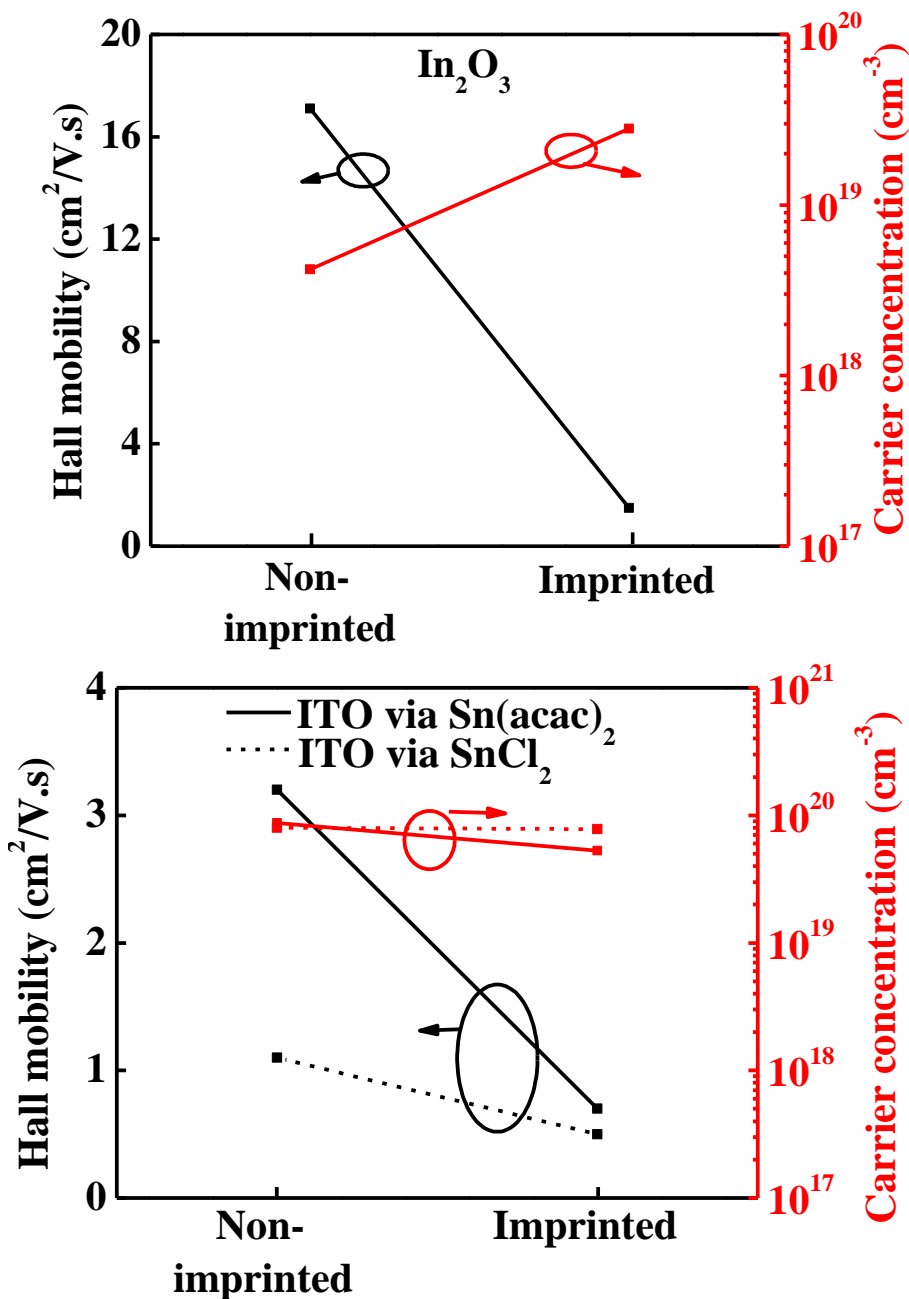


Fig. 3-14: Hall mobility of imprinted and non-imprinted films after annealing at 600 °C.

3.5 Discussion

The organic species in the gel films were analysed by FT-IR as shown in Fig. 3-15, where most peaks were due to carbon related compounds. In FT-IR, the broad band at around 3440 cm⁻¹ and peak at around 2970 cm⁻¹ are due to the stretching vibration of O-H and C-H bonds, respectively [21]. Around 1560 cm⁻¹, the peak, labelled by (a) in Fig. 3-15, is due to the acetylacetonato band in the In complex [21], while some authors refer to it as COO⁻ asymmetric

stretching [22]. The peaks at around 1470, 1430, and 1380 cm^{-1} are due to C-H bending, peaks at around 1250, 1140, and 1080 cm^{-1} are due to C-H stretching bond [23]. The peaks at around 1015 cm^{-1} (labelled as (b) in the figure) are due to acetylacetonato band in the In complex [22], which some authors reported as C=O bond [23], and peaks at 888 and 814 cm^{-1} are due to C-H bending [21, 26]. The peaks at around 670 cm^{-1} are due to the In-O bond [22] and around 600 cm^{-1} are due to Sn-O, also shown in Fig. 3-15 [26-28] labelled by (c) and (d), respectively. The FT-IR measurement of Fig. 3-15 shows that In_2O_3 has a relatively larger amount of organic species as compared to ITO. A relatively smaller amount of organic species in ITO compared to In_2O_3 may be one of the reasons for the degradation of patterning properties in ITO, as stated by Nagahara et al., the gel should have a high content of organic species to soften easily for good patterning properties [16]. The film thickness of the gel films measured by alpha-step profilometer are similar as; In_2O_3 : 273 nm, ITO via SnCl_2 : 280 nm, and ITO via $\text{Sn}(\text{acac})_2$: 243 nm. Since the film thicknesses are approximately same, it means that from the very beginning, organic species in In_2O_3 are more than in ITO.

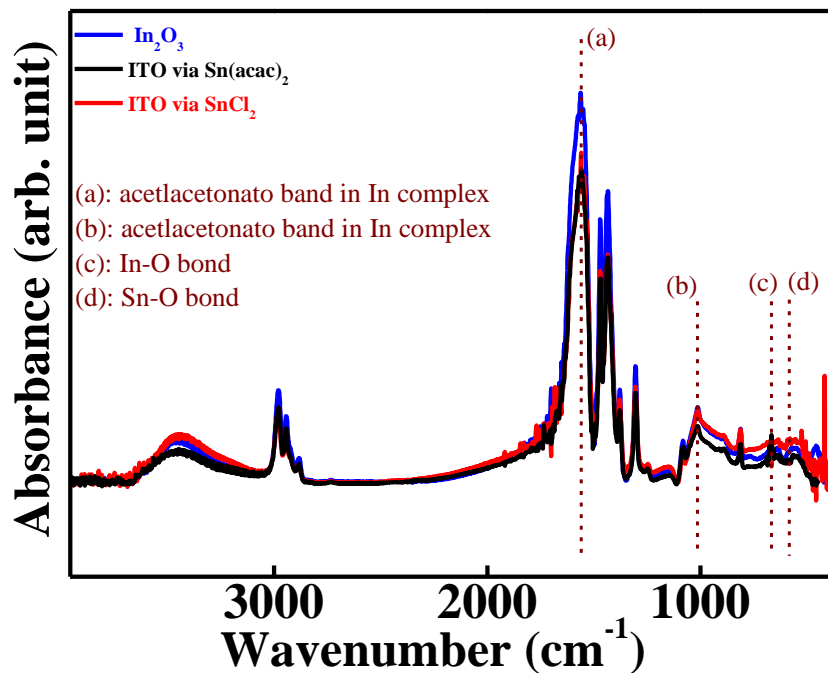


Fig. 3-15: FT-IR of In_2O_3 and ITO gel films.

The composition of the source solutions was further studied using cryospray ionisation Fourier transform ion cyclotron resonance mass spectroscopy (CSI-FT-ICR-MS). The mass spectra result from the positive mode measurements are shown in Fig. 3-16 and the inset shows the mass spectra for the m/z values from 0 to 500 on semi-log scale because these peaks were hardly visible on the linear scale. Figure 3-16 shows that most solutes have the general formula $\text{In}_n(\text{acac})_2(\text{PrA})_x(\text{CH}_3\text{O})_y$, where $n = 1-7$, x and y are positive integers, “PrA” is the propionate ligand ($\text{CH}_3\text{CH}_2\text{COO}^-$) and “acac” is acetylacetonate ligand ($\text{OCCH}_3\text{CHOCCH}_3^-$). CH_3O (or $-\text{CH}_2\text{OH}$) is the attachment of methanol to the solution because the source solutions were diluted with methanol for mass spectra analysis. The general formula suggests that the solute is mostly made up of the combination of $\text{In}(\text{acac})_2$ molecules and propionic acid molecules through van der Waals forces, which can also be stated as: In (indium) forms a basic structure with 1 In atom coordinated by 2 acac. The mass spectra show that In_2O_3 and ITO possess peaks at same m/z value, but the intensities are different, with a common pattern, which is shown in Table I.

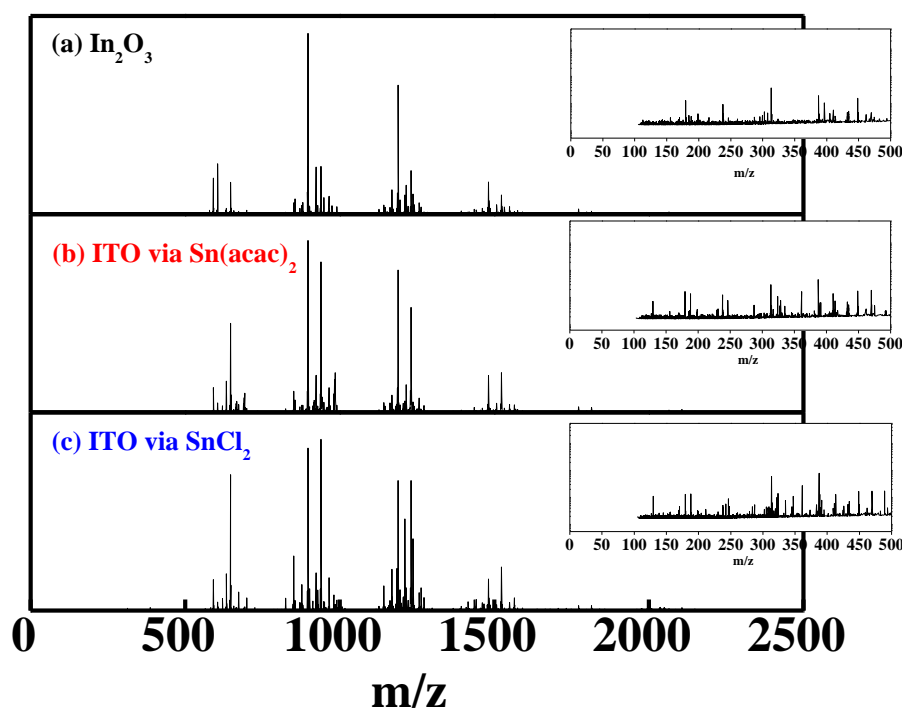
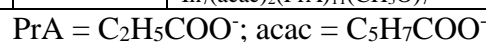


Fig. 3-16: CSI-FT-ICR-MS analysis of (a) In_2O_3 , (b) ITO via $\text{Sn}(\text{acac})_2$, and (c) ITO via SnCl_2 .

Table I. Structures corresponding to m/z value for In₂O₃ and ITO.

In ₂ O ₃ (A)		ITO via Sn(acac) ₂ (B)		ITO via SnCl ₂ (C)		Structure
Experimental mass	Theoretical mass	Experimental mass	Theoretical mass	Experimental mass	Theoretical mass	
312.99	312.99	312.99	312.99	312.99	312.99	In(acac) ₂
646.98	646.98	646.98	646.98	646.98	646.98	In ₂ (acac) ₂ (PrA) ₃
980.98	980.97	980.98	980.97	980.98	980.97	In ₃ (acac) ₂ (PrA) ₆
1230.94	1230.94	1230.95	1230.94	1230.95	1230.94	In ₄ (acac) ₂ (PrA) ₇ (CH ₃ O) ₂
1480.91	1480.91	1480.92	1480.91	1480.92	1480.91	In ₅ (acac) ₂ (PrA) ₈ (CH ₃ O) ₄
1730.89	1730.88	1730.89	1730.88	1730.85	1730.8537	In ₆ (acac) ₂ (PrA) ₉ (CH ₃ O) ₆ , <i>for A and B</i> In ₆ (acac) ₆ (PrA) ₅ (CH ₃ O)(CH ₃)HCl, <i>for C</i>
604.97	604.97	604.97	604.97	604.97	604.97	In ₂ (acac) ₂ (PrA) ₂ (CH ₃ O)
938.96	938.96	938.96	938.96	938.96	938.96	In ₃ (acac) ₂ (PrA) ₅ (CH ₃ O)
1272.96	1272.95	1272.96	1272.95	1272.96	1272.95	In ₄ (acac) ₂ (PrA) ₈ (CH ₃ O)
1522.93	1522.92	1522.93	1522.92	1522.93	1522.92	In ₅ (acac) ₂ (PrA) ₈ (CH ₃ O)
1772.90	1772.89	1772.90	1772.89	1772.90	1772.90	In ₆ (acac) ₂ (PrA) ₁₀ (CH ₃ O) ₅ , <i>for A and B</i> In ₆ (acac) ₆ (PrA) ₅ (CH ₃ O)(C ₄ H ₉)HCl, <i>for C</i>
2022.87	2022.86	--	--	--	--	In ₇ (acac) ₂ (PrA) ₁₁ (CH ₃ O) ₇



From the mass spectra, it was evident that In₂O₃, ITO via Sn(acac)₂, and ITO via SnCl₂ have almost the same solute structures, except for SnCl₂, where there was a peak containing Cl at the higher m/z value. In the similar way, more peaks containing In and organics along with Cl or Cl and Sn, or Sn are expected at higher m/z values. Although having similar structures of solute, the patterns degraded (as shown in Fig. 3-9) with the addition of Sn. This is due to the reason that In₂O₃ has viscoelastic changes similar to glass transition as in the case of polymers, while, with the addition of Sn, the viscoelastic properties are modified as shown in Fig. 3-17, which presents the viscoelastic properties of In₂O₃ and ITO semi-solid pallet. The viscoelastic properties were measured using a rheometer, in which the sample was sandwiched between two clips. The measurements were performed using dynamic viscoelastic measurement with sine wave in the temperature dependence mode (i.e. oscillatory mode). The sample was fabricated by drop-casting the In₂O₃ and ITO solution onto a glass petri dish, then heating it at 100 °C in air, finally pulverising it from the petri dish. The obtained semi-solid powder was formed in a shape of a pellet (1 mm thick) at room temperature using a compression-molding machine.

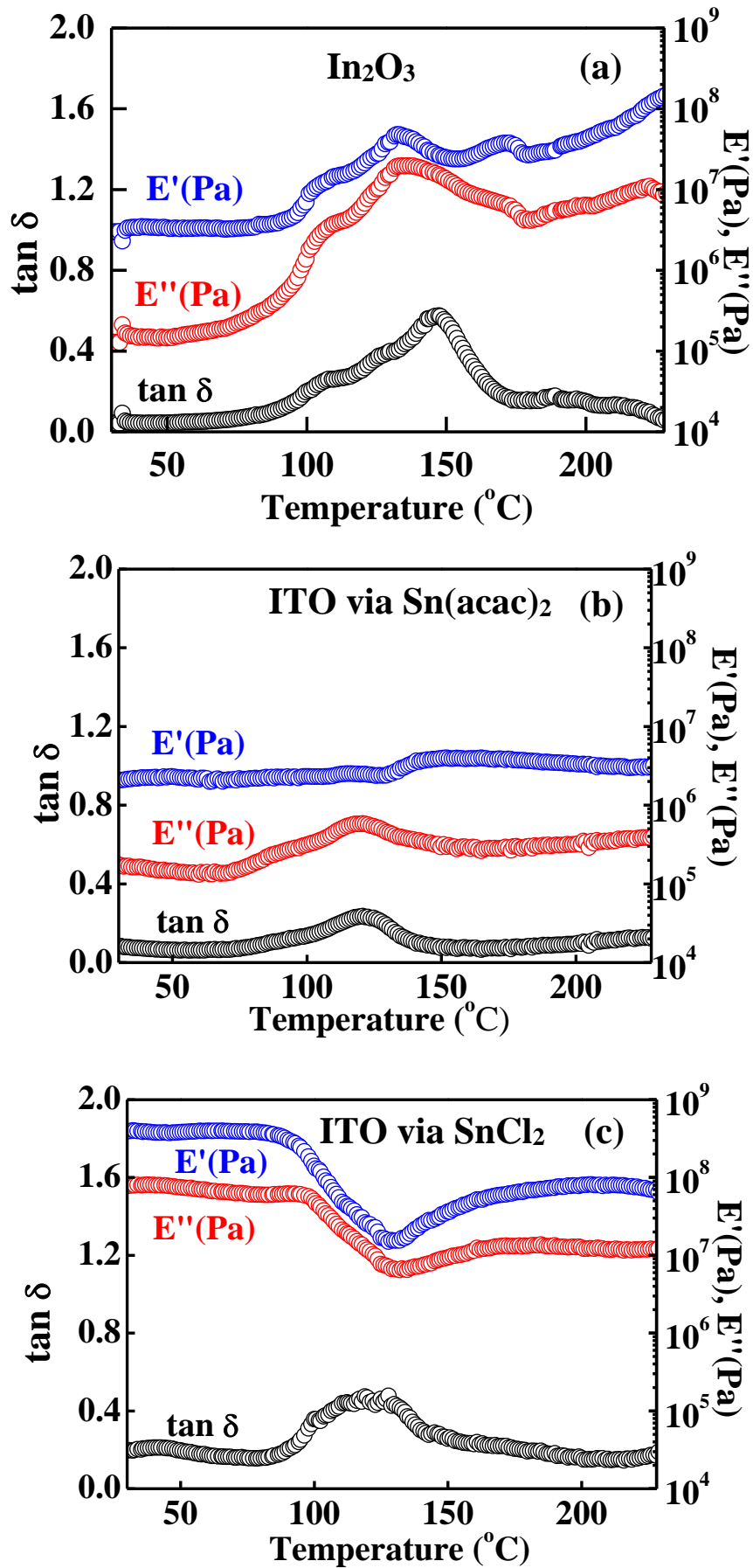


Fig. 3-17: Viscoelastic properties of (a) In₂O₃, (b) ITO via Sn(acac)₂, and (c) ITO via SnCl₂.

From Fig. 3-17, it is seen that the $\tan \delta$ for In_2O_3 is higher than that for ITO, which means the In_2O_3 gel becomes softer at a certain temperature than ITO. Hence, it can be concluded that In_2O_3 shows better viscoelastic transformation under pressure and temperature compared to ITO, which may explain the degradation of patterns with the addition of tin for n-RP experiments.

To study the effect of direct imprinting on the electrical properties of 600 °C annealed films, SIMS measurement was performed and the results are shown in Fig. 3-18. The carbon concentration in the imprinted In_2O_3 was more than non-imprinted In_2O_3 films, but in ITO, the carbon concentration was almost the same for imprinted and non-imprinted films. Indium precursor (i.e. $\text{In}(\text{acac})_3$) and the solvent (i.e. PrA) are themselves sources of carbon in the films.

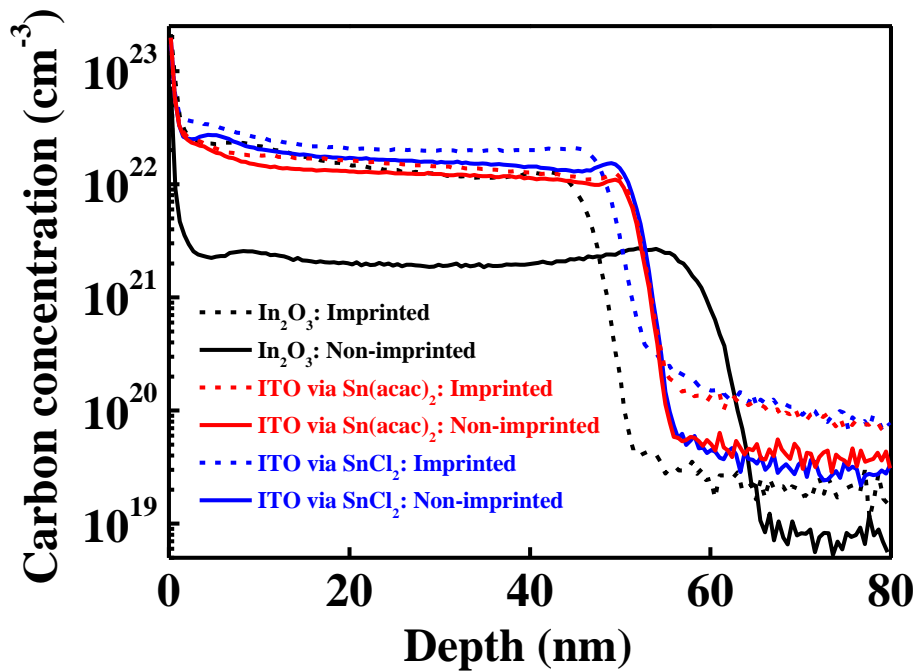


Fig. 3-18: SIMS profile of imprinted and non-imprinted In_2O_3 and ITO films, after annealing.

The imprinting temperature in this experiment was 175 °C and at this temperature, the organic species in the precursor gel film (like PrA, acac) try to evaporate from the film. However, at the same time, the films are under pressure (i.e. imprinting pressure), thereby preventing

evaporation of the organic species to some extent. It is interesting to note that the carbon concentration is larger for the imprinted film than the non-imprinted film, even though the films were annealed at 600 °C in oxygen ambient after the imprint process. These trapped carbons act as scattering centres that lead to a reduction in the mobility of the films in the case for In₂O₃. Whereas the ITO gel has less effect of imprinting pressure on the residual carbon concentration due to a lower tan δ value, which corresponds to the experimental result that Hall mobility reduction is not so pronounced for ITO.

As shown in Fig. 3-14 that the carrier concentration in In₂O₃ increased by the imprinting process, but does not change much in ITO. This corresponds to the fact that the precursor gel has not deformed much in ITO as much as in In₂O₃. This deformation may create oxygen vacancies, which are a source of carrier concentration in In₂O₃ [29-31]. To confirm this, the chemical bonding was studied using XPS, as shown in Fig. 3-19, where the x-axis represents the intensity (arb. unit) and y-axis represents binding energy (eV). The XPS peaks were calibrated using the binding energy of 284.6 eV for carbon. The oxygen 1s peak has been deconvoluted into three positions: the peak at lower binding energy due to metal-oxide bonds (M-O bond), the medium binding energy due to oxygen vacancies (O vacancy), and the higher binding energy due to oxygen of the free hydroxyl group (OH bonds), which is caused by the water molecules absorbed on the surface [32]. To understand the difference between samples, the peak area ratio was calculated, $\frac{O \text{ vacancies}}{M-O \text{ bonds}}$ as a measure of the formation of oxygen vacancies. The values of $\frac{O \text{ vacancies}}{M-O \text{ bonds}}$ shown in the top right-hand side of Fig. 3-19 are presented in Table II.

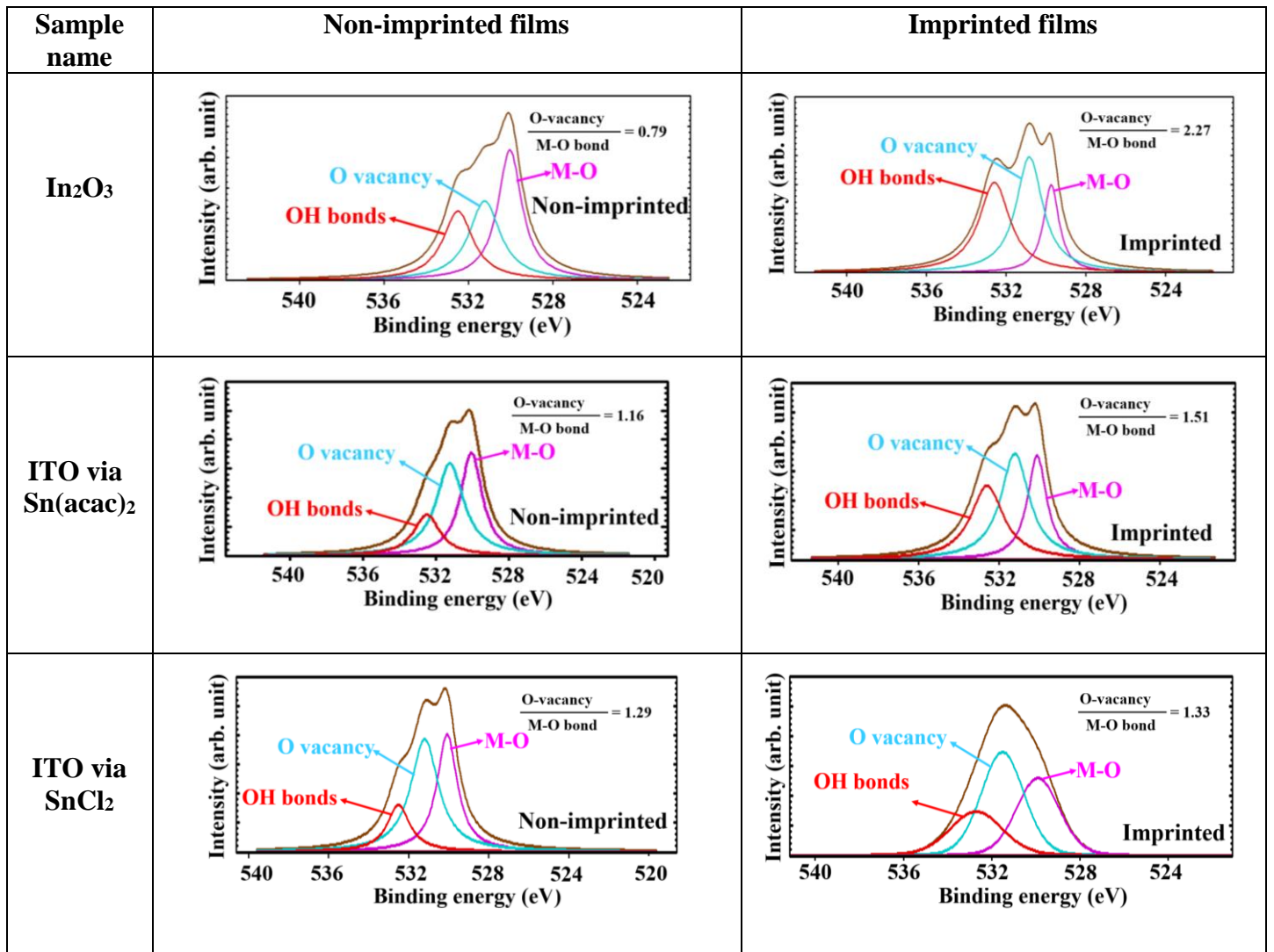


Fig. 3-19: XPS spectra of In_2O_3 and ITO for oxygen 1s peak.

Table II. Area ratio of O-vacancy/M-O bond.

	Non-imprinted		Imprinted
In_2O_3	0.8	<	2.3
ITO via $\text{Sn}(\text{acac})_2$	1.2	\approx	1.5
ITO via SnCl_2	1.3	=	1.3

From Fig. 3-19, it is evident that for the imprinted In_2O_3 film, the peak area ratio $\frac{O \text{ vacancies}}{\text{M-O bonds}}$ is as large as 2.3, while for the non-imprinted case, it is 0.8. As oxygen vacancies are responsible for free carriers in In_2O_3 [23], the structure is deformed during imprinting, leading to more oxygen vacancies. A similar analysis was conducted by Kim et al. [33] and Wu and Chiou [34], where the former reported that as the oxygen content increases, the carrier concentration decreases and the later showed that as the oxygen content increases, the ratio $\frac{O \text{ vacancies}}{\text{M-O bonds}}$ decreases. As explained above, the structure of ITO does not deform much during imprinting, so the ratio of $\frac{O \text{ vacancies}}{\text{M-O bonds}}$ is similar for imprinted and non-imprinted samples in the case of ITO. Hence, the carrier concentration remains almost the same for ITO films.

Finally, the crystalline properties were characterised by XRD. Figures 3-20 (a) and 20 (b) show the XRD of the imprinted and non-imprinted In_2O_3 and ITO films, respectively, with almost no peaks observed for imprinted In_2O_3 and ITO films, suggesting the imprinted films are amorphous in nature. In contrast, (222) and (400) diffraction peaks were found for non-imprinted films, indicating that the imprinting process prevents the crystallisation of In_2O_3 , probably due to the large residual carbon content. This also corresponds to the experimental result that the mobility of imprinted film was smaller than that of non-imprinted films.

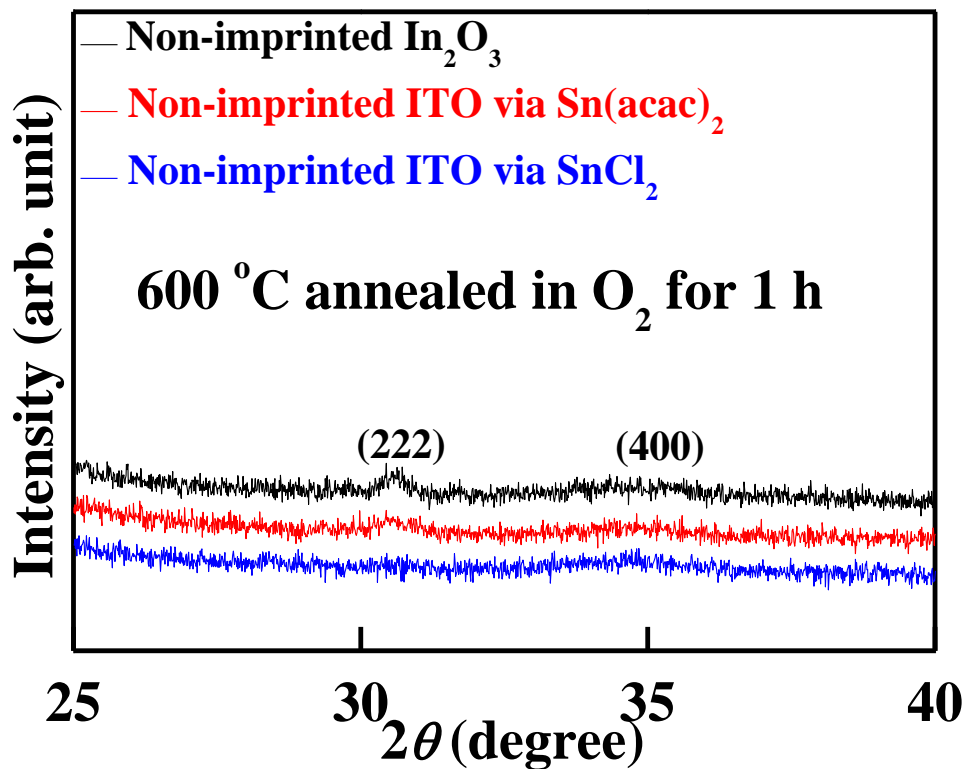
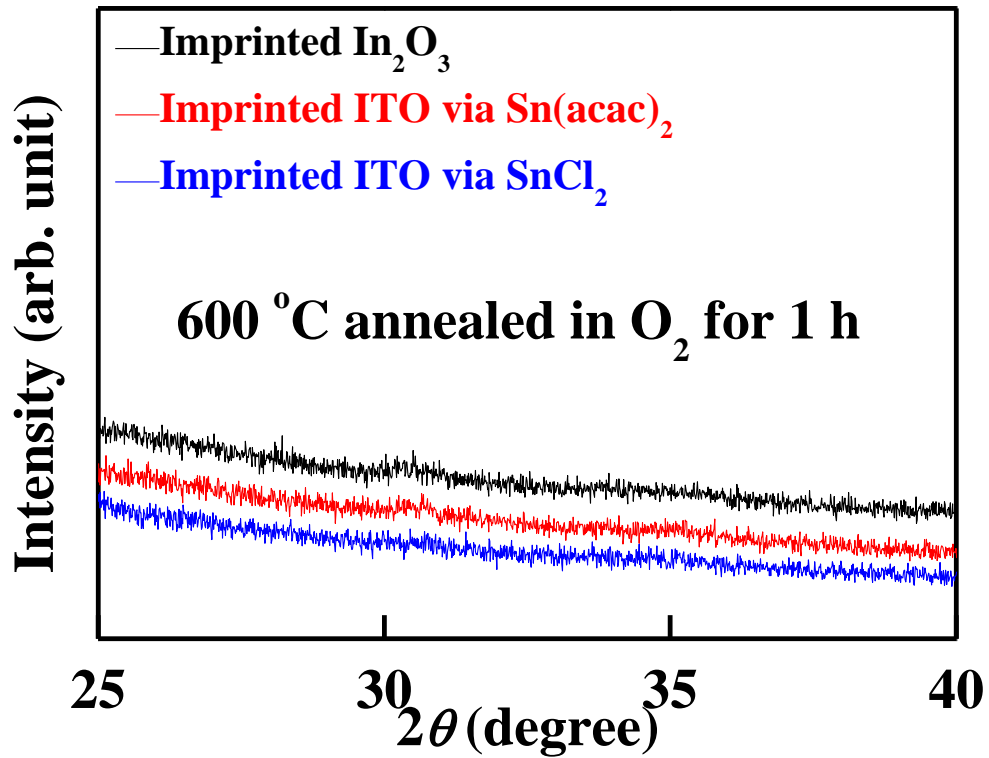


Fig. 3-20: XRD of (a) imprinted and (b) non-imprinted, In_2O_3 and ITO films.

Summary

N-RP is a resist-free, direct patterning technique to achieve patterns in the metal-oxide precursor gel in the nanoscale range, allowing precise shape control. During n-RP, the precursor gel is deformed by the application of the appropriate imprinting temperature and pressure. The addition of tin (Sn) to In_2O_3 degrades (i.e. ITO) the n-RP properties because the $\tan \delta$ value of ITO is smaller than that of In_2O_3 . Consequently, the electrical properties of imprinted ITO films are not altered as much as compared to non-imprinted ITO films, but are greatly affected in the case of imprinted In_2O_3 compared to the non-imprinted In_2O_3 films. The Hall mobility of imprinted In_2O_3 decreases due to the trapped carbon, as confirmed by SIMS measurements, which showed that even after annealing at 600 °C for 1 hour, there was more carbon in the imprinted In_2O_3 than non-imprinted In_2O_3 . An increase in the carrier concentration in imprinted films is due to the increase in oxygen vacancies in In_2O_3 after imprinting, as confirmed by XPS studies.

References

1. M. Mashayekhi, A. Conde, T.N. Ng, P. Mei, E. Ramon, C. Martinez-Domingo, A. Alcalde, L. Teres, and J.C. Bordoll, *J. Disp. Technol.*, **11** (2015) 658.
2. G.D. Martin, S.D. Hoath, and I.M. Hutchings, *J. of Phys. Conf. Ser.*, **105** (2008) 012001.
3. T.R. Hebner, C.C. Wu, D. Marcy, M.H. Lu, and J.C. Sturm, *Appl. Phys. Lett.*, **72** (1998) 519.
4. T. Kaneda, D. Hirose, T. Miyasako, P.T. Tue, Y. Murakami, S. Kohara, J. Li, T. Mitani, E. Tokumitsu, and T. Shimoda, *J. Mater. Chem. C.*, **2** (2014) 40.
5. E. Sowade, E. Ramon, K.Y. Mitra, C. Martínez-Domingo, M. Pedró, J. Pallarès, F. Loffredo, F. Villani, H.L. Gomes, L. Terés, and R.R. Baumann, *Scientific Reports.*, **6** (2016) 33490.
6. Y. Takeda, K. Hayasaka, R. Shiwaku, K. Yokosawa, T. Shiba, M. Mamada, D. Kumaki, K. Fukuda, and S. Tokito, *Scientific Reports.*, **6** (2016) 25714.
7. J. Branson, J. Naber, and G. Edelen, *IEEE T. Educ.*, **43** (2000) 257.
8. S. Khan, L. Lorenzelli, and R.S. Dahiya, *IEEE Sens. J.*, **15** (2015) 3164.
9. J. Suikkola, T. Björninen, M. Mosallaei, T. Kankkunen, P. Iso-Ketola, L. Ukkonen, J. Vanhala, and M. Mäntysalo, *Scientific Reports*, **6** (2016) 25784.
10. T. Arai, N. Sato, K. Yamaguchi, M. Kawasaki, M. Fujimori, T. Shiba, M. Ando, and K. Torii, *Jpn. J. Appl. Phys.*, **46** (2007) 2700.
11. B. E. Park, H. Ishiwara, M. Okuyama, S. Sakai, and S. M. Yoon: *Ferroelectric-Gate Field Effect Transistor Memories* (Springer, Netherlands, 2016) 1st ed., p. 344.
12. K. Haga, Y. Kamiya, and E. Tokumitsu, *Jpn. J. Appl. Phys.*, **57** (2018) 02CB14.
13. J. Huang, B. Yan, A. Faghihnejad, H. Xu, and H. Zeng, *Korea-Aust Rheol. J.*, **26** (2014) 3.
14. D. Hirose, H. Koyama, K. Fukada, Y. Murakami, K. Satou, S. Inoue, and T. Shimoda,

Phys. Status Solidi A, **214** (2017) 1600397.

15. P. T. Tue, K. Fukada, and T. Shimoda, *Appl. Phys. Lett.*, **111** (2017) 223504.
16. K. Nagahara, D. Hirose, J. Li, J. Mihara, and T. Shimoda, *Ceram. Int.*, **42** (2016) 7730.
17. H. Koyama, K. Fukada, Y. Murakami, P.T. Tue, S. Tanaka, S. Inoue, and T. Shimoda, *SID Int. Symp. Dig. Tec.*, **45** (2014) 979.
18. M. Terai, K. Fujita, and T. Tsutsui, *Jpn. J. Appl. Phys.*, **44** (2005) 1059.
19. A. Ginsburg, M. Priel, H.N. Barad, D.A. Keller, E. Borvick, K. Rietwyk, A. Kama, S. Meir, A.Y. Anderson, and A. Zaban, *Sol. Energy Mater. Sol. Cells*, **179** (2018) 254.
20. D. J. Seo, J. P. Shim, S. B. Choi, T.H. Seo, E. K. Suh, and D. S. Lee, *Optics Express*, **20** (2012) A991.
21. R. M. Pasquarelli, C. J. Curtis, A. Miedaner, M. F. A. van Hest, R. P. O Hayre, and D. S. Ginley, *Inorg. Chem.*, **49** (2010) 5424.
22. M. Epifani, R. Diaz, J. Arbiol, P. Siciliano, and J. R. Morante, *Chem. Mater.*, **28** (2006) 840.
23. https://chem.libretexts.org/Reference/Reference_Tables/Spectroscopic_Parameters/Infrared_Spectroscopy_Absorption_Table.
24. S. Luo, J. Feng, and K.M. Ng, *Cryst. Eng. Comm.*, **17** (2015)1168.
25. K.P. Gattu, K. Ghule, A.A. Kashale, V.B. Patil, D.M. Phase, R.S. Mane, S.H. Han, R. Sharma, and A.V. Ghule, *RSC Adv.*, **5** (2015) 72849.
26. M. Thirumoorthi and J. T. J. Prakash, *J. Asian Ceram. Soc.*, **4** (2016) 124.
27. M. Moradi-Haji Jafan, M.-R. Zamani-Meymian, R. Rahimi, and M. Rabbani, *J Nanostructure Chem.*, **4** (2014) 89.
28. A. M. Sayed and S. M. Yakout, *Journal of Research in Nanotechnology*, **2016** (2016) 1.
29. A. Facchetti and T. J. Marks: *Transparent Electronics* (John Wiley & Sons. Ltd,

Chichester, 2010) 1st ed., p. 8.

30. G. Frank, H. Kostlin, and A. Rabenau, *Phys. Stat. Sol. (a)*, **52** (1979) 231.
31. N. Nadaud, N. Lequeux, and M. Nanot, *J. Solid State Chem.*, **135** (1998) 140.
32. W. C. Chang, C. H. Kuo, C. C. Juan, P. J. Lee, Y. L. Chueh, and S. J. Lin, *Nanoscale Res. Lett.*, **7** (2012) 684.
33. S. M. Kim, H. W. Choi, K. H. Kim, S. J. Park, and H. H. Yoon, *J. Korean Phys. Soc.*, **55** (2009) 1996.
34. W. F. Wu and B. S. Chiou, *Semicond. Sci. and Technol.*, **11** (1999) 196.

4. Solution Derived High k -dielectric Materials

4.1 Introduction

With a continuous scaling down of metal-oxide-semiconductor field effect transistor (MOSFET) technology, the equivalent oxide thickness (EOT) assuming SiO₂ gate dielectric films approach to 1.2 nm. Such a thickness, leads to the problem of large leakage current density (over 1A/cm²) due to direct electron tunneling as well as poor gate reliability. To overcome these problems and to maintain a high capacitance, thicker dielectric layer with larger dielectric constant is necessary which can replace SiO₂ and SiO_xN_y. Such materials are called high- k gate dielectrics, which allow physically thicker gate insulator films, which reduce leakage current; while still have large MOS capacitance density, as necessary for further MOS scaling [1-5]. The requirements of high- k materials are-

- a. Good thermodynamic stability with Si due to direct contact with Si
- b. Good interface quality with silicon
- c. Comparable with conventional SiO₂
- d. Apart from their high- k constant, large band gap and band offsets are required

A large number of high- k materials are used as gate-dielectrics. Some of them are gadolinium oxide Gd₂O₃ [6], magnesium oxide MgO [7], erbium oxide Er₂O₃ [8], neodymium oxide Nd₂O₃ [9], praseodymium oxide Pr₂O₃ [10], cerium oxide CeO₂ [11], cerium zirconate CeZrO₄ [12], aluminum oxide Al₂O₃, [13], lanthanum oxide La₂O₃ [14], yttrium oxide Y₂O₃ [15], tantalum pentoxide Ta₂O₅ [16], titanium dioxide TiO₂ [17], zirconium dioxide ZrO₂ [18], hafnium oxide HfO₂ [19], etc. Among these, HfO₂ has been selected due to its advantages like [20-23]:-

- Relatively high dielectric constant, ($k_{\text{HfO}_2} \approx 22 \gg k_{\text{SiO}_2} = 3.9$)
- Compatible with CMOS processing
- High breakdown field ($> 5 \text{ MV/cm}$)
- Thermal stability in contact with Si

Thin films of pure HfO_2 (i.e. undoped HfO_2) to replace SiO_2 , first came into existence into commercial products since its first use in Penryn chip by Intel in 2007. After this, HfO_2 has been used in numerous applications like passivation layer in devices such as high temperature and high power electronics, based on silicon carbide [24], sensitive layer in ion selective field effect transistor [25].

Hafnium belongs to group 4 transition element in periodic table. Hafnium in the presence of oxygen, forms a stable oxide, hafnium dioxide. The phase diagram of Hf and O under 1 atm. and room temperature is shown in Fig. 4-1. It is seen from this phase diagram, that HfO_2 has three phases: monoclinic, below $1670 \text{ }^\circ\text{C}$; tetragonal phase from 1670 to $2200 \text{ }^\circ\text{C}$; and cubic phase, from 2200 to $2810 \text{ }^\circ\text{C}$. The change in crystal structure of HfO_2 as a function of temperature is often summarized as: monoclinic \rightarrow tetragonal \rightarrow cubic. Tetragonal/cubic phase has higher k than monoclinic phase [26]. By increasing the pressure between 4 to 11 GPa, orthorhombic phase can also be obtained. Table I summarizes the dielectric constant and bandgap for different phases of HfO_2 .

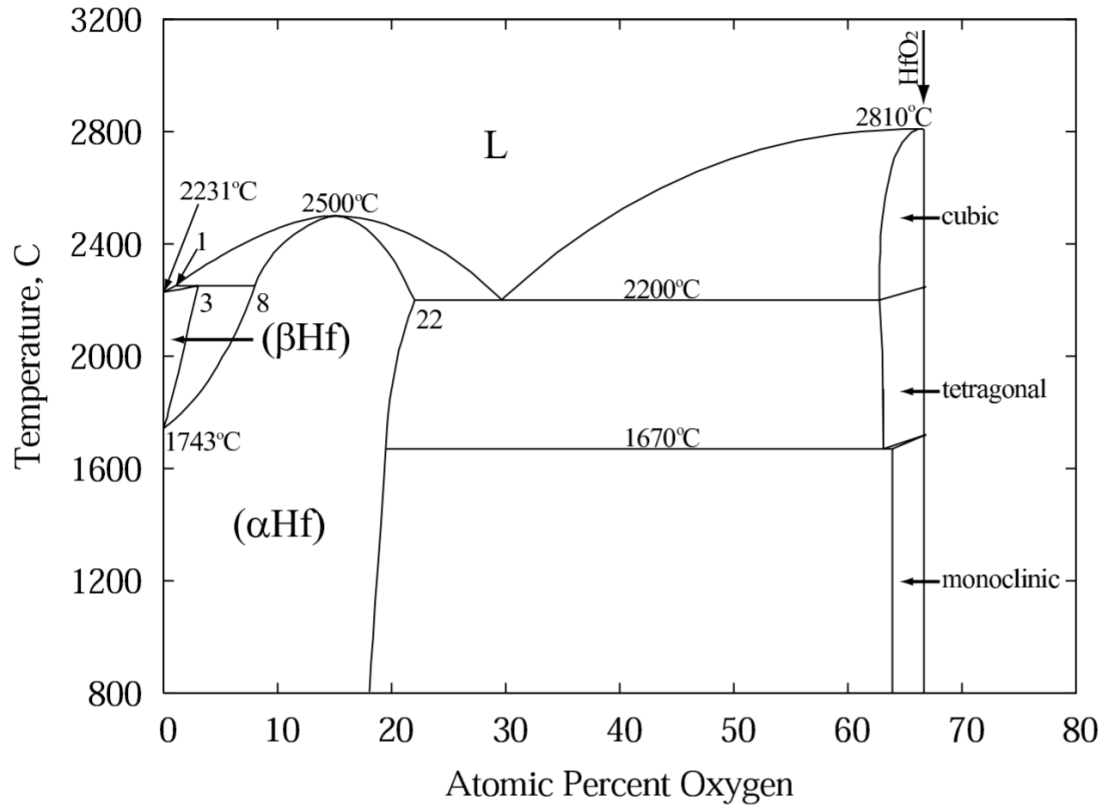


Fig. 4-1: Phase diagram of HfO₂ from Massalski [27].

Table I: Band gaps and averaged dielectric constant for crystalline phases of HfO₂

Phase	E _g	ε _r
Cubic	5.53 [28]	29 [29]
Tetragonal	5.79 [28]	70 [29]
Monoclinic	5.65 [28]	15-25 [29]

HfO₂ is used in two forms, one is pure (undoped) HfO₂ and another is doped HfO₂. Pure HfO₂ crystallizes into monoclinic phase and shows paraelectricity. Doped HfO₂ (i.e. HfO₂ doped with dopants like Y, Zr, or Si, etc.), crystallizes into orthorhombic phase and shows ferroelectricity [30].

In my work, we have investigated the electrical properties (i.e. polarization-electric field, capacitance-voltage, and leakage current density-electric field) of solution-processed HfO₂

films deposited on Pt/Ti/SiO₂/Si substrate. To study the electrical properties, we fabricated metal-insulator-metal (MIM) capacitor, using ITO/HfO₂/Pt type configuration (or, ITO/HfO₂/Pt/Ti/SiO₂/Si configuration). By XRD, it was found that undoped HfO₂ is monoclinic in phase and shows paraelectric properties, as confirmed by polarization-electric field and capacitance-voltage studies.

4.2 Experimental procedure

HfO₂ thin films were prepared by solution process using hafnium acetylacetonate (Hf(acac)₄) in propionic acid (PrA). Pure HfO₂ with a molar concentration of 0.2 mol/kg was used in this work. The source solution of HfO₂ was prepared by mixing proper amount of Hf(acac)₄ and PrA on a magnetic stirrer for 1 h at 120 °C at 1000 rpm. After this, the solution was allowed to cool down and finally it was filtered with 0.2 μm pore size of filter paper. This is shown schematically in Fig. 4-2.

To fabricate metal-insulator-metal (MIM) capacitor, Pt/Ti/SiO₂/Si substrate (hereinafter called as “Pt substrate”) was used. Pt substrate was first cleaned by ultra-sonicating in acetone for 10 min, then in isopropanol alcohol (IPA) for 10 min, and then in de-ionized water (DI) for 10 min. Finally, Pt substrate was purged with N₂ gas. HfO₂ source solution was spin coated on Pt substrate at 1500 rpm for 20 s. Then the HfO₂ coated Pt substrate was dried at 225 °C for 3 min on hot plate to evaporate the solvent and to make the film dense. Then, again HfO₂ source solution was spin-coated on it at 1500 rpm for 20 s and again dried at 225 °C for 3 min. Finally, third-time HfO₂ was spin-coated and this time it was dried at 100 °C. The complete spin-coating and drying conditions are:

slope/2sec → 500rpm/5sec → slope/2sec → 1500rpm/20sec → slope/2sec (**dry: 225°C/3min**); 2 times

slope/2sec → 500rpm/5sec → slope/2sec → 1500rpm/20sec → slope/2sec (**dry: 100°C/3min**); 1 time

Above process gave us gel film. To make this gel film into solid oxide film, gel film was annealed in rapid thermal annealing (RTA) in O₂ environment. RTA annealing was done by varying the annealing temperature from 500 to 700 °C with an annealing time of 15 min.

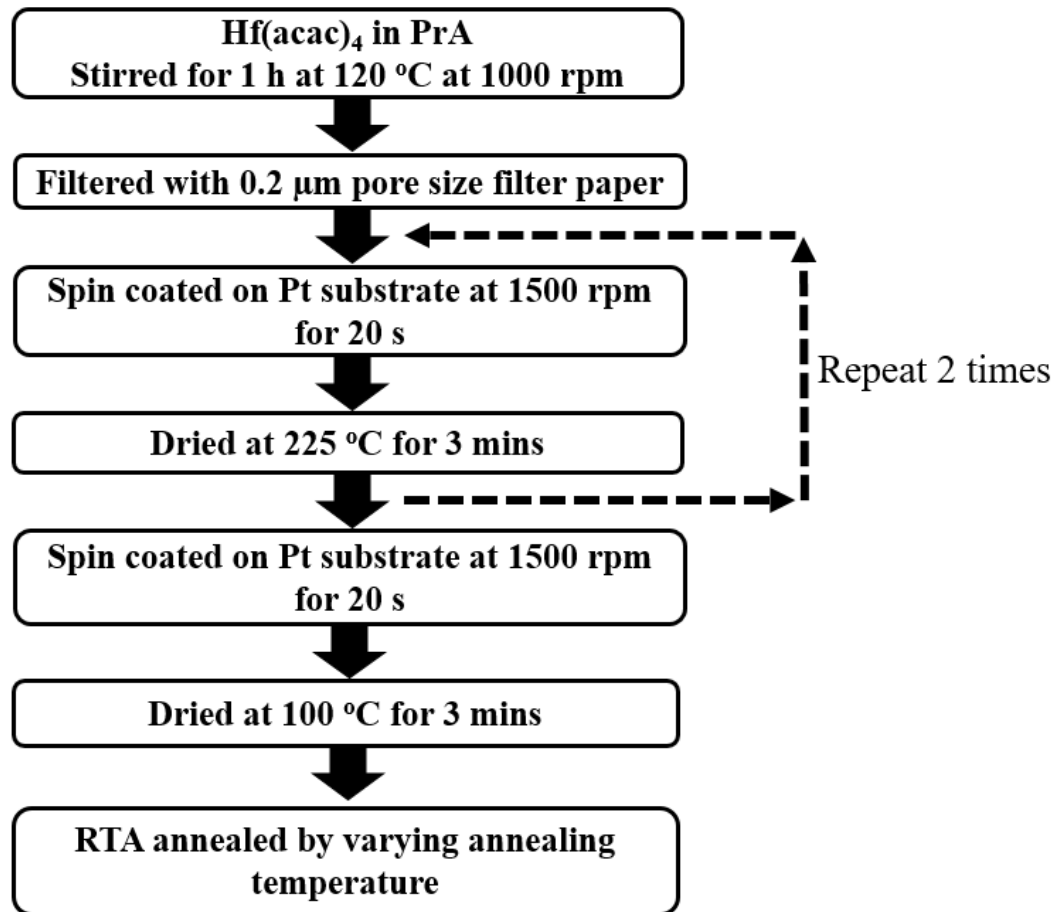


Fig. 4-2: Formation of HfO₂ solid thin film from source solution.

The crystalline phase of HfO₂ films on Pt substrate was characterized by X-ray diffraction (XRD) analysis. X'PERT PRO with monochromatic Cu K α (1.54 Å) was used for GI-XRD measurements. The surface morphology was studied via atomic force microscope (AFM) using HITACHI AFM5000II SPA-400 in tapping mode.

To measure the electrical properties, an electrode on top of HfO₂ (top electrode) is needed to make it MIM capacitor, while Pt was used as bottom electrode. To make the top electrode, indium-tin-oxide (ITO) was used. 1 wt.% ITO was used with a molar concentration of

0.3 mol/kg was used. Indium acetylacetonate ($\text{In}(\text{acac})_3$) and tin acetylacetonate ($\text{Sn}(\text{acac})_2$) in PrA were used to synthesise ITO source solution. The source solution to precursor-gel conversion of ITO was done by spin-coating ITO on HfO_2/Pt sample with the conditions shown below:

slope/2sec \rightarrow 500rpm/5sec \rightarrow slope/2sec \rightarrow 1500rpm/20sec \rightarrow slope/2sec (**dry**: 100°C/3min)

Finally, ITO was annealed in RTA for 1 h in O_2 environment (this condition was adopted after optimization, as discussed in chapter 2). This gave MIM capacitor structure. However, for electrical characterizations, we need to pattern the ITO films. In addition, to measure the thickness of HfO_2 thin film and to make the contact from the bottom Pt electrode, we need to etch the HfO_2 film. This was done by photolithography as shown in Fig. 4-3. First ITO patterning was done by lithography and then again, lithography was done to etch the HfO_2 film. To etch ITO and HfO_2 , hydrochloric acid (HCl) and hydrofluoric (HF) acid were used, respectively. The top electrode (i.e. ITO) after patterning is a square in shape with an area of $100 \times 100 \mu\text{m}^2$. The electrical characterization i.e. polarization-electric field (P-E), capacitance-voltage (C-V), and current density-electric field (J-E), of the MIM capacitor were measured. P-E, C-V, and J-E were studied using Toyo 6252 ferroelectric characterization system, Wayne Kerr 6400B precision component analyzer, and Agilent 4155C semiconductor parameter analyzer, respectively. The patterns were checked by optical microscope while the thickness of the electrodes and HfO_2 film, were measured using alpha-step profilometer.

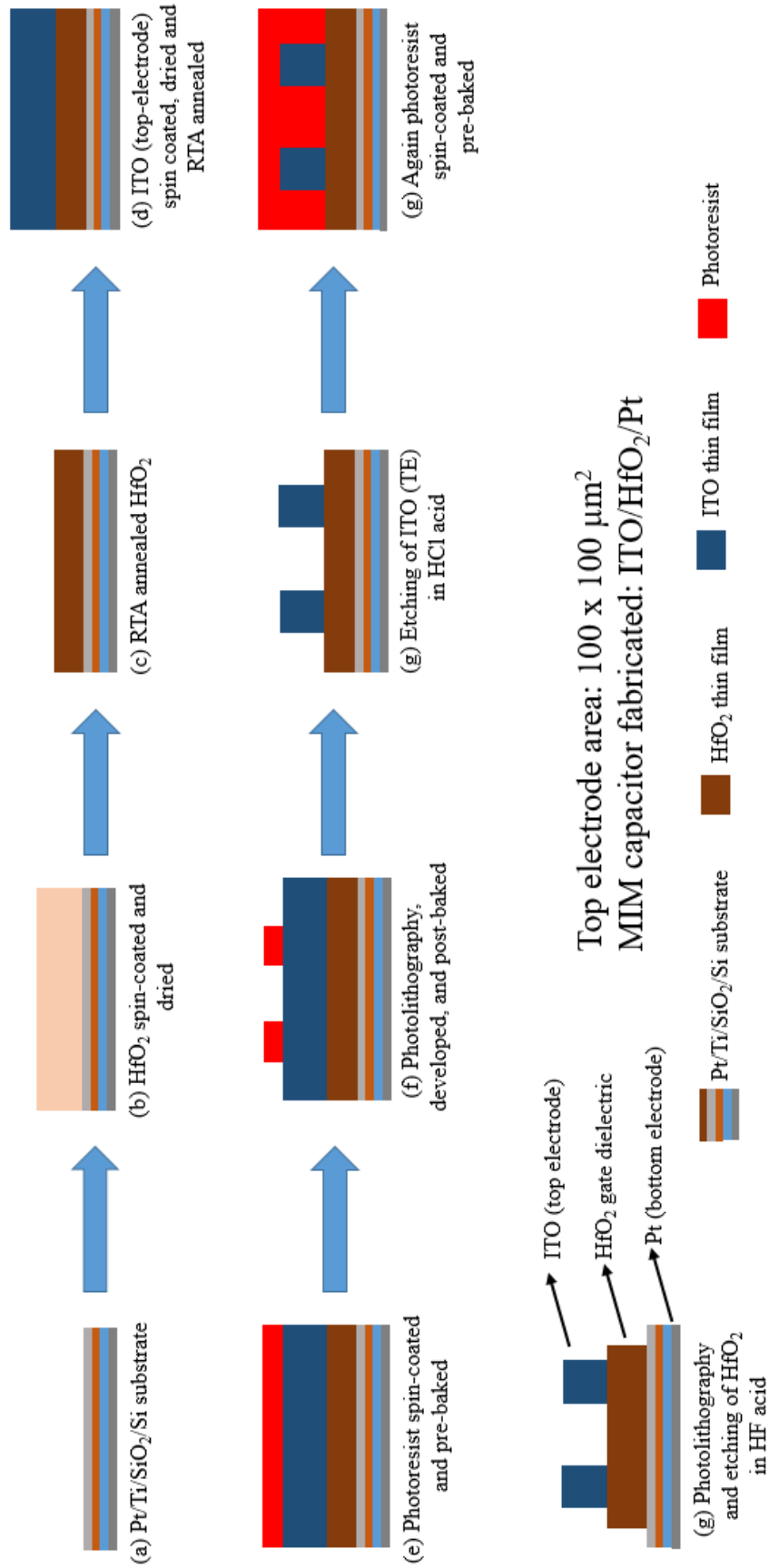
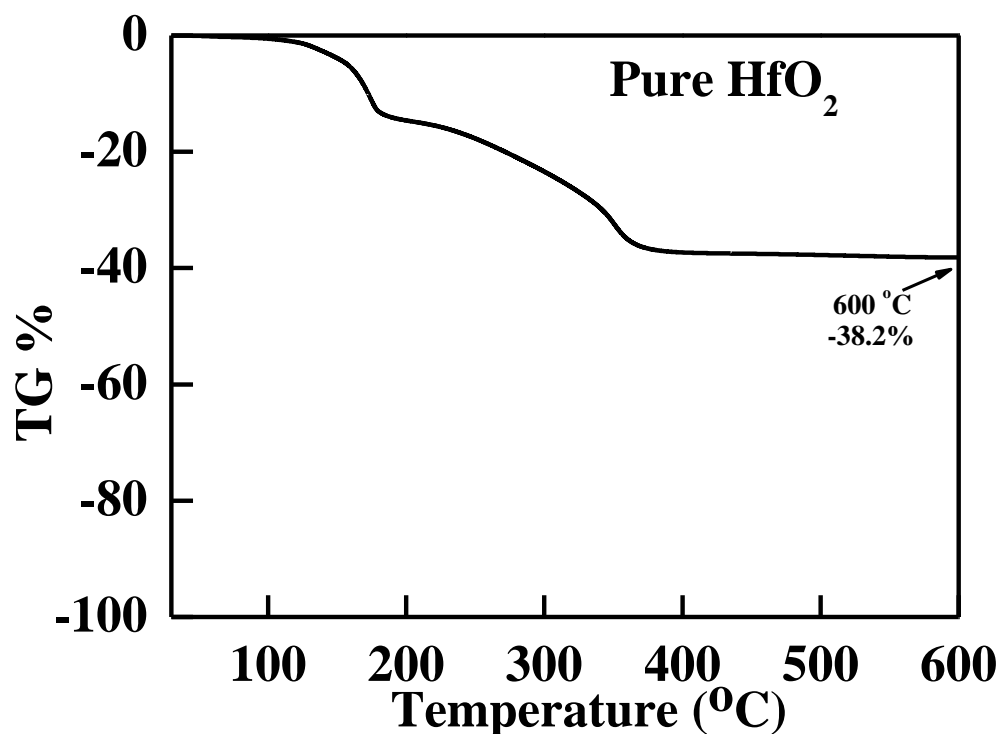


Fig. 4-3: Patterning of ITO, and etching of HfO₂ film, to make MIM capacitor.

4.3 Results and discussion

To study the crystallization temperature of HfO₂, TG-DTA was performed on HfO₂ source solution. TG-DTA was measured in air (flow rate: 200 ml min⁻¹) with a heating rate of 10 °C min⁻¹, where heating was performed from room temperature to 600 °C. Figure 4-4 shows the thermal behaviour of HfO₂ source solution. It is seen that two weight loss regions are observed, first in temperature range from room temperature to around 175 °C and second in the temperature range from 250 to 350 °C. The first weight loss is due to the evaporation of the solvent, which completes around 175 °C. This is also characterized by an endothermic peak in DTA graph, at around 175 °C, which indicates the evaporation of the solvent. The next weight loss starts from around 250 °C and finishes around 350 °C. This weight loss is due to the crystallization of HfO₂ precursor by the decomposition of organic species. DTA curve also shows an exothermic peak around 350 °C, corresponding to HfO₂ crystallization.



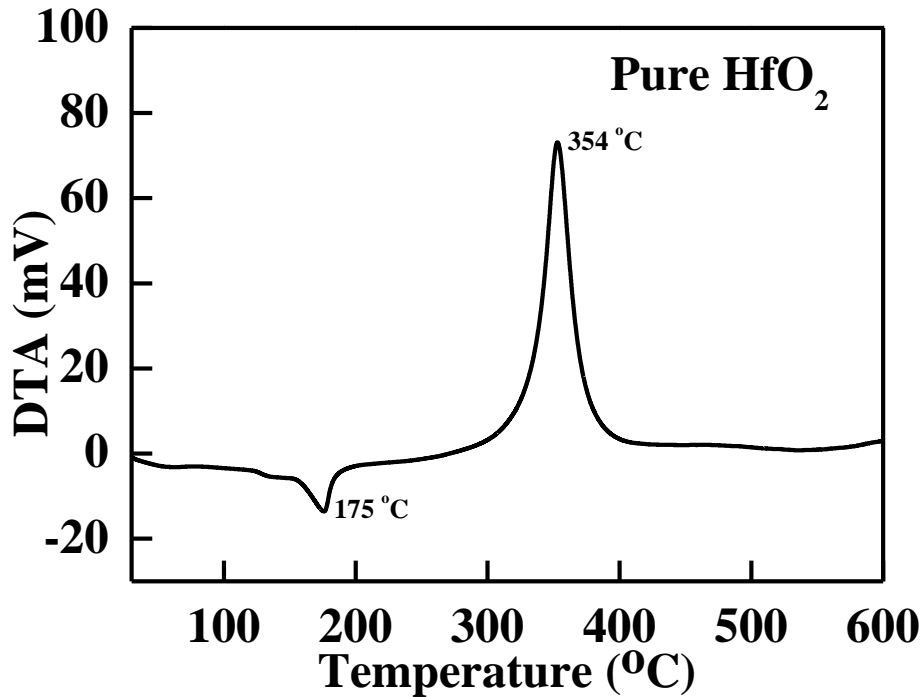


Fig. 4-4: Thermal behaviour of HfO₂ source solution.

Figure 4-5 shows the electrical characteristics (P-E and C-V) of MIM capacitor, where the insulator layer i.e., HfO₂ precursor gel film, was annealed in O₂ for 15 min at 500, 600, and 700 °C. Figure 4-6 shows the leakage current density (J-E) of the same films. Table II gives relative dielectric constant (ϵ_r), breakdown field (E_{bd}), leakage current density at 1 MV/cm and thickness of 500, 600, and 700 °C annealed film. Figures 4-7 and 4-8 show the crystallinity behaviour studied by XRD measurements and surface morphology of the films measured by AFM (for an area of 1 x 1 μm^2), while Table III gives the RMS roughness. As stated earlier, for electrical properties measurements, ITO top electrode was annealed for 1 h, but XRD and AFM studies were performed before ITO deposition. It is seen from Table II, that, as the annealing temperature increased, thickness of HfO₂ reduced. This is due to the reason that at higher annealing temperature, more organic species are removed from the films and densification of films take place. Hence, film quality improves. This densification of the films at higher annealing temperature is a reason for the increase of breakdown voltage with annealing temperature. The lower annealing temperature of the films leads to more residual,

polarizable hydroxo groups [31]. The leakage current density at 1 MV/cm is also large for 500 °C annealed film compared to 600 and 700 °C. This is due to the large amount of organic residual and low density of the films. Also, 500 °C annealed film is poor in quality as seen from XRD. XRD results also show that whatever the annealing temperature is, pure HfO₂ crystallizes into monoclinic phase.

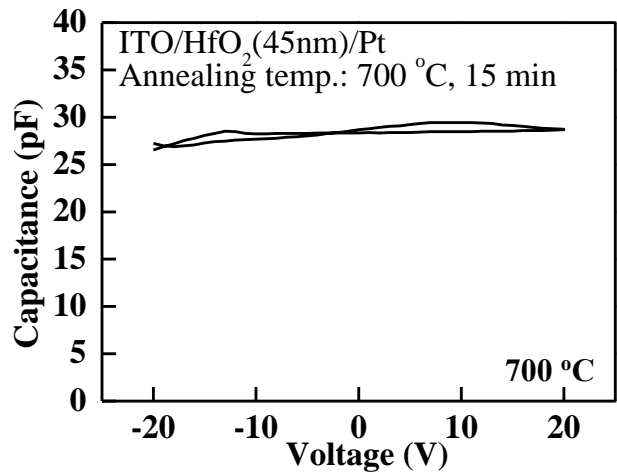
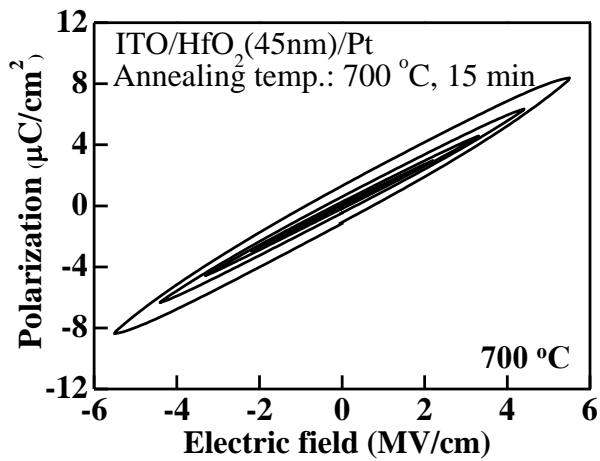
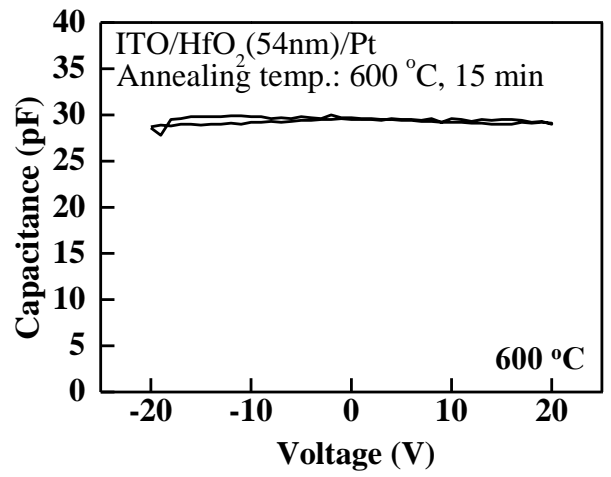
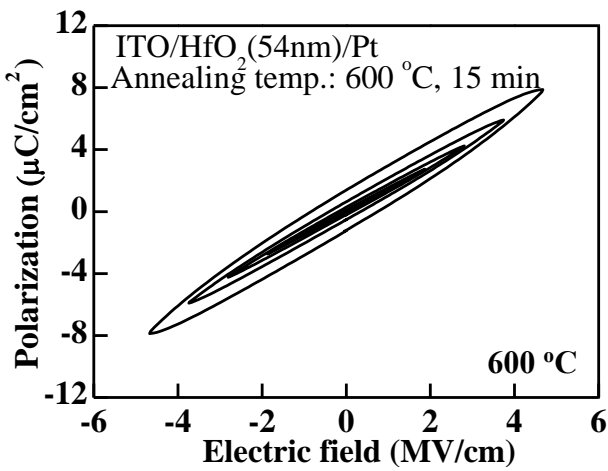
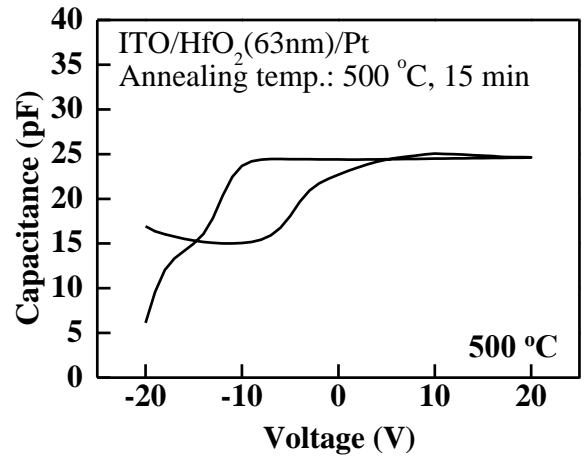
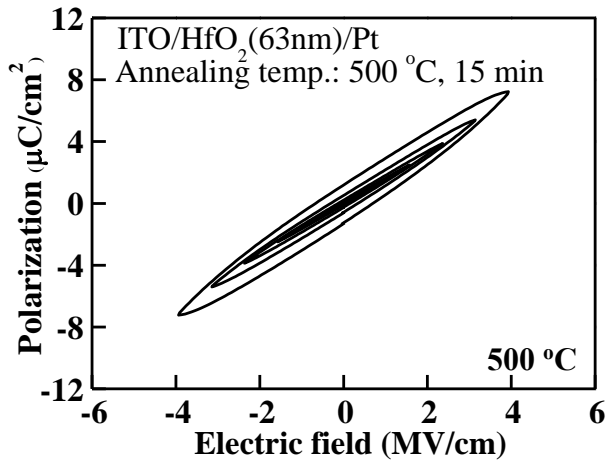


Fig. 4-5: P-E and C-V of HfO₂ films annealed at 500, 600, and 700 °C in O₂ for 15 min.

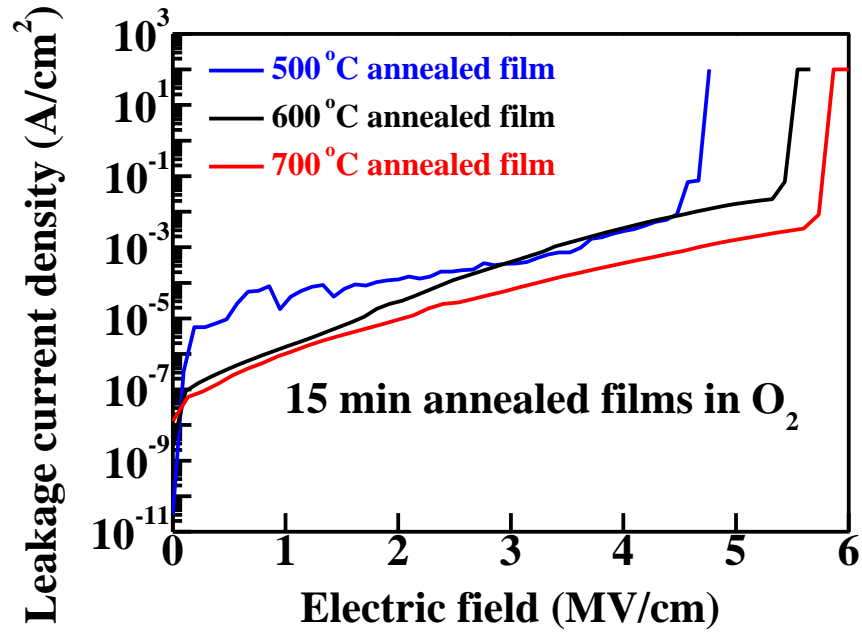


Fig. 4-6: J-E of HfO₂ films annealed at 500, 600, and 700 °C in O₂ for 15 min.

Table II: Relative dielectric constant (ϵ_r), breakdown field (E_{bd}), leakage current density, and thickness of HfO₂ films annealed at 500, 600, and 700 °C in O₂ for 15 min.

Annealing temperature	ϵ_r from P-E	ϵ_r from C-V	E_{bd} (MV/cm)	Leakage current density (A/cm ²) at 1MV/cm	Thickness (nm)
500 °C	21.17	19.45	3.84	2.86×10^{-5}	63
600 °C	19.26	17.98	5.36	1.61×10^{-6}	54
700 °C	17.58	15.91	5.78	1.01×10^{-6}	45

As 700 °C annealed HfO₂ films gives highest breakdown field strength and lowest leakage current density, so for TFT fabrication, we used 700 °C annealed HfO₂ films.

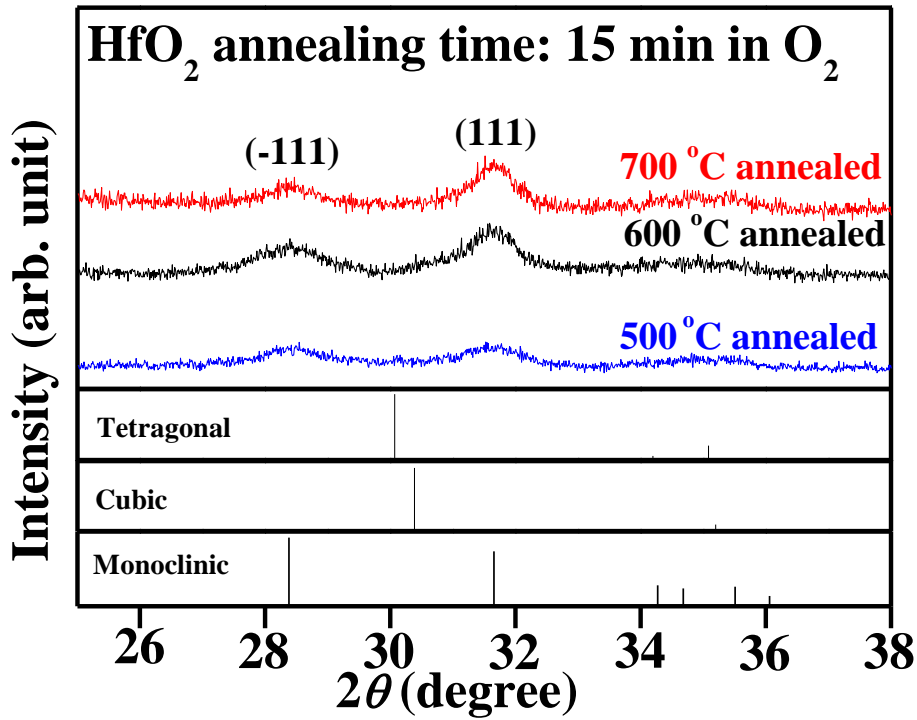


Fig. 4-7: XRD of HfO₂ films annealed at 500, 600, and 700 °C in O₂ for 15 min.

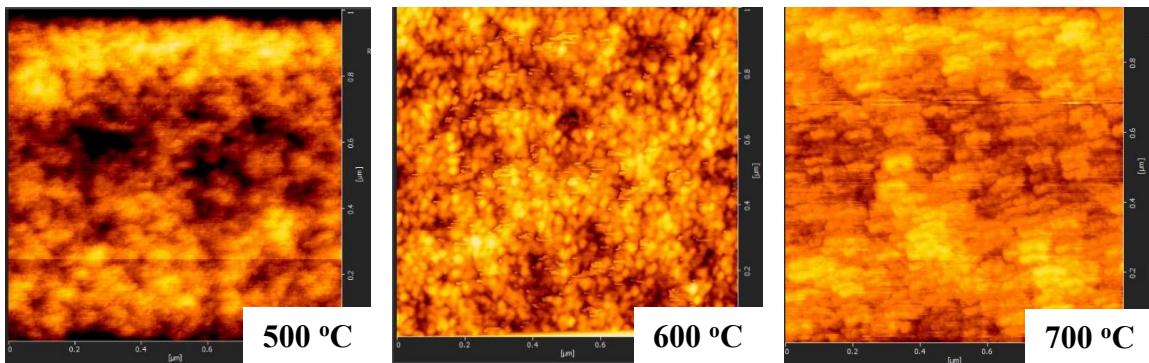


Fig. 4-8: AFM images of HfO₂ films annealed at 500, 600, and 700 °C in O₂ for 15 min.

Table III: RMS roughness of HfO₂ films annealed at 500, 600, and 700 °C in O₂ for 15 min.

Annealing temperature (°C)	RMS roughness (nm)
500 °C	0.73
600 °C	0.65
700 °C	0.82

As electrical properties improve with increasing annealing temperature, we could have annealed our films at 800 °C or above also. However, when we annealed the films at 800 °C, there starts peel-off of the platinum film from the substrate. This is because platinum is glued

on the SiO_2/Si substrate via Ti. At higher annealing temperature, Ti oxidizes to TiO_x and Pt starts to peel-off. An 800 °C sample showing peel-off is shown in Fig. 4-9.

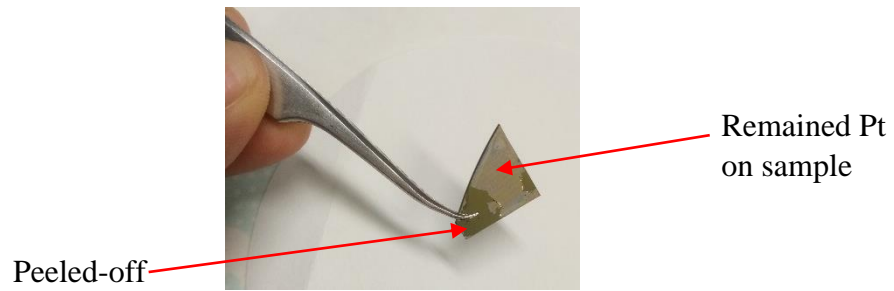


Fig. 4-9: Peel-off of Pt film from Pt/Ti/ SiO_2/Si substrate at 800 °C annealing.

Summary

In this present work, electrical properties (i.e. polarization-electric field (P-E), capacitance-voltage (C-V), and leakage current density-electric field (J-E)) of HfO₂ thin films by solution process were studied, by fabricating ITO/HfO₂/Pt, MIM capacitor, more precisely, electrical properties dependence on annealing temperature was studied. It is found that solution process derived pure HfO₂ film exhibit monoclinic phase, as confirmed by XRD studies, irrespective of annealing temperature. It has been confirmed by P-E studies that pure HfO₂ shows paraelectricity and as the electric field is increased, a hysteresis starts to appear in P-E, which is due to the leakage at higher field. As annealing temperature increases from 500 to 700 °C, film thickness decreases and leakage current density decreases. However, breakdown field increases. This is due to the reason that as annealing temperature increases, organic species from the films are removed and films become dense. The lowest leakage current at 1 MV/cm is 1.01×10^{-6} A/cm² for 700 °C annealed HfO₂ for 15 min, with a breakdown field of 5.8 MV/cm.

References

1. C. Driemer, R. M. Wallace, and I. J. R. Baumvol, *J. Appl. Phys.*, **102** (2004) 024112.
2. L. Pereira, P. Barquinha, E. Fortunato, and R. Martins, *Mater. Sci. Forum*, **514-516** (2006) 58.
3. J. Robertson, *J Non Cryst Solids*, **303** (2002) 94.
4. J. Robertson, *Rep. Prog. Phys.*, **69** (2006) 327.
5. High-k Gate Dielectrics, edited by M. Houssa (Institute of Physics, Bristol. 2004).
6. M. Czernohorsky, E. Bugiel, H. J. Osten, A. Fissel, and O. Kirfel, *Appl. Phys. Lett.*, **88** (2006) 152905.
7. L. Yan, C. M. Lopez, R. O. Shrestha, E. A. Irene, A. A. Suvorova, and M. Saunders, *Appl. Phys. Lett.*, **88** (2006) 142901.
8. S. Chen, Y. Zhu, R. Xu, Y. Q. Wu, X. J. Yang, Y. L. Fan, Z. M. Jiang, and J. Zou, *Appl. Phys. Lett.*, **88** (2006) 222902.
9. A. A. Dakhel *Phys. Status Solidi*, **201** (2004) 745.
10. T. Busani and R. A. B. Devine, *J. Appl. Phys.*, **98** (2005) 044102.
11. Y. Nishikava, T. Yamaguchi, M. Yoshiki, H. Satake, and N. Fukushima, *Appl. Phys. Lett.*, **81** (2002) 4386.
12. P. C. Juan, C. H. Liu, C. L. Lin, S. C. Ju, M. G. Chen, I. Y. K. Chang, and J. H. Lu, *Jpn. J. Appl. Phys.*, **48(2)** (2009) 05DA02.
13. S. Guha, E. Cartier, Ma. A. M. Gribelyuk, N. A. Bojarczuk, and M. C. Copel, *Appl. Phys. Lett.*, **77** (2000) 2710.
14. G. Aygun and R. Turan, *Thin Solid Films*, **517** (2008) 994.
15. M. K. Bera, C. Mahata, and C. K. Maiti, *Thin Solid Films*, **517** (2008) 27.
16. M. Copel, M. Giberyuk, and E. Gusev, *Appl. Phys. Lett.*, **76** (2000) 436.

17. W. J. Zhu, T. Tamagawa, M. Gibson, T. Furukawa, and T. P. Ma, *IEEE Electron. Device Lett.*, **23** (2002) 649.
18. L. Pereira, P. Barquinha, E. Fortunato, and R. Martins, *Mater. Sci. Forum*, **514** (2006) 58.
19. S. W. Nam, J. H. Yoo, S. Nam, H. J. Choi, D. Lee, D. H. Ko, J. H. Moon, J. H. Ku, S. Choi, *J. Non-Cryst. Solids*, **303** (2002) 139.
20. H. Gruger, C. Kunath, E. Kurth, S. Sorge, W. Pufe, T. Pechstein, *Thin Solid Films*, **447-448** (2004) 509.
21. J. Aarik, H. Mandar, M. Kirm, L. Pung, *Thin Solid Films*, **466** (2004) 41.
22. G. D. Wilk, R. M. Wallace, J. M. Anthony, *J. Appl. Phys.*, **89** (2001) 5243.
23. J. Weng, W. Chen, W. Xia, J. Zhang, Y. Jiang, G. Zhu, *J Solgel Sci. Technol.*, **81** (2017) 662.
24. Taube, S. Gieraltowska, T. Gutt, T. Malachowski, I. Pasternak, T. Woj-ciechowski, W. Rzekiewicz, M. Sawaicki, and A. Piotrowska, *Acta. Phys. Pol. B.*, **119** (2011) 696.
25. A. Tarasov, M. Wip, R. L. Stoop, K. Bedner, W. Fu, V. A. Guzenko, O. Knopfmacher, M. Calame, and C. Schonenberger, *ACS Nano.*, **5** (2013) 12104.
26. <https://scholarworks.rit.edu/cgi/viewcontent.cgi?article=10042&context=theses>.
27. D. Shin, R. Arroyave, and Z. Liu, *CALPHAD*, **1** (2018) 1.
28. M. C. Cheynet, S. Pokrant, F. D. Tichelaar, and J.-L. Rouviere, *J. Appl. Phys.*, **101** (2007) 5.
29. X. Y. Zhao and D. Vanderbilt, *MRS Preced.*, **747** (2003) 93–98.
30. J. Muller, P. Polakowski, S. Mueller, and T. Mikolajick, *ECS J. Solid State Sci. Technol.*, **4 (5)** N30 (2015)
31. Y. B. Yoo, J. H. Park, K. H. Lee, H. W. Lee, K. M. Song, S. J. Lee, and H. K. Baik, *J. Mater. Chem. C*, **1** (2013) 1651.

5. In₂O₃ Channel Thin Film Transistor (TFT) by Solution Process and n-RP

5.1 Introduction

Indium oxide (In₂O₃)-based oxide films are used in wide range of applications, like photovoltaics, smart windows, displays, sensors, etc. In₂O₃ and indium tin oxide (ITO) are also used as channel in TFTs.

To keep Moore's law active, it is necessary to scale down the channel length into submicron or even nanometer-scale range to get high speed at low operating voltage [1]. The conventional ways to fabricate the short-channel devices are electron beam lithography [2], nano-imprint lithography [3, 4], etc. These techniques are successful to get submicron channel length TFTs, but they need vacuum process, which is time consuming and costly. So researchers have moved to printed electronics. There are many types of printed electronics like inkjet printing, screen printing, gravure printing, roll-to-roll printing, flextronics, etc. Amongst these, inkjet printing has gained popularity due to the advantages of low temperature deposition, so, we can use large number of cheap substrates like paper, glass, polymer, wood, textile, etc. Another advantage of inkjet printing is that it is easy to implement, as it does not require large number of steps as in photolithography. Inkjet printing is an alternate to get such scale of channel length but it suffers from the problem of resolution.

As in the previous chapters, we have introduced the concept of nano-rheology printing (n-RP); in this chapter, we describe the details of TFT formation by n-RP process, which is simple and does not take much time as other vacuum techniques. As described earlier, using n-RP process, we get source/drain and channel, simultaneously. Also, source/drain and channel, all are made up of same material in the TFT fabricated by n-RP process. The thick regions act as

source/drain while the thin regions act as channel. It is found (in chapter 3) that, after n-RP carrier concentration increases. TFT works because source/drain are concave regions of the mold and channel is convex region of the mold. In other words, channel is formed by imprinting and has high carrier concentration than source/drain.

Since, In_2O_3 and ITO have high carrier concentration, so, when they are used as channel, then it is necessary to deplete the carrier concentration of the channel to get low off current. Gate insulator does this depletion and the possible candidates for the gate insulator are:

- ferroelectric material like $\text{Pb}(\text{Zr,Ti})\text{O}_3$ (PZT), $(\text{Ba,Lu})_4\text{Ti}_3\text{O}_{12}$ (BLT), $\text{SrBi}_2\text{Ta}_2\text{O}_9$ (SBT), etc., or
- high- k gate dielectric materials like Al_2O_3 , HfO_2 , La_2O_3 , MgO , etc., which can induce large charge density to control the conductive channel layer.

TFTs with ferroelectric gate insulator are known as ferroelectric gate TFT (FeTFT) [5, 6]. Ferroelectric materials induce large charge density, which helps to get large on-current and low-off current, due to the spontaneous/remnant polarization of ferroelectric materials. This gives large $I_{\text{on}}/I_{\text{off}}$ ratio. For depletion, the channel should be thin enough for complete depletion. Another advantage of using FeTFT is that the TFTs with non-volatile memory operation can be realized due to polarization hysteresis and transfer curve of the of the device exhibits hysteresis loop.

For displays applications, TFTs, which have transfer curve without hysteresis loops, are required. For these TFTs, in-place of ferroelectric gate insulator, high- k gate insulator are used, like $(\text{Ba}_{0.3}\text{Sr}_{0.7})\text{TiO}_3$ (BST), $\text{Bi}_{1.5}\text{Zn}_{1.0}\text{Nb}_{1.5}\text{O}_7$ (BZN), hafnium dioxide (HfO_2), etc. TFTs having paraelectric gate material are widely studied due to their strong expectancy for flat-panel displays and system-on-panel applications [7]. For the complete depletion of the channel

layer, using high- k material, the charge density of the gate insulator is greater than the charge density of the channel. Mathematically,

$$q \cdot n \cdot d < \varepsilon_0 \cdot \varepsilon_r \cdot E_{BD} \quad (1)$$

where, q , n , and d are the elemental charge, carrier concentration of the oxide channel, and thickness of oxide channel layer, respectively. ε_0 , ε_r , and E_{BD} are dielectric constant of vacuum, relative dielectric constant of gate insulator, and breakdown field of gate insulator, respectively.

In the present work, we have fabricated bottom-gate TFT with n-RP process, with In_2O_3 as source/drain and channel, while HfO_2 as gate dielectric. In_2O_3 and HfO_2 , both are fabricated by solution process. Platinum is used as a gate electrode. It is easy to get TFT operation with ferroelectric gate insulator and many reports are available on this but very few reports are available with In_2O_3 as channel and HfO_2 as gate insulator.

5.2 Fabrication process

The complete process flow for the fabrication of thin film transistor using the In_2O_3 channel and HfO_2 gate dielectric is shown in Fig. 5-1. First, pure HfO_2 film (as gate dielectric film) was spin-coated on Pt/Ti/SiO₂/Si substrate, which was first cleaned with acetone, isopropanol alcohol (IPA) and deionized water (DI water). The HfO_2 film (concentration of 0.2 mol/kg) was coated 3 times to get the desired thickness (this is explained in previous chapter 4) and annealed at 700 °C for 15 min in O₂ atmosphere for crystallization. Then it was etched using photolithography to measure its thickness and to make contact from the bottom gate electrode, i.e. platinum. In_2O_3 source solution was spin-coated on HfO_2 film to make source/drain and channel of In_2O_3 . The spin-coated In_2O_3 on HfO_2 /Pt/SiO₂/Si film then dried in air at 100 °C for 3 min to make it a precursor-gel film. Then imprinting was done on this gel In_2O_3 film via SNP-02 checker mold. The imprinting was done with an imprinting pressure of 6 MPa, imprinting time of 5 min, cooling rate of 5.8 °C/min, and imprinting temperature of 175 °C (as

discussed in chapter 3). Platinum (of Pt/Ti/SiO₂/Si substrate) was used as a bottom gate electrode.

After imprinting, the sample was annealed in O₂ for 1 h in O₂ at 600 °C (this condition was adopted from the optimization as discussed in chapter 2). Finally, the device isolation was done by photolithography via wet-etching. To carry out lithography, first thinner OAP was spin-coated on the sample at 5000rpm/20sec and the positive photoresist (PR); OFPR, was spin-coated on it at 5000rpm/20sec. It was then dried on hot-plate at 110 °C for 1.30 min (pre-baking). Then photolithography was carried out by exposing ultraviolet (UV) light through a Cr plated glass mask at 350 W for 12 s. The exposed PR was developed in NMD-3 solution and then rinsed in DI water. The developed sample was post-baked at 110 °C for 5 min on hot-plate. Then it was etched by HCl acid and the resist was removed by dipping the sample in acetone, then in iso-propyl alcohol (IPA), and finally in DI water. The complete process flow is shown in Fig. 5-1. The complete structure of the fabricated TFT is shown in Fig. 5-2. The thick regions on the precursor-gel, which correspond to the concave regions of the mold, act as source/drain, while the residual film acts as a channel layer. These are shown clearly in Fig. 5-2.

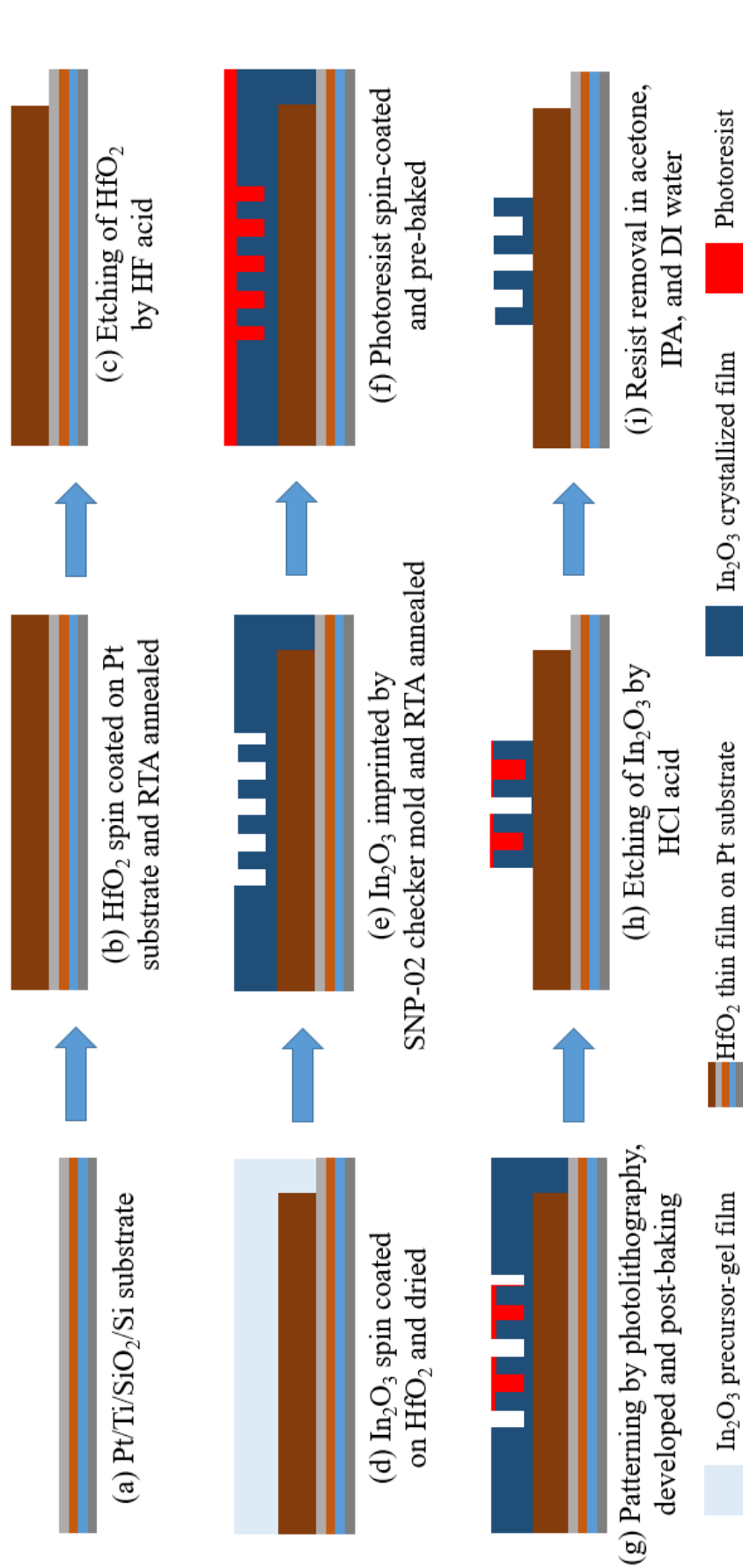


Fig. 5-1: Process flow for TFT fabrication.

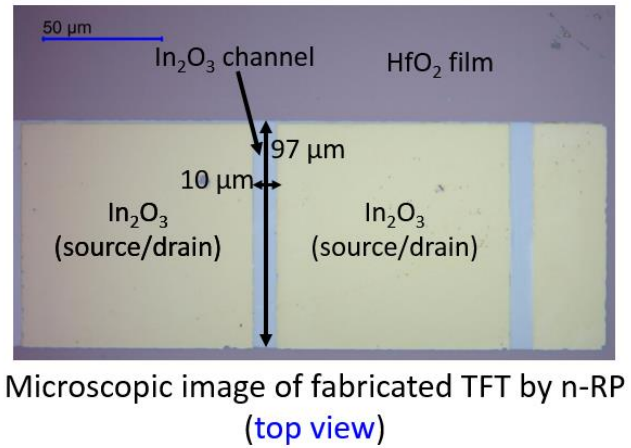
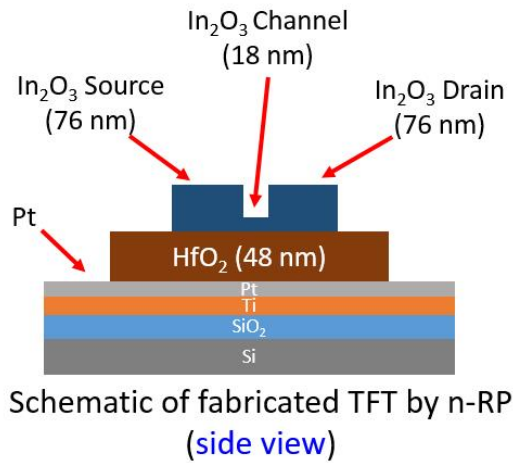


Fig. 5-2: Top and side view of fabricated TFT by n-RP process.

5.3 Results and discussion

The thin film transistor using solution processed In_2O_3 as source/drain and channel, while HfO_2 as gate insulator was fabricated with channel length of $10\ \mu\text{m}$ and width $97\ \mu\text{m}$, respectively. This is because we used SNP-02 checker mold (described in chapter 3), so source/drain and channel were imprinted by SNP-02 mold, hence the fabricated length and width of the channel is 10 and $97\ \mu\text{m}$ (shown in Fig. 5-2). Width was also expected to be $100\ \mu\text{m}$, but it is around $97\ \mu\text{m}$, which may be due to side etching during wet etching or may be due to misalignment during channel isolation. The TFT was fabricated by n-RP process, with an imprinting pressure of $6\ \text{MPa}$, imprinting time of $5\ \text{min}$, cooling rate of $5.8\ \text{°C min}^{-1}$, and imprinting temperature of $175\ \text{°C}$. The thickness of the In_2O_3 channel is $18\ \text{nm}$, while the thickness of the In_2O_3 source/drain electrode is $76\ \text{nm}$. The thickness of HfO_2 gate insulator is $48\ \text{nm}$. Figure 5-3 shows the transfer characteristics while Fig. 5-4 shows the output characteristics of the fabricated transistor. Transfer characteristics with gate sweep voltage of $\pm 20\ \text{V}$, clearly shows n-channel operation, with large counter-clockwise hysteresis. This counter-clockwise hysteresis is not due to ferroelectric property, but this hysteresis may be due to the channel-dielectric interface oxide charges. In addition, our channel and gate dielectric were fabricated by solution process and solution derived films have residual organics. Another reason for this

hysteresis is due to the oxides at the interface. These may also be the reason for large hysteresis in transfer curve [8-12]. I_{DS} - V_{DS} exhibits a clear pinch-off and current saturation, confirming that TFT follows standard field effect transistor (FET) theory as transistor behaviour is observed. However, the on/off ratio is 9.97×10^4 ($\sim 10^5$) with ON current of $1.44 \times 10^6 \mu\text{A}/\mu\text{m}$ at gate voltage of 20 V and OFF current of $14.43 \mu\text{A}/\mu\text{m}$ at gate voltage of -5 V. The carrier concentration of channel (i.e. thin region obtained on the precursor gel film after imprinting) is $4.1 \times 10^{19} \text{ cm}^{-3}$ while the sub-threshold swing (SS) is 2.3 V/dec when V_{GS} is swept from -20 to +20 V and it is 0.54 V/dec, when V_{GS} is swept from +20 to -20 V.

The mobility in the saturation region can be calculated from saturation drain current (I_{DS}) given by the formula:

$$I_{DS} = \frac{C_i \mu W}{2L} (V_{GS} - V_T)^2 \quad (2)$$

In Eq. (2) W and L are channel width and length, C_i is gate oxide, V_{GS} is gate-source voltage, I_{DS} is drain-source current, V_T is threshold voltage, respectively.

The mobility at saturation region is $0.13 \text{ cm}^2/\text{Vs}$ with $V_T = 1.9 \text{ V}$. Threshold voltage estimation was calculated from $\sqrt{I_{DS}}$ v/s V_{GS} plot shown in Fig. 5-5, where the dotted line represents the extrapolated line drawn to estimate V_T .

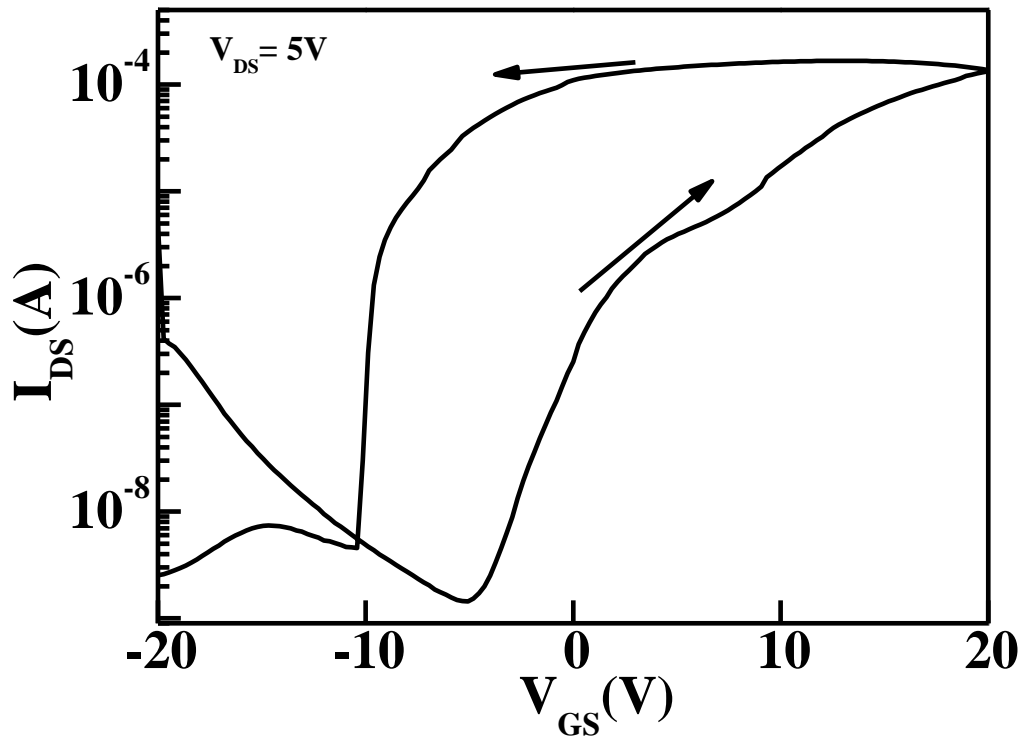


Fig. 5-3: Transfer characteristics of fabricated TFT by n-RP.

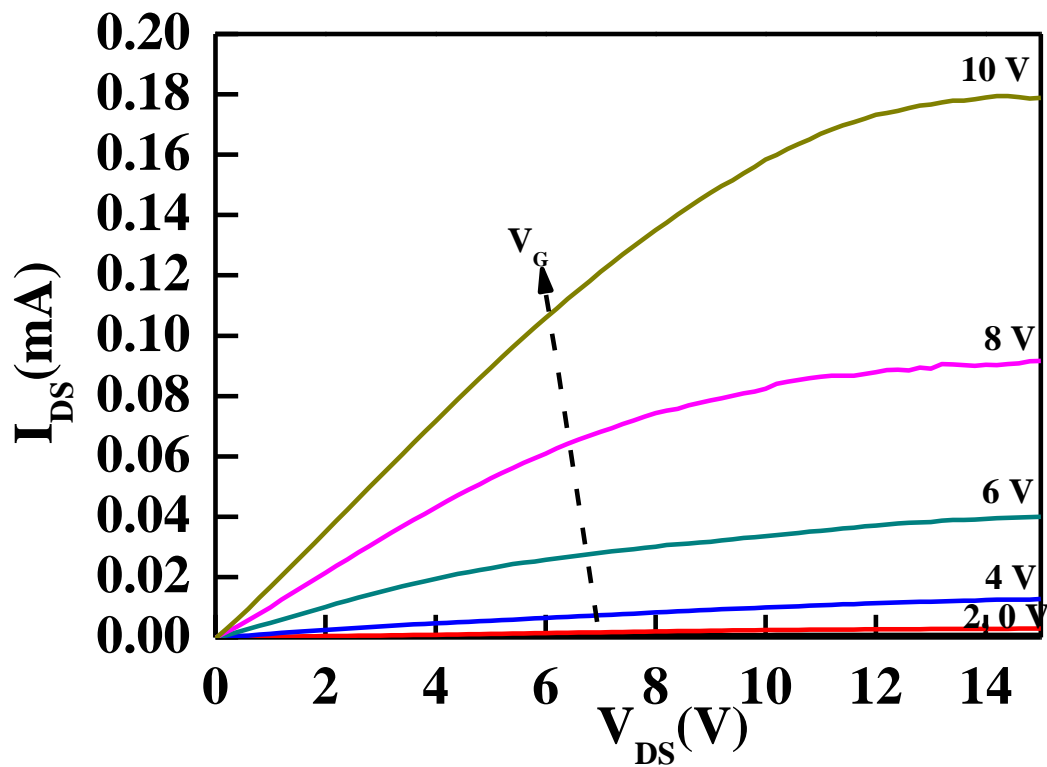


Fig. 5-4: Output characteristics of fabricated TFT by n-RP.

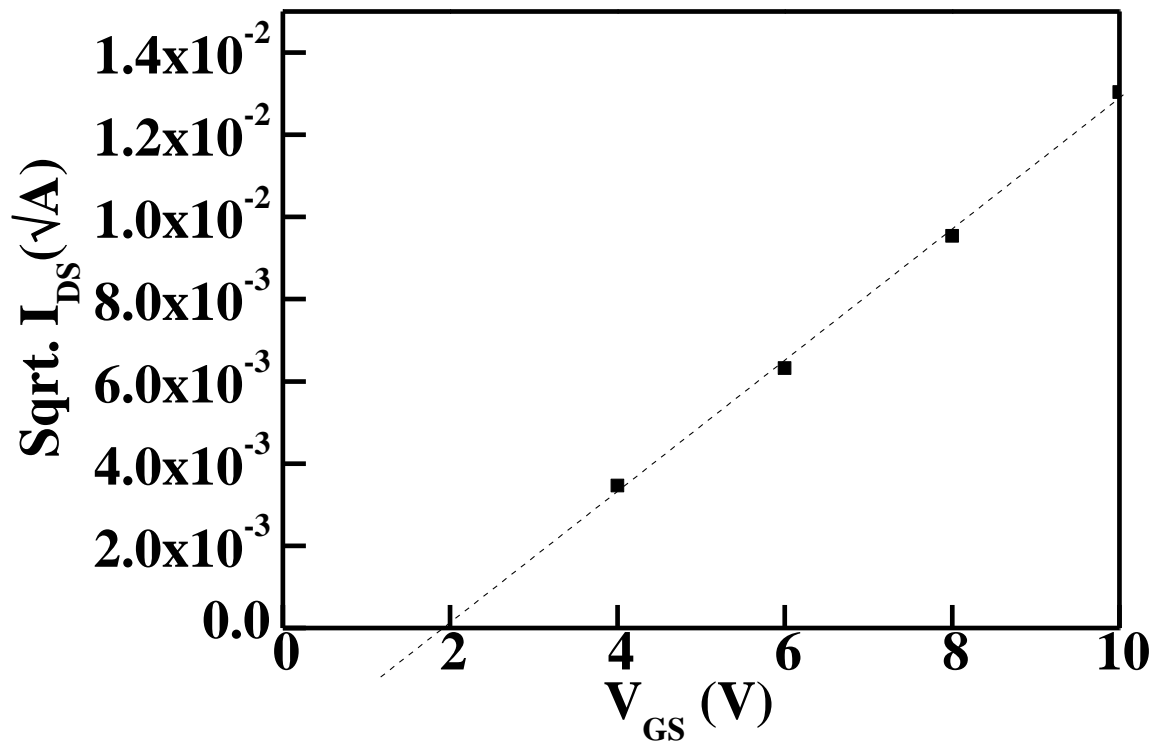


Fig. 5-5: Threshold voltage estimation of fabricated TFT by n-RP.

Summary

In this chapter, bottom-gate thin film transistor (TFT) using solution-processed In_2O_3 as a channel and source/drain; and solution-processed HfO_2 as a high- k gate dielectric film, was fabricated and characterized. Pt from the Pt/Ti/SiO₂/Si substrate was used as bottom gate electrode. Bottom-gate was selected, as the crystallization temperature of HfO_2 was higher than that of In_2O_3 . 0.3 mol/kg was the concentration of used In_2O_3 while 0.2 mol/kg was the concentration of used HfO_2 . Since, In_2O_3 is an n-type semiconductor, so the TFT output characteristics shows n-channel operation with drain current saturation. As the solution-processed films have large amount of hydroxyls into it and also due to the oxide charges at interface, the transfer characteristics showed large hysteresis in counter-clockwise direction. The calculated TFT parameters are, on/off ratio is in the order of $\sim 10^5$, SS: 2.3 V/dec, mobility: 0.13 cm²/Vs, and threshold voltage: 1.9 V.

References

1. T. T. Phan, J. Li, and T. Shimode, *Nano Futures*, **2** (2018) 035006.
2. I. Song, S. Kim, H. Yin, C. J. Kim, J. Park, S. Kim, H. S. Choi, E. Lee, and Y. Park, *IEEE Electron Device Lett.*, **29** (2008) 549.
3. C. Kim, M. Shtein, and S. R. Forrestb, *Appl. Phys. Lett.*, **80** (2002) 4051.
4. M. D. Austina, S. Y. Chou, *Appl. Phys. Lett.*, **81** (2002) 4431.
5. E. Tokumitsu, M. Senoo, and T. Miyasako, *Microelectron. Eng.*, **80** (2008) 305.
6. K. Haga, Y. Nakada, D. Ricinschi, and E. Tokumitsu, *Jpn. J. Appl. Phys.*, **53** (2014) 09PA07.
7. T. Miyasako, M. Senoo, and E. Tokumitsu, *Appl. Phys. Lett.*, **86** (2005) 162902.
8. Y. B. Yoo, J. H. Park, K. H. Lee, H. W. Lee, K. M. Song, S. J. Lee, and H. K. Baik, *J. Mater. Chem. C*, **1** (2013) 1651.
9. K. Suzuki and K. Kato, *J. Am. Ceram. Soc.*, **92** (2009) S162.
10. J. Weng, W. Chen, W. Xia, J. Zhang, Y. Jiang, and G. Zhu, *J. Sol-Gel Sci. Technol.*, **81** (2017) 662.
11. Y. Aoki, T. Kunitake, and A. Nakao, *Chem. Mater.*, **17** (2005) 450.
12. H. Shimizu, S. Konagai, M. Ikeda, and T. Nishide, *J. Jpn. Appl. Phys.*, **48** (2009) 101101.

6. Conclusion

6.1 Summary and conclusions of this research

Unlike most of the research for In_2O_3 -based films, which use vacuum techniques to deposit thin films, in this complete work solution process derived indium oxide (In_2O_3) and indium tin oxide (ITO) films were used, which were deposited directly on high- k hafnium oxide (HfO_2) for thin film transistors (TFTs) application. To fabricate TFT, researchers use lithography, sputtering, or other vacuum techniques. Nano-rheological printing (n-RP) is a new technique which helps to fabricate source/drain and channel, simultaneously. This saves time and also does not need costly vacuum techniques.

In chapter 1, as an introduction of this research, it is shown how n-RP is a novel technique to pattern metal-oxide gel films, which can then be used to fabricate TFTs or electrodes. Although there are many conventional techniques to make TFTs for displays and memories, but n-RP is a direct thermal imprinting technique, which does not need resist. This chapter also focuses on the advantages of solution process over costly techniques like sputtering, CVD, etc. The objective of this research is to develop chemical solution processed In_2O_3 , ITO and HfO_2 thin films and to use these solution-derived thin films to fabricate transistor by n-RP.

In chapter 2, solution processed In_2O_3 and ITO, electrical properties were studied with respect to annealing time and annealing temperature, using $\text{In}(\text{acac})_3$ precursor. For In_2O_3 case, using $\text{In}(\text{acac})_3$ precursor, mobility as high as $42.8 \text{ cm}^2/\text{Vs}$ was obtained with a carrier concentration of $9.47 \times 10^{18} \text{ cm}^{-3}$, when In_2O_3 film was annealed for 1 h in O_2 at $600 \text{ }^\circ\text{C}$. ITO was prepared using two different precursors for tin (Sn). One source solution was prepared using $\text{In}(\text{acac})_3$ and SnCl_2 in PrA (named as ITO via SnCl_2), while the other was prepared using $\text{In}(\text{acac})_3$ and $\text{Sn}(\text{acac})_2$ in PrA (named as ITO via $\text{Sn}(\text{acac})_2$). The concentration of Sn was varied from 1 to

10 wt.%. It was found that as the Sn concentration increases, mobility decreases due to the reason that Sn acts as impurity in In₂O₃ cubic bixbyite structure. Therefore, more the Sn content, more impurity scattering, hence less mobility. Resistivity as low as $2.6 \times 10^{-3} \Omega\text{cm}$ for our ITO films was obtained for 1 wt.% ITO via Sn(acac)₂ with a mobility of 24 cm²/Vs and carrier concentration of $1.0 \times 10^{20} \text{cm}^{-3}$.

In chapter 3, patterning and electrical properties of direct imprinted In₂O₃ and ITO films were studied. N-RP is a resist-free, direct patterning technique to achieve patterns in the metal-oxide precursor-gel in the nanoscale range, allowing precise shape control. The addition of tin (Sn) to In₂O₃ (i.e. ITO) degrades the n-RP properties because the tan δ value of ITO is smaller than that of In₂O₃. Consequently, the electrical properties of imprinted ITO films are not altered as much as compared to non-imprinted ITO films, but are greatly affected in the case of imprinted In₂O₃ compared to the non-imprinted In₂O₃ films. The Hall mobility of imprinted In₂O₃ decreases due to the trapped carbon, as confirmed by SIMS measurements, which showed that even after annealing at 600 °C for 1 hour, there was more carbon in the imprinted In₂O₃ than non-imprinted In₂O₃. An increase in the carrier concentration in imprinted films is due to the increase in oxygen vacancies in In₂O₃ after imprinting, as confirmed by XPS studies.

In chapter 4, electrical properties (i.e. P-E, C-V, and J-E) of HfO₂ by solution process were studied, by fabricating ITO/HfO₂/Pt MIM capacitor. Solution process derived HfO₂ film exhibit monoclinic phase, as confirmed by XRD studies, irrespective of annealing temperature. It has been confirmed by P-E studies that pure HfO₂ shows paraelectric behaviour, as monoclinic HfO₂ is paraelectric in nature. As annealing temperature increases, thickness and leakage current density decrease. However, breakdown field increases. This is due to the reason that as annealing temperature increases, organic species from the films are removed and films become dense. The lowest leakage current density at 1 MV/cm is $1.01 \times 10^{-6} \text{A/cm}^2$ for 700 °C annealed HfO₂ for 15 min, with a breakdown field of 5.78 MV/cm.

In chapter 5, using In_2O_3 as a channel, TFT was fabricated using n-RP technique with HfO_2 as a high- k gate dielectric. Chemical solution processed In_2O_3 film was fabricated directly on the solution process derived HfO_2 gate insulator. It is shown that the TFT showed a typical n-type semiconductor behaviour with an on/off ratio of order of $\sim 10^5$. The calculated mobility in the saturation region $0.13 \text{ cm}^2/\text{Vs}$ with $V_{\text{th}} = 1.9 \text{ V}$.

6.2 Future prospects of this study

In this present study, the In_2O_3 and ITO were deposited on high- k oxide film, hafnium oxide (HfO_2), directly by the chemical solution process. This work shows possibility that the solution processed In_2O_3 based oxide films could be applied to electronics applications. However, there are several points which have to be investigated.

First, it is an interesting work to use doped HfO_2 instead of pure HfO_2 , like Y-doped HfO_2 , Zr-doped HfO_2 . It is well known that doped HfO_2 shows ferroelectricity which means remnant polarization, so the transfer curve of TFT fabricated via doped HfO_2 , should show memory window due to the hysteresis. As pure HfO_2 is paraelectric in nature, so the TFT can only be used for display applications because of absence of memory window. Having memory window in the transfer characteristics of TFT, allows to use TFT for memory applications.

Second, it is also interesting to deposit In_2O_3 based films on sputtered or ALD deposited gate insulator, keeping top In_2O_3 based oxide film by solution process. This is because for n-RP process, solution processed films are required as imprinting is done in the gel state. So we can keep the In_2O_3 layer by solution process and change the gate dielectric from solution process to any other vacuum technique. Then we can also compare the output and transfer characteristics of TFTs with solution processed gate insulator and same gate insulator material by other technique.

Third one is changing the oxide semiconducting material from In_2O_3 and ITO to any other oxide material like zinc oxide (ZnO), aluminium doped zinc oxide (AZO), gallium indium zinc oxide (GIZO), tin oxide (SnO_2), gallium oxide (Ga_2O_3), etc. But, before performing the imprinting of these oxides, it is very necessary to check the rheological properties of these oxides. If they show rheological properties, then impinging can be done by choosing a large variety of gate insulator and also by changing the deposition techniques of the gate insulator.

Fourth is to keep the channel layer and insulator layer same as, they are used in this work, but by varying the SAM layer formation. In other words, we can study the role of SAM layer, the complete mechanism of SAM layer and hydrophobicity, etc. This itself is a very new topic of research for n-RP process, as SAM layer is helpful in the damage-free removal of the mold from the imprinted film. If the mold and the film get bonded then the patterns break during the detachment of the mold.

Fifth, it would also be interesting to change the precursors of In_2O_3 , ITO, and HfO_2 from $\text{In}(\text{acac})_3$, SnCl_2 , $\text{Sn}(\text{acac})_2$, and $\text{Hf}(\text{acac})_4$ to any other precursor.

However, there are just few future aspects. There can be numerous things that can be done.

Announcement list

Journal Papers

1. “Electrical and Patterning Properties of Indium Oxide (In_2O_3) and Indium Tin Oxide (ITO) by Direct Nanoimprinting Technique”, **Puneet Jain**, Chang Su, Ken-ichi Haga and Eisuke Tokumitsu, *Jpn. J. Appl. Phys.*, **58** (2019) SDDJ05 (chapter 3 is referred from this paper).
2. “Electrical Properties of In_2O_3 and ITO Thin Films Formed by Solution Process using $\text{In}(\text{acac})_3$ Precursor”, **Puneet Jain**, Ken-ichi Haga, and Eisuke Tokumitsu (submitted; chapter 2 is referred from this paper).

International conferences

1. “Electrical Properties of In_2O_3 and In-Sn-O Films Prepared by Direct Nanoimprinting”, **Puneet Jain**, Ken-ichi Haga, and Eisuke Tokumitsu, The 31st International Microprocessor and Nanotechnology Conference (MNC’ 18), November 13-16, Sapporo Park Hotel, Sapporo, Japan (poster).
2. “Hall Mobility and Carrier Concentration of $\text{In}(\text{acac})_3$ Precursor Derived Solution Processed In_2O_3 and ITO Thin Films”, **Puneet Jain**, Ken-ichi Haga, and Eisuke Tokumitsu, The 7th International Symposium on Organic and Inorganic Electronic Materials and Related Nanotechnologies (EM-NANO 19), June 19-22, Shinshu University, Nagano, Japan (poster).

Domestic conferences

1. “Electrical Properties of In_2O_3 and ITO Thin Films Prepared by Solution Process using $\text{In}(\text{acac})_3$ Precursor”, **Puneet Jain**, Ken-ichi Haga, and Eisuke Tokumitsu, Japan Society of Applied Physics (JSAP 66th Spring Meeting’ 19), March 9-12, Tokyo, Japan (poster).
2. “Direct Imprinting and Electrical Properties of ITO Precursor gel”, **Puneet Jain**, Ken-ichi Haga, and Eisuke Tokumitsu, Japan Society of Applied Physics (JSAP 65th Spring Meeting’ 18), March 17-20, Tokyo, Japan (oral).
3. “Study of Electrical and Imprinting Properties of ITO Precursor Gel using Direct Imprinting”, **Puneet Jain**, Chang Su, Ken-ichi Haga, and Eisuke Tokumitsu, Japan Advanced Institute of Science and Technology (JAIST) Japan-India Symposium, March 5-6, JAIST, Nomi, Japan (poster).